UNIVERSIDAD NACIONAL AUTÓNOMA DE MÉXICO

PROGRAMA DE POSGRADO EN ASTROFÍSICA

Instituto de Astronomía

ESTRELLAS DE NEUTRONES ULTRAMAGNETIZADAS.

TESIS

PARA OPTAR POR EL GRADO DE:
DOCTORA EN CIENCIAS (ASTRONOMÍA)

PRESENTA:
JILLIAN ANNE HENDERSON GERELUS

TUTOR
DR. DANY PIERRE PAGE ROLLINET, INSTITUTO DE ASTRONOMÍA - UNAM

MÉXICO, D. F. ABRIL 2014

Por mi familia.

Abstract

Increasingly improved astronomical observations of compact objects such as pulsars and other neutron star phenomena has created the need for a comprehensive physical description of matter around nuclear density. In neutron star cores the density can go well beyond, the properties of which are still quite mysterious though their importance in governing observable spectra is increasingly evident. One such aspect in determining the observable surface temperature, spectrum and timing properties is heat transport within the star. In the outer less dense layers the properties of matter is much better understood partly due to experimental particle physics results performed on Earth and more thoroughly tested mathematical treatments of particle interactions in the sub-nuclear regime. This insulating outer layer takes the heat generated in the core and determines the resulting surface temperature profile which in turn is observed and interpreted, thus providing a window into the depths of compact matter, the likes of which is irreproducible on Earth. The usefulness of the numerical method of Finite Differencing applied to the problem of diffusion in multiple dimensions in spherically symmetric coordinates is investigated and numerical models of the thermal evolution of neutron stars based on these methods are presented. Furthermore, the effect on anisotropic surface temperature distribution from the presence of a strong magnetic field and their resultant phenomena are examined. This project attempts to elucidate various case studies of known compact objects with the intention of conecting theory with observation.

Agradecimientos

Quiero agradecer mi familia, especialmente Papi, el Bebo y mis papas sin cuya paciencia y tiempo yo no lo habría podido escribir este tésis. Un “gracias” grande a mi ascesor Dany para introducirme al mundo maravilloso de las estrellas de neutrones y a mis amigos y colegas para discusiones enormamente útiles, especialmente Irina Sagert, Tobias Fischer, Andrew Cumming y Etienne Rollin.

Contents

List of Figures

List of Tables

Chapter 1

Resumen en Español

1.1. Introducción

Las observaciones astronómicas de objetos compactos como los pulsares y otros fenómenos relacionados con las estrellas de neutrones mejoran constantemente, lo cual ha creado la necesidad de obtener una descripción cada vez mas comprehensiva de la física de la matéria a densidades cercanas a la densidad nuclear. En los núcleos de las estrellas de neutrones la densidad puede ir mucho más allá de la densidad nuclear, donde las propriedades de la materia siguen siendo poco entendidas. En las capas exteriores menos densas las propriedades de la matería son mejor entendidas en parte debido a los resultados de la física nuclear experimental realizado en la Tierra y también debido a los modelos matemáticos de las interacciones de partículas en el régimen sub-nuclear. La capa aislante exterior transporta el calor desde el núcleo hacia la superficie y determina el perfil de la temperatura superficial observada lo que nos proporciona una ventana a las profundidades de la materia compactada en condiciones imposibles de producir en la Tierra.

Evolución Térmica de Estrellas de Neutrones Por el momento es generalmente aceptado que las estrellas de neutrones son formadas en el núcleo de una supernova con temperaturas internas muy altas $T \gtrsim 10^{11} K$. En los primeros minutos de su vida, la temperatura del núcleo baja a 10^{10} K por la emisión de neutrinos, quienes se encargan principalmente de la perdida de energía hasta $T \sim 10^{8} K$ que es cuando los fotones asumen esta función. Resolviendo la ecuación de balance de energía dentro de una estrella de neutrones, nos da calculos teóricos del enfriamiento que establecen las escalas de tiempo. Las observaciones

de temperaturas superficiales en combinación con edades inferidas (e.j. la asociación con remanentes de supernovas, SNr) son usadas para soportar ó rechazar estas teorias. Mientras se puede deducir de estas teorías información de las propriedades que dependen de T cómo los coeficientes de transporte (e.j. la conductividad térimica), la transición a estados superfluidos, solidificación de la matéria de la corteza y más.

Es de particular importancia en este momento encontrar evidencia de la transición a estados superfluidos. Recientemente Heinke & Ho [47] demostraron por primera vez evidencia directa del enfriamiento rápido de una estrella de neutrones. Analizaron datos de Cassiopeia A (*Cas A*), una estrella de neutrones descubierta en 1999 en la observación de primera luz de *Chandra* [102] asociada con la supernova historica SN 1680 [6]. Observaron que su temperatura superficial bajó de $2.12 \times 10^6 K$ en el año 2000 a $2.04 \times 10^6 K$ en 2009 - una disminución de 4% en solo nueve años. Poco después, Page et al [75] propusieron que el enfriamiento en Cas A fue debido al comienzo de la superfluidez en el núcleo de la estrella y proponen que va a continuar por las próximas décadas (la misma descripción fue propuesta, independentemente, por [97]). Para mostrar que se puede explicar la evolución térmica de Cas A por los processos de enfriamiento dentro de una estrella de neutrones, usaron la solución numérica de cálculos de balance de energía y transporte de calor incluyendo la relatividad general y emparejamiento. El modelo resuelve las ecuaciones previamente mencionadas en una dimensión (radial) de una estrella esféricamente simétrica con la microfísica descrita en [74] y [73].

Los modelos de enfriamiento en una dimensión son muy poderosos y pueden mostrar los efectos de propiedades dependientes en la temperatura y la densidad, suponiendo una estrella esféricamente simétrica con capas de densidad uniformes. Se puede comparar efectivamente teorías del efecto del estado de la matería densa (conocido como la *ecuasión de estado, EOS*), las propiedades superfluidas de la matería densa, la composición de la corteza de la estrella de neutrones y su masa con las observaciones de las temperaturas efectivas para eliminar algunas de las posibilidades [73]. Sin embargo, hay otros procesos de interés en la evolución térmica de una estrella de neutrones que se desean investigar. Por ejemplo, el campo magnético puede tener un gran efecto sobre el transporte de calor ya que los agentes de transporte de energía como los electrones, siguen las líneas del campo. Es necesario tomar en cuenta este efecto en multiples dimensiones, lo cual incrementa el costo computacional para su cálculo.

Geppert, Küker & Page consideraron el efecto del campo magnético poloidal [32] y

toroidal [33] sobre la distribución de la temperatura superficial. Resolvieron ecuaciones de balance de energía y de transporte de calor en dos dimensiones, con simetría rotacional por el eje del campo. Mostraron que la solución del equilibrio (cuando la estrella se enfría pasivamente por fotones, tiempo $> 10^5$ años) tiene un perfil de la temperatura dentro de la estrella no-simétrico, especificamente que la combinación del las configuraciones de los campos en la corteza efectivamente limita el flujo de calor por la región ecuatorial formando puntos calientes en los polos magnéticos superficiales de tamaños diferentes. Se propone que estos *hot spots* pueden producir pulsaciones vistas en las curvas de luz de algunas estrellas.

Aguilera, Pons & Miralles [1] presentaron sus cálculos de la evolución térmica de estrellas de neutrones con campos magnéticos fuertes con configuraciones estáticas similares a las consideradas arriba. Mostraron como el campo magnético afecta la distribución de temperatura superficial,T_s, de la estrella tanto en la época de enfriamiento por fotones como durante los períodos tempranos de enfriamiento por neutrinos.

Contribución de la Autora Los modelos numéricos del enfriamiento en dos dimensiones de estrellas de neutrones magnetizadas esfericamente simétricas de Aguilera, Pons & Miralles [1] usan una combinación de métodos numéricos pseudo-espectrales (dimensión ángular) y de diferencias finitas (dimensión radial). Mientras los métodos espectrales usan representaciones globales de las ecuaciones de interés en la forma de polinomios de alto orden o series de Fourier, los métodos de diferencias finitas están basados en representaciones locales de polinomios de orden más bajo. Estos métodos espectrales pueden ser muy precisos para calculos computacionales grandes en multiples-dimensiones y también permiten una malla más grande reduciendo así el costo computacional. En contraste estos métodos pseudo-espectrales son especialmente afectados por la presencia de las condiciones de la frontera, tanto es así que impacta negativamente su estabilidad numérica y puede restringir el tamaño de las estapas temporales de la evolucíon aumentando así el tiempo de computación [103].

La intencíon de esta tésis es de tratar de usar un esquema completamente formado por diferencias finitas en cada dimensión, resolviendo la evolución térmica con pasos en el tiempo que siguen en magnitud a la edad de la estrella. Este modelo, que divide las etapas temporales para buscar la solución de balance de energía en cada dirección considerada, permite la precisión de segundo orden en el espacio y tiempo. Los resultados en dos dimensiones son comparables a los obtenidos en una-dimension para estrellas no-magnetizadas pero con efriamiento más eficiente. El modelo también tiene éxito para estrellas de neutrones fuertamente

magnétizadas.

Bosquejo La tésis está organizada de la siguiente manera: El Capítulo 3 presenta una breve historia del descubrimiento de estrellas de neutrones y los fenomenos associados que nos dejan con más preguntas sobre la naturaleza de la matéria densa. El Capítulo 4 describe los métodos numéricos mencionados anteriormente y sus aplicaciones a la evolucion térmica de estrellas de neutrones. Los efectos resultados de varias contribuciones a la microfísica son investigados por ejemplo el efecto de un campo magnético fuerte. El Capítulo 5 presenta la aplicación de los cálculos de la evolución térmica para explicar ciertos casos del fenómeno asociado con las estrellas de neutrones. El Capítulo 6 resume los resultados presentados en esta tésis y brinda una proyección del futuro del presente trabajo así como del futuro de la investigación de las estrellas de neutrones.

1.2. Estrellas de Neutrones

Nuestra visión presente de la estructura interna de una estrella de neutrones está ilustrado en la Figura 3.1. Por afuera donde la presión llega hasta $P = 0$ la estrella tiene una *atmósfera*, de unos pocos centímetros de espesor, sobre una capa delgada, de un centenar de metros de profundidad, llamada *envolvente*. En la parte superior de la envolvente está un *ocean*, donde la materia que era gaseosa en la atmósfera se vuelva líquida por el aumento de la presión, abajo del cual, a todavía mas alta presión, la materia está en un estado sólido. La atmósfera es la capa donde se emiten los fotones térmicos que se pueden detectar en rayos X y nos permiten "medir" la temperatura efectiva de la estrella, T_e, a través del modelado de su espectro. Globalmente, la envolvente funciona como una "cobija térmica", aislando la superficie del interior y determinando la temperature superficial,T_s, dada la temperatura interior T_b en su base. El calor proveniente del interior tiene que viajar dentro de la envolvente por una mezcla de composiciones químicas dependiente en el modelo teórico utilizado para describir la envolvente. Hay modelos suponiendo una composición de átomos ligeros (H, He) y algunos que suponen la presencia de especies más masivas como Fe. También, en esta zona la presencia o no del campo magnético en el modelo del envolvente cambia mucho la T_s esperada, aún cambia la distribución de T_s sobre la superficie. El rol de estos modelos en los cálculos del enfriamiento de las estrellas de neutrones es más elaborada en §3.3.7.

Mientras viajamos más hacia adentro de la estrella, la densidad ρ, y la presión P corre-

spondiente aumenta y el decaimiento-β inverso resulta en más especies ricas en neutrones. La composición del equilibrio depende en la densidad de la capa de matéria y la EOS particular. Por ejemplo, la EOS de BPS predice la presencia de ^{56}Fe hasta una densidad máxima de 8.1×10^6 g cm^{-3}, una serie de especies químicas hasta llegar a ^{118}Kr antes de cruzar un ρ_{drip} de 4.3×10^{11} g cm^{-3}. Esta capa se llama la *corteza exterior*.

El punto ρ_{drip} es definido por la densidad a la cual los neutrones sobre-abundantes ya no están todos confinados dentro de los núcleos: desde este punto la materia está compuesta de núcleos sumamente ricos en neutrones y rodeados de un líquido de neutrones "goteados", todo inmerso en un gas de electrones. Los modelos teóricos predicen que los núcleos están ordenados en una malla cristalina mientras los neutrones goteados forman un superfluido. La rotación de la estrella, examinado en más detaille en §3.4.1, crea vórtices del superfluido que pueden clavarse a los núcleos cristalizados. Esta descripción microscópica está ilustrada en el inserto B de la Figura 3.1. El desacoplamiento eventual de los dos componentes puede ser el mecanismo detrás del fenomeno de los "glitches", un tema explorado en §3.4 *Observaciones*.

Al aumentar mas la densidad y conforme la distancia entre los núcleos decrece resulta energéticamente favorable tener núcleos no esféricos: se vuelven alargados ("espaguetis"), anchos ("lasañas"), hasta casi fusionar solo dejando huecos ("queso suizo"). Esta fase de transición has sido apodada fase de "pasta nuclear" (ver el inserto A de la Figura 3.1). Los "espaguetis" aparecen cuando la densidad rebasa 10^{13} g cm^{-3} mientas la fase de "queso suiza" terminaría cuando la densidad rebasa 10^{14} g cm^{-3}: en este punto los "huecos" desaparecen y entramos en la región donde la materia es homogénea, el *núcleo*, o *carozo* de la estrella. (Mas detalle sobre la estructura y la ecuación de estados de la materia densa en la corteza se presentan en las secciones 3.2.2 y 3.2.3).

El núcleo de una estrella de neutrones esta definido por densidades más grandes que ρ_{nucl} y contiene $> 90\%$ de la masa. La matéria esta considerada como un fluido frio uniforme de neutrones en equilibrio-β con una fracción de protones, electrones y muones. La teoría indica que los neutrones siguen formando un superfluido mientras los protones forman un superconductor. Como en la corteza interior, la rotación de la estrella requiere la presencia de vórtices en el superfluido mientras en la presencia de un campo magnético el superconductor de protones sería de tipo II y el campo magnético estaría confinado en fluxoides: esta posible estructura está ilustrada en el inserto C de la Figura 3.1. Pero la region al centro de la estrella, donde la densidad supera 10^{15} g cm^{-3}, la historia se vuelve aun más misteriosa y está marcada por un *?* en la Figura 3.1. La presencia de hiperones está esperada así como

la de quarks deconfinados, pero la multitud de teorias de la matéria ultra-densa todavia necesita estar comprobada.

Y esto es el chiste. Desde la región de la pasta nuclear hasta la parte mas interna, la materia está en condiciones muy lejanas de las posibilidades experimentales terrestres y los modelos teóricos están plagados de muchísimas incertidumbres. La confrontación de predicciones teóricas con observaciones es necesaria para restringir el rango de incertidumbre de la teoría. Una herramienta muy poderosa en esta línea es el modelado de la evolución térmica de estrellas de neutrones y comparación de la predicciones de las varias teorías con observaciones, en particular mediciones de temperaturas superficiales T_s de estrellas de varias edades. Es la propuesta de esta tesis el extender los modelos existentes al incluir los efectos del campo magnético sobre la evolución de la estrella. En la presencia de un campo fuerte el transporte de calor dentro de la estrella es fuertemente alterado: de una descripción con simetría esférica (que es común en modelos de evolución estelar) tenemos que desarrollar modelos bi-, y tri-, dimensionales.

La siguiente sección describe los elementos que componen un modelo de enfriamiento de una estrella de neutrones.

1.3. Modelado Numérico del Enfriamiento de Estrellas de Neutrones

Estudiar el enfriemiento de una estrella de neutrones consiste en determinar su temperature interna en función de la posición en la estrella y del tiempo. En un modelo con simetría esférica esto significa calcular $T(r;t)$ mientras en un modelo esférico pero sin simetría tenemos que determinar $T(r,\theta,\phi;t)$, (r,θ,ϕ) siendo coordenadas esféricas. Dos ecuaciones rigen la evolución de T: conservación de energía y transporte de calor. El segundo está expresado por la ecuación

$$\boldsymbol{F} = -\kappa \boldsymbol{\nabla} T \tag{1.1}$$

(frecuentemente llamada "Ley de Fick") donde $\boldsymbol{\nabla} T$ es el gradiente de temperatura y $\boldsymbol{F}$ el flujo de calor, κ siendo la conductividad térmica. La conservación de energía se expresa como

$$\frac{\partial E_T}{\partial t} = C_v \frac{\partial T}{\partial t} = -\boldsymbol{\nabla} \cdot \boldsymbol{F} - \text{"perdidas"} + \text{"fuentes"} \tag{1.2}$$

donde E_T is la densidad de energía térmica, C_v el calor específico y "perdidas" representa los mecanismos de perdida de energá, esencialmente procesos de emisión de neutrinos, y "fuentes" la fuentes de calor que pueden ser, por ejemplo, reacciones nucleares o generación de calor por decaimiento del campo magnético. Designaremos estos dos términos por Q_ν y Q_h (ν por neutrinos y h por "heating") Estas dos ecuaciones se pueden juntar en un "ecuación del calor" generalizada como

$$\frac{\partial T}{\partial t} = \frac{1}{C_v}\left[\boldsymbol{\nabla}\cdot(\kappa\boldsymbol{\nabla}T) - Q_\nu + Q_h\right] \tag{1.3}$$

La micro-física involucrada en el cálculo de C_v, κ, y Q_ν está descrita en la secciones 3.3.2 hasta 3.3.5.

En el caso con simetría esférica, $\boldsymbol{\nabla} \to \frac{d}{dr}$ la Eq. (1.3) se escribe

$$\frac{\partial T}{\partial t} = \frac{1}{C_v}\left[\frac{1}{r^2}\frac{\partial}{\partial r}\left(\kappa r^2 \frac{\partial T}{\partial r}\right) - Q_\nu + Q_h\right] \equiv G(T) \tag{1.4}$$

(donde $G(T)$ simboliza todo el operador del lado derecho). Dada la complejidad de las funciones físicas C_v, κ, y Q_ν, tal ecuación tiene que resolverse numericamente:
- se discretiza la coordenada radial r en $r_0 = 0$, r_1, ... , r_i, ... , $r_I = R$
- se discretiza el tiempo t en $t_0 = 0$, t_1, t_2, ...
En cada punto de la malla radial las derivadas $\partial/\partial r$ implican que $\partial T_i/\partial t$ depende no solo de T_i pero también de T_{i-1} y T_{i+1} así que la versión discetizada en r de la Eq. (1.4) es

$$\frac{\partial T_i}{\partial t} = G(T_i, T_{i-1}, T_{i+1}) \tag{1.5}$$

Al discretizar también el tiempo tenemos una secuencia de temperaturas $T_i^{(n)}$ (es decir T en el punto r_i al tiempo t_n). Con esto podríamos integrar numericamente la Eq. (1.6) de manera trivial como

$$T_i^{(n+1)} = T_i^{(n)} + \delta t_n \times G(T_i^{(n)}, T_{i-1}^{(n)}, T_{i+1}^{(n)}) \tag{1.6}$$

(donde $\delta t_n \equiv t_{n+1} - t_n$). Se escojen valores iniciales $T_i^{(0)}$ en $t_0 = 0$, por ejemplo $T_i^{(0)} = 10^{10}$ K en toda la estrella y de la Eq. (1.6) se obtienen los $T_i^{(1)}$, luego los $T_i^{(2)}$, ... , de manera directa (después de escoger $\delta t_n = \delta t$ fijo).

Este método es desastroso !

Se llama "método explicito" y es *numericamente inestable* al menos que δt sea muy pequeño (satisfaciendo la llamada condición de Courant): si δt es demasiado grande los errores de

redondeo (inevitables en un calculo numérico que siempre usa un numero fínito de cifras significativas) crecen exponencialmente ! La solución a este problema es sencilla: se reemplaza la Eq. (1.6) por

$$T_i^{(n+1)} = T_i^{(n)} + \delta t_n \times G(T_i^{(n+1)}, T_{i-1}^{(n+1)}, T_{i+1}^{(n+1)}) \tag{1.7}$$

donde se reemplazan los $T_i^{(n)}$ por $T_i^{(n+1)}$ en el lado derecho. Es el llamado "método implicito" y la inestabilidad numerica desaparece !

El precio a pagar con el metodo implicito es que los $T_i^{(n+1)}$ a calcular aparecen dentro de G que es una función sumamente compleja. La manera de encontrar estos $T_i^{(n+1)}$ es por iteraciones:
1) hacemos un intento inicial $T_i^{(n+1,0)} = T_i^{(n)}$
2) calculamos el lado derecho de la Eq. (1.7) usando $G(T_i^{(n+1,0)}, T_{i-1}^{(n+1,0)}, T_{i+1}^{(n+1,0)})$
3) obtenemos los $T_i^{(n+1,1)}$ resolviendo la Eq. (1.7)
y regresamos a 2) usando ahora los $T_i^{(n+1,1)}$ en G, vamos a 3), ... y seguimos iterando k veces hasta que $T_i^{(n+1,k+1)} \simeq T_i^{(n+1,k)}$ con la precisión requerida. Se considera entonces que el procedimiento de aproximaciones sucesivas ha convergido y se puede pasar al paso siguiente en el tiempo, t_{n+2}.

La ecuación del calor, Eq. (1.3), tiene que ser complementada por condiciones de frontera y, tratando de estrella de neutrones, debe ademas incluir efectos de Relatividad General: la formulación completa está presentada en la sección 3.3.1. La sección 4.1 presenta la ecuación del calor con mas detalle y el metodo numérico implicito está descrito con detalle en la sección 4.2. La sección 4.3 finalmente presenta modelos realistas de enfriamiento de estrellas de neutrones en la aproximación de simetría esférica.

1.3.1. Modelos en 2D con campo magnético

La parte medular de esta tesis fue el extender los modelos de enfriamiento con simetría esférica a modelos bi-dimensionales con simetría axial en presencia de una campo magnético fuerte. El transporte de calor en la corteza está dominado por los electrones y estos están fuertemente afectados por campos magnéticos: la conductividad térmica κ se vuelve anisotrópica, pudiendo ser muchos ordenes de magnitud mas grande a lo largo del campo magnético que en la dirección perpendicular. La ecuación del calor, Eq. (1.3), en su forma bi-dimensional con efectos de relatividad general y en la presencia de un campo magnético fuerte está descrita en la sección 4.4. El método de resolución numérica es implicito pero

mucho mas complicado que en el caso con simetría esférica ya que la anisotropía de la conductividad térmica induce un fuerte acoplamiento entre las componentes r y θ del campo magnético $\boldsymbol{B}$ y del gradiente de temperatura $\boldsymbol{\nabla} T$ (ver la sección 4.4.2 para los detalles de la formulación). Las geometrías del campo magnético que se consideran están descritas en la sección 4.4.1: dos componentes dipolar poloidales, una con corrientes en la corteza y la otra con corrientes en el núcleo, y una componente dipolar toroidal confinada en la corteza. La componente toroidal es un campo magnético que no sale de la estrella y sus líneas de campo forman un "dona" magnética dentro de la corteza: actúa como una fuerte "cobija térmica" que impide el flujo de calor hacía la superficie y su efecto observable es el que la superficie es muy fría salvo en dos pequeñas regiones centradas en el eje de simetría del campo.

Los efectos de la anisotropía del transporte de calor en la corteza en presencia de una campo magnético fuerte, notablemente una componente toroidal, están descritos en la sección 4.4.4 donde se puede apreciar la complejidad de los perfiles de temperatura que se obtienen.

Finalmente, en el capítulo 5, se estudian cuatro casos específicos:
- Agregamos a los procesos de enfriamiento (que son emisión de neutrinos del interior y de fotones en la superficie) un procesos de "calentamiento" debido al decaimiento del campo magnético, sección 5.1. Este proceso permite mantener la estrella caliente durante mas tiempo se aplica al estudio de la evolución de los magnetares.
- Considerando la presencia de dos regiones calientes en la superficie, rodeadas de una fond frío, modelamos la emisión térmica de esta superficie la características observables, sección 5.2. Mostramos que esta peculiar distribución de temperature superficial (debida a la presencia de una componente toroidal del campo magnético) permite explicar la muy alta amplitud de la modulación observada en el caso del pulsar PSR J1119-6127.
- Extendemos el modelo de componente toroidal poloidal, es decir simétrica con respeto al ecuador magnético, a casos asimétricos, sección 5.3. Esta configuración asimétrica resulta en una distribución de temperature superficial también asimétrica y aplicamos este escenario para interpretar las observaciones de la estrella de neutrones en el remanente de supernova "Puppis A".
- Como último estudio, consideramos un caso extremo, el de una estrella de quarks, ó "Strange Star", sección 5.4. En este escenario, el núcleo de la estrella está constituido en un 100% de materia de quarks, en vez de materia bariónica, y la corteza interna (que debería contener neutrones goteados) no existe. Tales estrellas de quarks solo pueden tener

una corteza externa que es muy delgada. Al incluir una componente poloidal del campo magnético en esta corteza mostramos que no resulta en una distribución de temperatura superficial tan diferenciada como en el caso de una estrella de neutrones y no aparecen estos dos regiones calientes rodeadas de un fondo frío. Esto implica que estrellas compactas con "hot spots" no se pueden interpretar como siendo estrellas de quarks. Este argumento no permite concluir directamente que estas estrellas compactas no son estrellas de quarks, ya que otro escenario (no descrito a la fecha !) podría existir, pero hace muy sospechoso un escenario de estrellas de quarks.

Posibles extensiones de este trabajo se presentan en el último capítulo 6.

Chapter 2

Introduction

Increasingly improved astronomical observations of compact objects such as pulsars and other neutron star phenomena has created the need for a comprehensive physical description of matter around nuclear density. In neutron star cores the density can go well beyond, the properties of which are still quite mysterious though their importance in governing observable spectra is increasingly evident. One such aspect in determining the observable surface temperature, spectrum and timing properties is heat transport within the star. In the outer less dense layers the properties of matter is much better understood partly due to experimental particle physics results performed on Earth and more thoroughly tested mathematical treatments of particle interactions in the sub-nuclear regime. This insulating outer layer takes the heat generated in the core and determines the resulting surface temperature profile which in turn is observed and interpreted, thus providing a window into the depths of compact matter, the likes of which is irreproducible on Earth.

2.1. Modeling Thermal Evolution

It is generally accepted that neutron stars are formed in the cores of supernova explosions with extremely high internal temperatures of $T \gtrsim 10^{11}K$. In the first few seconds of their lives the temperature of their nuclei drop to $10^{10} - 10^{9}K$ due to neutrino emission, the dominant form of energy transport until $T \sim 10^{8}K$ when photons begin to dominate. Solving the *Energy Balance* within a neutron star enables us to theoretically model it's cooling and establish the timescales of these aforementioned cooling eras while surface temperature observations in combination with inferred neutron star ages (e.g. from the association with

Supernova Remnants, SNr) are used to support or reject these theories. Meanwhile, information about T-sensitive ingredients of the Energy Balance such as transport coefficients (e.g. thermal conductivity, κ), transition to superfluid staes and solidification of crust material can be deduced.

Of particular interest at the moment is evidence of the transition to superfluid states. Recently, Heinke & Ho [47] demonstrated for the first time direct evidence of the rapid cooling of a neutron star. They analyzed data from Cassiopeia A (*Cas A*), a neutron star discovered in the 1999 *Chandra* "first light" observations [102] associated with the historical 1680 supernova [6], and saw that it's temperature dropped from $2.12 \times 10^6 K$ in the year 2000 to $2.04 \times 10^6 K$ in 2009 - a decrease of 4% en nine years, larger that that expected from cooling from neutrinos alone! Soon afterwards, Page et al (2011) [75] proposed that the cooling in Cas A was to due the turn-on of superfluidity in the star's core and predicted that this rapid cooling would continue in the next dacades. In order to show that the thermal evolution of Cas A could be explained from cooling precoesses from within a neutron star, a numerical solution to Energy Balance and Heat Transport calculations including general relativistic effects and pairing was used. The model solved these equations in a one dimensional (radial) spherically symmetric star with input microphysics decribed in [73] and [74].

One-dimensional radial cooling models are very powerful and successfully show the effect of physical properties that are dependant on temperature and density assuming a spherically symmetrical star with uniform density levels. Comparisons between observations of effective surface temperatures and theories of the state, or *Equation of State, (EOS)*, of dense matter, superfluid properties of dense matter, neutron star crust composition and stellar mass can be made in order to eliminate some of the myriad of possibilities [73]. It is however desirable to investigate in detail processes of the thermal evolution of a neutron star. For example, the intrinsic magnetic field can have a large effect on heat transport since energy carriers such as electrones are strongly influenced by field lines. Magnetic field configurations vary in two and three dimensions, thus this effect is necessarily considered in multiple dimensions. The challenges of scaling up spatial dimensions then become stability of the numerical method and an increase in the computational cost of the calculation.

Geppert, Küker & Page considered the effct of a poloidal magnetic field [32] as well as the addition of a toroidal component [33] on the temperature distribution within a neutron star and it's resulting surface temperature anisotropy. The equilibrium solution of Energy Balance and heat transport was calculated in two dimensions (radial and polar) symmetrical

about the magnetic axis and showed that at equilibrium, when the star is passively cooling by photons ($> 10^5$ *years*) it's interior temperature profile is asymmetric. Specifically, the combination of the magnetic field configurations within the neutron star crust effectively blanket heat flow from the core creating hot polar regions of different sizes surrounded by a cooler equatorial belt. It is propsed that these *hot spots* can produce pulsations in the light curves of some neutron stars.

Aguilera, Pons & Miralles [1] presented their thermal evolution calculations with static magnetic field configurations similar to the above work. They showed that the magnetic field affects the distribution of surface temperature, T_s, during neutrino-cooling early life of a neutron star as well as the later photon cooling era.

2.2. Contribution of the Author

The numerical models of two-dimensional cooling of spherically-symmetric magnetized neutron stars from Aguilera, Pons & Miralles [1] use a combination of pseudo-spectral numerical methods (polar direction) and finite differences (radial direction). While spectral methods use global representations of the equations of interest in the form of higher-order polynomials or Fourier series, finite difference methods are based on local representations of lower-order polynomials. Spectral methods can be more accurate for large multi-dimensional computations, such as solving heat transport within magnetized neutron stars, and allow for larger grid sizes thus lowering computational cost. They are, however, particularly sensitive to the presence of boundary conditions, so much so that their numerical stability is negatively affected and can severely restrict time-step sizes thus increasing computing time [103].

It is the intention of this thesis to attempt to use an entirely finite differencing scheme in each dimension thus solving heat transport within a neutron star with timesteps that increase on par with stellar age. This model, which will divide each timestep in order to find the solution to the Energy Balance equation in each direction considered, will allow for second-order accuracy in both time and space, with results that are comparable to, if not slightly more efficient than, their one-dimensional (radial) couterparts for unmagnetized neutron stars. The parallelized model code also has success with strongly magnetized neutron stars with a calculation time on the order of minutes for an age up to the end of the photon cooling era ($\sim 10^5$ *years*).

2.3. Outline

This thesis is ordered by the following scheme. Chapter 3 presents a brief history of the theory and the eventual discovery of neutron stars and the myriad of associated phenomena which leaves us with more questions than answers regarding the nature of dense matter. In order to illuminate this mystery the following Chapter 4 describes the numerical methods mentioned above and their application to the thermal evolution of neutron stars. Results of the effects of various contributions to the input microphysics, such as superfluidity and a strong internal magnetic field, are investigated. The next Chapter 5 presents the application of thermal tranport calculations to explain certain phenomena associated with particular known neutron stars. The concluding Chapter 6 summarizes the results presented within this thesis. A description of the possible work to be continued in the Future is also presented with regards to this project and neutron star research in general.

Chapter 3

Neutron Stars

3.1. History

The neutron was discovered in 1932 by Sir James Chadwick [19] and by the following year Walter Baade and Fritz Zwicky proposed the existence of the neutron star [7]. In an effort to explain what powers a supernova, Baade and Zwicky correctly hypothesized that this power could be derived from the release of gravitational binding energy during the creation of a neutron star. As a massive star approaches the end of its life, nuclear fusion runs out in its core and the star collapses resulting in a compact remnant and a supernova (Type II, Ib or Ic). The newly created compact star could be a white dwarf, neutron star, or black hole depending on the size on the progenitor star. Since that time researchers investigating the properties of dense matter have worked on a theory to describe the state of matter inside a neutron star, whose core density could possibly increase beyond that of nuclear matter.

3.2. The Interior Physics

In order to determine the structure and composition of a neutron star, a description of the physical properties of dense matter, also known as it's *Equation of State (EOS)*, is necessary. An EOS starts with the basic laws of thermodynamics for a certain number of particles, N, in a volume, V, in a Lorentz cell which is co-moving within the fluid stellar material. It is expressed in terms of the Pressure, $P(\rho)$ where ρ is the density whose lowest energy state gives the local composition.

There are several important assumptions regarding the initial conditions in the life of

a neutron star: after proto-stellar nuclear burning sufficient time has passed such that the tempertaures of interest are lower than those necessary for nuclear reactions and the star can be considered to be in thermodynamic equilibrium ; and is otherwise considered to be *cold* with $T = 0$ (cold catalyzed matter).

3.2.1. Equations of Stellar Structure

In order to ultimately model (numerically) the physical processes of a neutron star, one must start with it's general structure. In order to properly consider such a compact object as a neutron star, whose density exceeds $\rho > 10^{14}$ g cm^{-3} within it's core, relativistic effects must be considered.

A spherically symmetric spacetime geometry, in the usual Schwarzschild coordinates (t, r, θ, ϕ), takes the following form:

$$ds^2 = -e^{2\phi}c^2dt^2 + \frac{dr^2}{1 - 2Gm/rc^2} + r^2d\Omega^2 \tag{3.1}$$

where the radial proper length is

$$dl = dr/\sqrt{1 - 2Gm/rc^2} > dr \tag{3.2}$$

and proper time $d\tau = e^{\phi}dt < dt$.

Coupling Einstein's equations to a perfect fluid energy momentum tensor gives the following standard structure equations,

$$\frac{dm}{dr} = 4\pi r^2\rho \tag{3.3}$$

$$\frac{dP}{dr} = -\frac{Gm\rho}{r^2}\left[1 + \frac{P}{\rho c^2}\right]\left[1 + \frac{4\pi r^3P}{mc^2}\right]\left[1 - \frac{2Gm}{rc^2}\right]^{-1} = -(\rho c^2 + P)\frac{d\Phi}{dr} \tag{3.4}$$

$$\frac{d\Phi}{dr} = \frac{1}{c^2}\frac{Gm}{r^2}\left[1 + \frac{4\pi r^3P}{mc^2}\right]\left[1 - \frac{2Gm}{rc^2}\right]^{-1} = -\frac{dP}{dr}\left[\rho + \frac{P}{c^2}\right]^{-1} \tag{3.5}$$

where the latter is the Tolman-Oppenheimer-Volkoff (TOV) equation for hydrostatic equilibrium and (3.3) and (3.5) give the mass function $m = m(r)$ and the gravitational potential $\Phi = \Phi(r)$ respectively.

From (3.4) one see that $c^2d\Phi/dr$ plays the role of the gravitational acceleration, and thus $c^2\Phi$ is naturally interpreted as the gravitational potential.

Boundary conditions in the centre, where $r = 0$ is dictated by the regularity of the geometry of (3.1):

$$m(r = 0) = 0 \tag{3.6}$$

while $P = P(\rho)$, which is a relation particular to the Equation of State (EOS) to be further discussed below, will give the central pressure, P_c, depending on the corresponding free parameter, ρ_c:

$$P(r = 0) = P_c \tag{3.7}$$

At the outer boundary $r = R$, the radius of the star, and $\rho(R)$ is arbitrarily set to a low value (i.e. for the models presented in this project, R is determined by the EOS value of r at a boundary density of $\rho_b = 10^{10}$ g cm^{-3}). Densities lower than ρ_b are considered part of the *envelope* and are treated as an outer boundary condition which will be discussed below.

Equation (3.5) can be scaled, given its linearity, to always fulfill the following condition:

$$e^{\phi(R)} = \sqrt{1 - \frac{2GM}{c^2 R}} \tag{3.8}$$

The interior spacetime geometry is connected across the surface (defined by R) of the star to an exterior Schwarzschild field determined by $M = m(r)$ [72].

With these conditions in place, the EOS is guaranteed to be temperature independent, thus greatly simplifying the algorithm to be used to model neutron star cooling, the equations for which will be described in the next section.

3.2.2. Equation of State of cold, dense matter below *Neutron Drip*

An isolated neutron star ultimately cools to $T = 0$ and it's structure is calculated using a degenerate EOS. To begin with, a single fermionic species can be considered for simplicity. In the pioneering article of 1931, Chandrasekhar [20] chose electrons at $T = 0$ in order to describe an ideal Fermionic gas to characterize White Dwarfs and found a maximum mass of $1.4M_\odot$ (the *Chandra limit*). In 1939, Oppenheimer & Volkoff (OV) [68] expanded on Chandrasekhar's idea to describe neutron stars, objects that are much more dense than their White Dwarf counterparts, and found a maximum mass of $0.7M_\odot$. This seemed very small, so much so that it was doubtful that sufficient observable luminosity could be produced. Interest in these objects then diminished.

It was also evident that an ideal Fermi gas was insufficient to describe dense matter. Positive charges are not actually uniformly distributed throughout the gas, but are concentrated around nuclei of charge Z. This has the effect of lowering the energy and pressure of the ambient electrons, which have more distance between each other than with their respective nuclei, and therefore the attractive forces dominate over repulsive forces. The density increases with increasing depth within the star and crosses a point at which the electrons become degenerate. In this region Coulomb effects become important and ions form a crystal which maximizes the distance between them, $E_c = E_{e-e} + E_{e-i}$. The effect is electrostatic and in 1949 Feynman, Metropolis & Teller [27] added these corrections to the ideal degenerate electron gas EOS.

As well as electrostatic corrections, the inclusion of inverse β-decay, described by the following formula, was important:

$$e^- + p \rightarrow n + \nu \tag{3.9}$$

It is assumed here that neutrinos, ν, are massless and escape the star without interactions. β-decay is blocked when the density is sufficiently great that the Fermi energies, E_F, are completely filled with electrons until the level at which the emitted electron would have filled. Assuming the simple case of a *cold n-p-e gas*, neutrons, electrons and protons in equilibrium ($\mu_e + \mu_p = \mu_n$) and neutral charge ($n_e = n_p$) the EOS and the composition can be calculated using the mass fractions, X_e, X_p and X_n.

In 1958, Harrison & Wheeler caculated the EOS considering inverse β-decay and β-equilibrium between relativistic electrons and nuclei using a mass function, $M(A, Z)$. However the nuclei have discrete values of A and Z and in 1961 Salpeter included these "shell" effects using the EOS of Chandrasekar as a base including the Coulomb correction. A decade later in 1971, Baym, Pethick & Sutherland ("BPS" [14]) improved upon the results of Salpeter using a new improved semi-emperical mass formula in order to determine the equilibrium composition. Besides shell effects, BPS included lattice energy of the crystal phase. However, considering that the pressure P is continuous causes discontinuities in the number densities of n and p due to phase transitions between the nuclear species. In order to smooth the composition between layers the following methods are implemented: a Maxwell construction determines P in the transition; or a Gibb's construction minimizes the Gibbs free energy, g, at constant P. Both EOS join with the EOS of Chandrasekhar for White Dwarfs and give a maximum mass similar to that of OV, $M_{NS} \sim 0.7 M_\odot$.

At the moment we have the following picture of the physics of the interior of the neutron star: considering nuclear forces alone, the equilibrium nuclear structure would be a nucleus of unlimited size. Including repulsive Coulomb forces which are so great that fission can occur at low densities, an equilibrium is reached at $A = 56$ (^{56}Fe). Adding relativistic electrons and inverse β-decay produces more neutrons in the stellar core and Coulomb forces become relativly weak and unimportant. When the density reaches 4×10^{11} g cm^{-3} the fraction of neutrons to protons, n/p, reaches a critical level and the neutrons begin to *drip* out of the nuclei. This point is refered to as the *neutron drip* point and is described by ρ_{drip}. For $\rho > \rho_{drip}$ the electrons, ion nuclei and "free" neutrons coexist. Furthermore, for $\rho > 4 \times 10^{12}$ g cm^{-3} the neutrons replace the electrons as the dominant constituent to the pressure.

3.2.3. Equation of State of cold, dense matter above *Neutron Drip*

While the theoreticians improved upon the physical picture of neutron stars, observers were making incredible discoveries. In 1962 Giacconi [36] discovered cosmic non-solar x-ray sources and interest in neutron stars was reignited. A few years later, in 1967, Jocelyn Bell and her supervisor Anthony Hewish, made the monumental discovery of radio pulsars [49]. At first, these highly regular radio pulses were interpreted as possible signals from extraterrestrials, but soon enough were correctly attributed by Gold (1968) [38] to spinning neutron stars. The following year the "Crab" and "Vela" pulsars were discovered indicating that neutron stars were indeed born from the violent explosions of supernova. Furthermore, it was observed that the Crab pulsar was slowing down and Gold (1969)[39] showed that the energy loss was similar in magnitude to the rotational energy necessary in order to give it it's power. Neutrons had then been observed directly and initial mass measurements did not indicate something as small as the star resulting from the calculations of OV but rather something akin to the Chandra limit, $M_{NS} \sim 1.3 M_{\odot}$. It was evident that something was missing from the EOS and that we had to improve our understanding of matter at densities beyond ρ_{drip}.

For densities up to ρ_{nucl} the picture of dense matter was well understood and the system could be treated as a non-relativistic many-body Schrödinger equation. Matter in equilibrium is composed of neutron-rich nuclei forming a Coulomb lattice, free electrons and neutrons. While the density approaches ρ_{nucl} the nuclei dissolve and start to join together. The pressure, P, is dominated by neutrons interacting via strong forces. For densities be-

yond ρ_{nucl} the "meson clouds" surrounding the nucleons start to overlap and the system can be treated as a local group of particles interacting via two-body forces to which three- and more- body forces also have to be added. Until $\rho \sim 10^{15}$ g cm^{-3} the nuclear potential from nucleon-nucleon interactions (NNI) must be described and a method to solve the many-body problem found. Different potentials result in different EOS, but which is the correct one? Furthermore, for $\rho > 10^{15}$ g cm^{-3} the picture is even more mysterious such that it is expected that the composition would contain hyperons and relativistic NNI would have to be treated.

In 1971, Baym, Bethe & Pethick (BBP [13]) used a mass formula determined from many-body calculations. As well, they included the effect of a neutron gas on the surface energy of the nuclei they surround and the effect of the nuclear Coulomb lattice energy. It was deemed the "compressible liquid drop" model. Their EOS had the following consequences: free neutrons accounted for an increasingly significant fraction of the pressure with increasing density; the adiabatic index, Γ, decreased dramatically close to ρ_{drip} and does not return to $\Gamma = 4/3$ until $\rho \geq 7 \times 10^{12}$ g cm^{-3} resulting in a range of densities that could not support a stable neutron star; nuclei survive until a ρ of 2.4×10^{14} g cm^{-3} after which the matter forms a nuclear liquid; beyond this density the contribution of mesons to the EOS must be incorporated.

In a pioneering work, Negele & Vautherin (1973)[66] calculated the EOS for matter beyond ρ_{drip} using NNI from n-n scattering data with variational methods. Their calculation is based on the many-nucleon theory of Hartree-Fock with the semi-empirical NNI of cold catalyzed matter above ρ_{drip} sufficient to determine the structure of the level of neutron-rich nuclei. Haensel, Zdunik & Dobaczewski (hereafter refered to as HZD, 1989) [46] expanded upon the aforementioned methods using a Hartree-Fock-Bogolyubov scheme to calculate lattice energies of the nucleons included in NNI. This method allowed the authors to reproduce nuclear properties seen in the laboratory and predicted the nuclear shell structure expected in the neutron star crust. During the 1970's, it became obvious that NNI alone would be insufficient to describe the properties of nuclear matter. NNI saturates at high densities thus underbinding ^3H. This problem was resolved with the addition of ρ-dependant 3-body terms to the *Urbana 14 (U14)* model. In 1981, Friedmann & Pandharipande [29] derived models with three-body interactions (TI). The terms of these models have energies fixed to the saturation density of nuclear matter and the binding energy of ^3H. In the 1990's, the Nijmegen group created a database of NN scattering data for energies below 350 MeV collected from 1955 to 1992. The data were sufficiently precise in order to determine phase

changes and mixing parameters. The *Argonne* v_{18} model was born from this great effort by the Wiringa group (1995)[108]. In the same year, Pudliner and colleagues [86] expanded the model *Urbana* to UIX. In 1998, Akmal, Pandharipande & Ravenhall (APR)[2] combined the models of *A18*, *U1X* and added δ_ν *relativistic boost interactions* arriving at a maximum neutron star mass of $2.2M_\odot$.

A combination of the EOS of APR for the stellar core ($\rho_{core} > 1.6 \times 10^{14} g\ cm^{-3}$), and NV ($\rho_{core} > \rho > \rho_{drip}$) and HZD ($\rho_{drip} > \rho > 10^{10} g\ cm^{-3}$) for the inner and outer crust respectively is used in this project, the results of which for a model star of $1.4M_\odot$ are presented in the Chapter "A Virtual Laboratory". Since we are, in this work, concentrating on the effect of a strong magnetic field in the thermal evolution of the crust, we will not, for the time being, explore scenarios with some form of "exotic" matter present in the core (see, e.g., [76] for a presentation of "exotic" phases).

3.2.4. The Complete Picture? The General Structure of Neutron Stars

Typical neutron stars have masses between 1.34 and $2.1M_\odot$ with corresponding radii between 10 and 20 km [60]. Their cores are thought to be a homogenous quantum liquid of neutrons and protons and possibly more exotic species. Inwards of $\sim 1000 - 500$ m, the stellar layers are comprised of a solid crust and envelope of subsequently less-dense nuclear matter covered with a thin atmosphere (Fig. 3.1).

Though thin, the atmosphere on a neutron star is critical when understanding the emitted thermal Flux, F, we get from observations. It may contain light or heavy elements and may or may not be magnetized, all crucial parameters in modelling observed spectra. The envelope may be 10's of meters thick and acts as an insulator between the surface and the hot stellar interior. It consists of matter that is not yet fully degenerate, the composition of which may be standard among stars of a particular mass or may vary from case to case, perhaps depending on if the star is in an accreting system or isolated.

Unlike in the core, matter in the crust is inhomogenous, containing a lattice formed by nuclei immersed in a quantum liquid of electrons. At densities greater than the neutron drip point ($\rho_{drip} \sim 4 - 7 \times 10^{11}$ g cm^{-3}), free neutrons join the mix, likely as a superfluid (see Figure 3.1 Inset B). Stellar rotation could form vortices in this nuclear superfluid which may actually pin on the nuclei. Generally, the superfluid portion of the star is moving faster

than the solid crust and occasional pinning of these vortices to lattice nuclei could cause a temporary increase in pulsar spin frequency (a.k.a. *Pulsar Glitches*).

As densities continue to increase towards nuclear density, nuclei become elongated, then flattened - termed *Pasta phases*. The situtaion is then inverted as the superfluid neutrons that once permeated the *pasta* now form bubbles in the *Swiss cheese*-like proton + neutron quantum liquid surrounding it. Inset A of Figure 3.1 shows the idea of this complicated phase transition, the physics for which are still being studied [87] so that they may be included in neutron star modelling. This transition from *core* to *crust* occurs at a density slightly lower than ρ_{nucl}, currently thought to be at $\rho_{cc} \sim 1 - 2 \cdot 10^{14}$ g cm^{-3} for matter at non-zero pressure comprised of 95% neutrons and 5% protons.

Their cores reach nuclear densities $\gg \rho_{nucl}$ and contain $> 95\%$ of their mass, whose exact composition is still a mystery but is generally thought to be a homogenous superfluid of degenerate neutrons and superconducting degenerate protons. Figure 3.1 Inset C shows a likely representation of vortices, formed from rotation of the star, containing this superfluid interlaced with magnetic field *fluxoids* from the superconductor.

The inner core is truly mysterious (marked with a *?* in Figure 3.1) and one of the ultimate goals of neutron star modelling is to narrow down it's composition.

3.3. Neutron Star Cooling

3.3.1. Cooling and The Energy Balance Equation

When looking at neutron star thermal evolution one considers internal temperatures in the range of $\sim 10^7 - 10^{10} K$. In this range neutrinos have a mean free path much larger than R and leave the star as soon as they are produced. Taking this into account, along with reletivistic effects, energy balance considerations give the following (from [73] Appendix B):

$$\frac{d(Le^{2\Phi})}{dr} = -\frac{4\pi r^2 e^{\Phi}}{\sqrt{1 - 2Gm/rc^2}} \left(\frac{dU}{dt} + e^{\Phi}(Q_\nu - Q_h) \right) \tag{3.10}$$

where L is the internal luminosity and Φ is gravitational potential. The other quantities are the internal energy U, the neutrino emissivity (heat loss) Q_ν and the heating rate Q_h, all three expressed per unit volume. The inner boundary condition is necessarily,

$$L(r = 0) = 0 \tag{3.11}$$

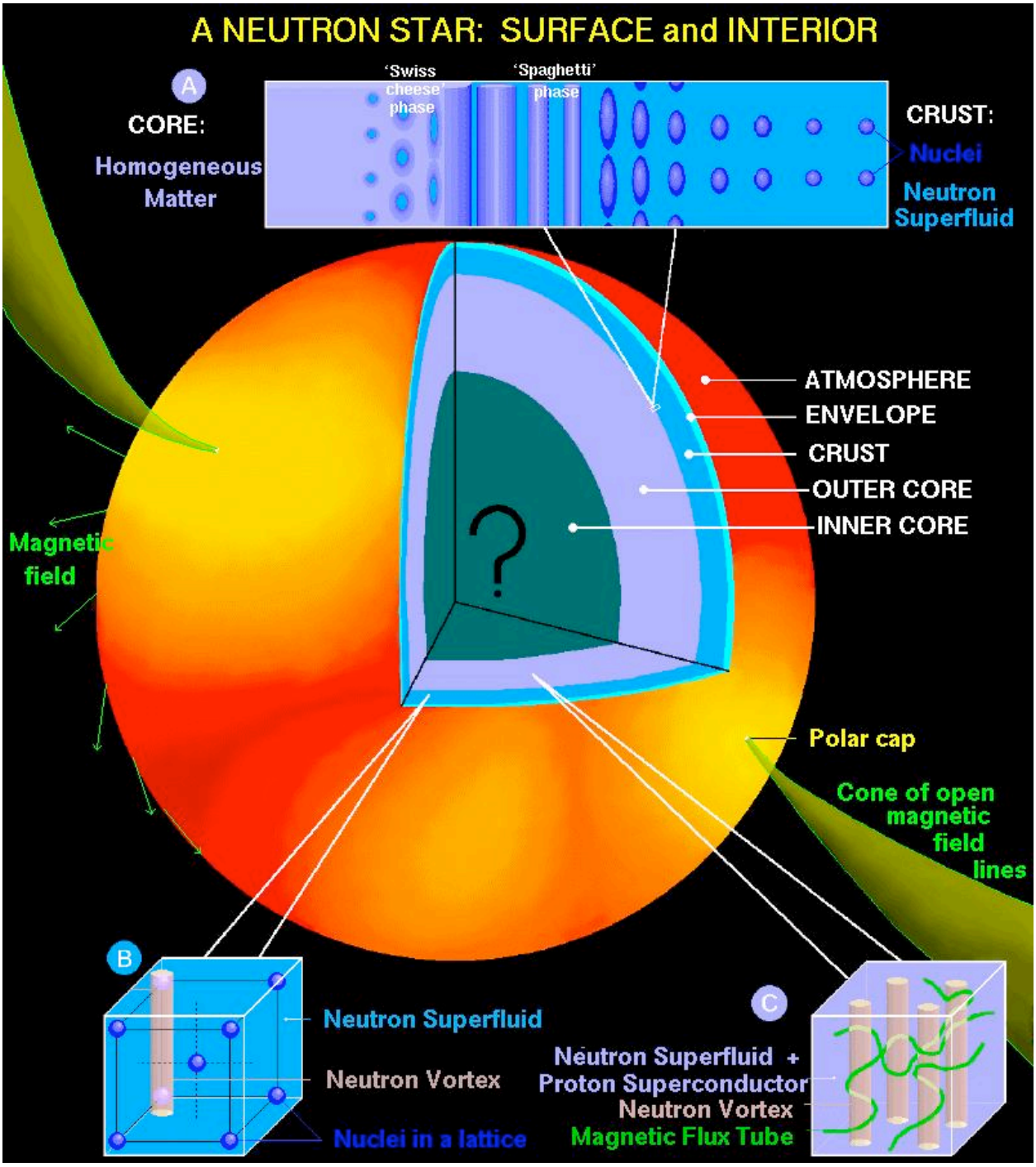

Figure 3.1 Theorists view of the interior of a neutron star (Artist: Dr. Dany Page)

which simply states that there are no point energy sources or sink at the center of the star.

In order to rewrite the equation in terms of the temperature, T, the following equivalencies can be applied:

$$\frac{dU}{dt} = \frac{dU}{dT}\frac{dT}{dt} = C_v \frac{dT}{dt} \tag{3.12}$$

where C_v is the specific heat at constant volume, which equals the specific heat at contant pressure, C_p, for degenerate matter, per unit volume. Then Eq. (3.10) reads

$$\frac{d(Le^{2\Phi})}{dr} = -\frac{4\pi r^2 e^{\Phi}}{\sqrt{1-2Gm/rc^2}}\left(C_v \frac{dT}{dt} + e^{\Phi}(Q_\nu - Q_h)\right) \tag{3.13}$$

Energy transport is obtained from Fick's law, $\vec{F} = -\kappa\vec{\nabla}T$, which expresses the energy flux $\vec{F}$ in term of the T-gradient through the thermal conductivity κ. With spherical symmetry only the radial direction has to be considered and, with GR effects properly included, gives

$$\frac{d(Te^{\Phi})}{dr} = -\frac{1}{\kappa}\frac{Le^{\Phi}}{4\pi r^2\sqrt{1-2Gm/rc^2}} \tag{3.14}$$

where T is the local temperature. Te^{Φ} is usually referred to as the *redshifted temperature* and the term *isothermal* refers to this relativistic term being constant, i.e., r independent. This equation needs an outer boundary condition

$$T_b = T(L_b) \tag{3.15}$$

which states that the outer boundary temperature (mentioned above) is related to the luminosity, L_b, at this level. The level is chosen so that L_b is equal to the total photon luminosity of the star, $L(r = R) = L_R$, which in turn can be expressed in terms of the effective temperature, T_e, and the Stefen-Boltzmann constant σ_{SB}:

$$L_R \equiv 4\pi R^2 \sigma_{SB} T_e^4 \tag{3.16}$$

thus relating $T_b = T_b(T_e)$ dubbed the $T_b - T_e$ *relation* which will be discussed later in terms of outer envelope models, the outer layer of the star whose thermal evolution must be treated differently for it's lower densities.

The quantities T, R and L shown above are quantities local to the star, however in principle these values taken *at infinity* should be measurable. The following conversions must then be taken is order to compare theoretical results with observations:

$$T_e^{\infty} \equiv T_e e^{\Phi(R)} \tag{3.17}$$

$$R^{\infty} \equiv Re^{-\Phi(R)} \tag{3.18}$$

$$L^{\infty} \equiv e^{2\Phi(R)} L(R) = 4\pi R^{\infty 2} \sigma_{SB} T_e^{\infty 4} \tag{3.19}$$

Measuring these observables is, of course, no trivial task and will be touched on in §3.4.

3.3.2. Pairing

The Cooper theorem (1956) [23] states: the Fermi surface of a degenerate system of fermions become unstable in the presence of an attractive interaction between the particles (i.e. the formation of Cooper Pairs) whose momenta lie close to the Fermi momentum. This instability results in an energy gap Δ in the energy spectrum around the Fermi energy such that no particle can have an energy between $E_F - \Delta$ and $E_F + \Delta$. This is illustrated when considering the excitiation energy spectrum for a single particle:

$$\left.\frac{\partial \varepsilon(p)}{\partial p}\right|_{p=p_F} \equiv \frac{p_F}{m^*} \equiv v_F \tag{3.20}$$

where m^* is the effective mass and p_F, v_F are the Fermi momentum and velocity. For momenta close to p_F we can write:

$$\varepsilon(p) = E_F + v_F(p - p_F) \tag{3.21}$$

where the Fermi energy, E_F is the value of $\varepsilon(p)$ at the Fermi Surface. Normally, $\varepsilon(p)$ would vary smoothly across the Fermi Surface but when conditions for pairing are met the aforementioned gap, Δ, appears:

$$\varepsilon(p) = E_F - \sqrt{v_F^2(p - p_F)^2 + \Delta^2} \text{ for } p < p_F, \tag{3.22}$$

$$\varepsilon(p) = E_F + \sqrt{v_F^2(p - p_F)^2 + \Delta^2} \text{ for } p > p_F \tag{3.23}$$

Neutron star matter with a temperature lower than this latent heat from pairing, i.e $kT \lesssim \Delta$, will be expected to be in a superfluid or superconductive state. The temperature associated with Δ is referred to as the critical temperature, T_c, such that for matter with $T > T_c$ we expect Δ to vanish and its behavior to correspond to a Fermi liquid. For $T \leq T_c$ the second order transition to superfluidity and superconductivity should occur and Δ will continue to

grow as the temperature continues to drop. The gap, Δ, and Tc, is much studied and, from BCS theory (Bardee, Cooper & Schreiffer, 1957 [12]), has a value at $T = 0$ of

$$k_B T_c \approx 0.57\Delta(0) \tag{3.24}$$

Furthermore, the *weak coupling approximation* estimates

$$\Delta(0) \sim E_F e^{-1/N(0)V}, \tag{3.25}$$

where $N(0)$ is the density of states at the Fermi surface and is equivalent to,

$$m^* p_F/\pi^2\hbar^3 \ , \tag{3.26}$$

where V is the pairing potential and it's presence implies that accurate calculations are very difficult, particularly because of its exponential dependence. V depends on the scattering length of an interation, a, which is negative for attraction. However, Cooper pairs have a coherence length great enough that it may comprehend many other particles. These particles could react with the pair thus *screening* their interaction, a process called *medium polarization*. Including this effect, termed *Beyond BCS*, reduces Δ in the following way,

$$\Delta(k_F) \rightarrow\sim 0.45\Delta_{BCS}(k_F) \tag{3.27}$$

The gap has been reduced by more than a factor of two which in turn reduces its corresponding T_c.

There are no obvious attractive interactions for electrons and muons, so they are not considered for the T_c of interest. However nucleons (i.e. neutrons, protons) do have attractive interactions and Cooper pairs can appear in various spin-orbital angular momentum states. Those expected for a neutron star are the $^1S_0$ channel for lower densities (i.e. the neutron star crust, see Inset A of Fig. 3.1) and $^3P_2$ for higher densities, i.e. the core) ([101], [75]). The $^1S_0$ channel for neutrons has been the most studied and when comparing Fig. 3.2, Fig. 3.3, and Fig. 3.4 the range of T_c is not so vast as for the $^3P_2$ or the proton $^1S_0$ channels. This large uncertainly in T_c is partly why the composition and underlying physics of the very core of neutron stars is still such a mystery (see *?* of Figure 3.1). Is the entire proton population of the core superconducting, or only the outer, lower density shell?

3.3.3. Specific Heat

The core of a neutron star represents roughly $\sim 90\%$ of its mass and thus is the main contributor to the overall specific heat of the star. The total specific heat per unit volume

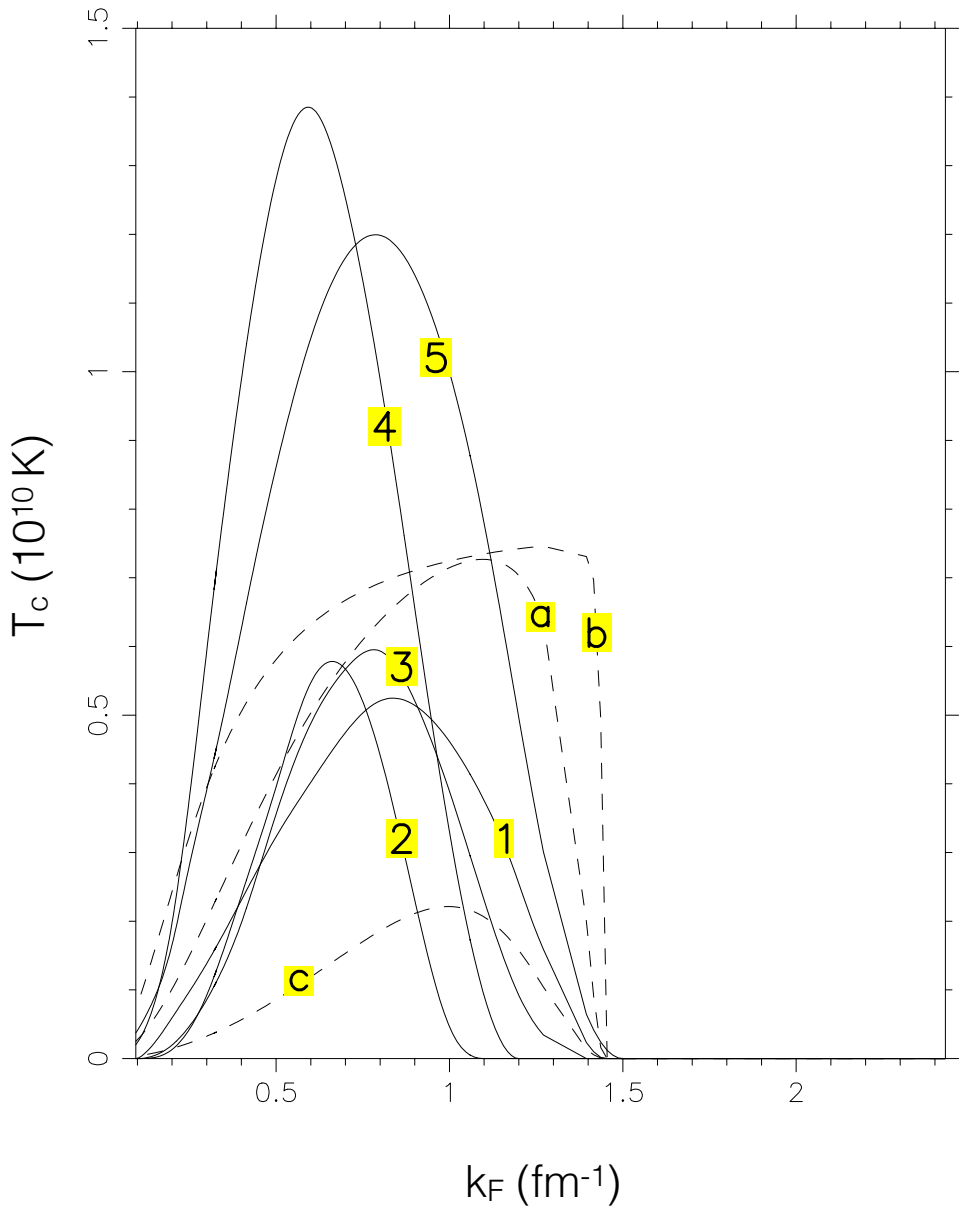

Figure 3.2 Neutron $^1S_0$ Pairing critical temperature, T_c, as a function of neutron Fermi momentum, $k_F(n)$, from neutron drip to the stellar centre. 1: [94], 2: [22], 3: [106], 4: [35], 5: [30], a: [109], b: [110], c: [110]

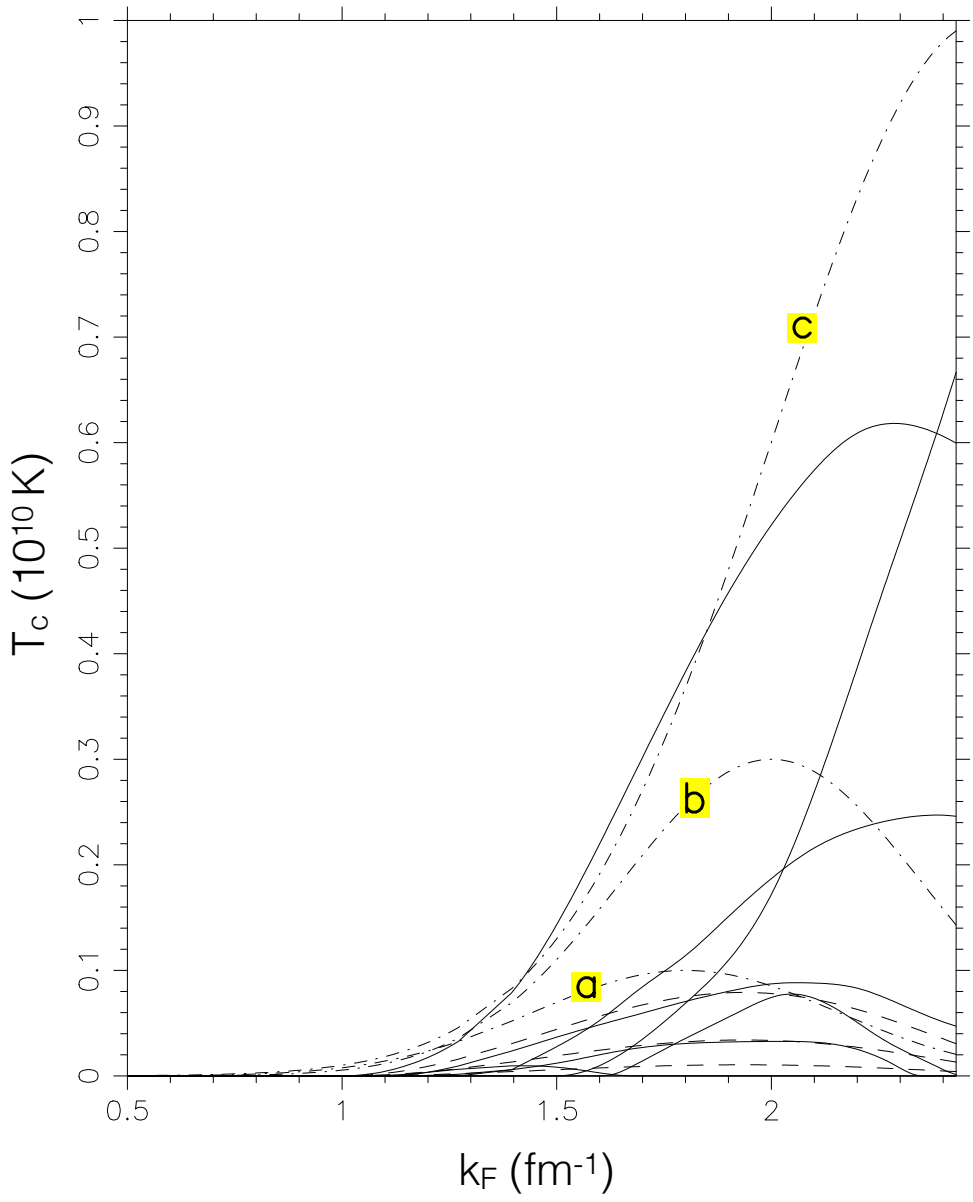

Figure 3.3 Neutron $^3P_2$ Pairing critical temperature, T_c, as a function of neutron Fermi momentum, $k_F(n)$ up to the central density of the model star considered here. The models [a], [b], and [c] are from [11]. The *solid line* models are from the following [from top]: [51], next two from [3], the following two from [99], [10], and last two from [25]

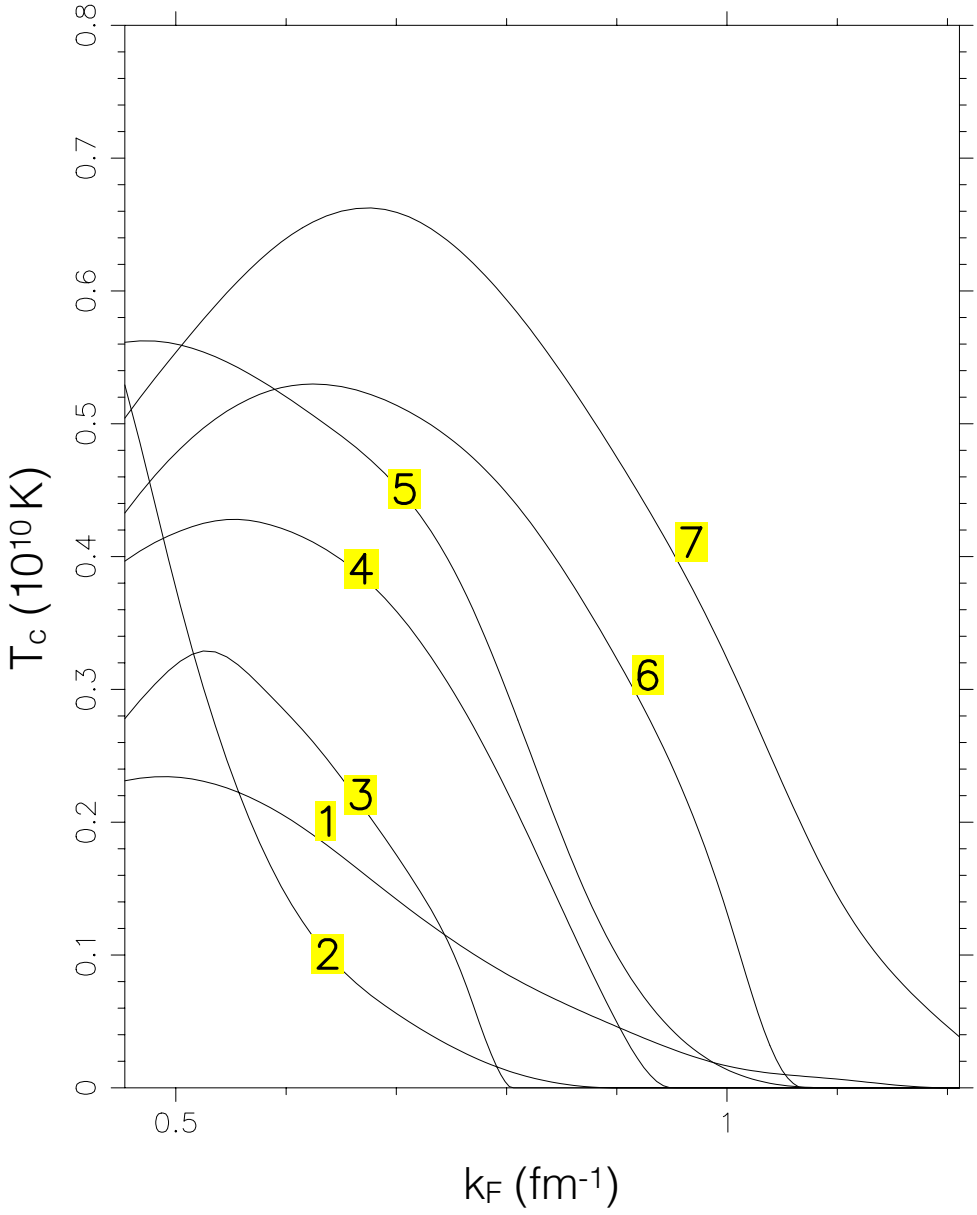

Figure 3.4 Proton $^1S_0$ Pairing critical temperature, T_c, as a function of proton Fermi momentum, $k_F(p)$ from the neutron drip point to the stellar centre. 1: [4], 2: [67], 3: [100], 4: & 6: [21], 5: [10], 7: [22]

(at constant volume) can be summed linearly,

$$C_v = \sum_i C_{v,i} \tag{3.28}$$

where i refers to the particular species such as leptons, baryons, mesons and quite possibly deconfined quarks. For degenerate matter, such as in the core, C_v is equal to C_p, the specific heat at constant pressure, and the Fermi liquid result (for unpaired matter) can be used,

$$C_{v,i} = N_i(0)\frac{\pi^2}{3}k_B^2 T = \frac{m_i^* p_{F,i}}{\pi^2\hbar^3}\frac{\pi^2}{3}k_B^2 T \tag{3.29}$$

As mentioned above, $N(0)$ is the density of states at the Fermi surface (see equation (3.26)). Figure 11 from [73] shows the relative contributions of various core constituents to C_v.

Temperatures well above T_c are associated with superfluidity and superconductivity and matter in the core is considered a normal Fermi liquid and energy states, $\varepsilon(p)$ from equation (3.21), above E_F are smoothly filled up, allowing for the above linearity in C_V. However, when T reaches T_c, the second order phase transition to a superfluid/superconductor occurs at the same time as pair breaking since $k_B T >> \Delta(T)$. The associated large fluctuations cause a sharp increase in C_V as more thermal energy becomes easily stored. As temperatures much below T_c are reached and matter in the core is in a superfluid and/or superconductive state, the gap in the energy spectrum decribed by equation (3.22) appears and the occupation probability is suppressed by a Boltzman factor $\sim exp[-2\Delta(T)/k_B T]$, thus strongly suppressing anything relying on thermally excited particles including C_v [73].

In the crust, C_v comes from degenerate free neutrons in the inner regions, from the nuclear lattice, and from the degenerate electron gas in the shallower layers. Since the inner crust neutron superfluid specific heat is strongly suppressed by the $^1S_0$ gap, the majority must come from vibrations of the lattice itself. The lattice forms at a temperature, T_g, and for T below this limit C_v doubles that of an ideal Maxwell-Boltzmann gas due to the lattice potential energy ($+1/2kT$). However, as T decreases past the Debye temperature, defined by $k_B\Theta_D \equiv \hbar\Omega_p$ where Ω_p is the ion plasma frequency, quantum effects become increasingly important thus we obtain [95],

$$C_v \simeq 3k_B, \quad \text{for } \Theta_D << T << T_g \tag{3.30}$$

$$C_v \simeq \frac{16\pi^4}{5}\left(\frac{T}{\Theta_D}\right)^3 k_B, \quad for\ T << \Theta_D. \tag{3.31}$$

Though the crust is physically much smaller than the core, its contribution is considered in detailed calculations, such as those performed in this project. In order to put the specific heat, with (or without) considering pairing effects, into practice one must use *control functions*, R: $C_v \rightarrow C_V^{Paired} = R_c C_V^{Normal}$. R functions for nucleon pairing in ${}^1S_0$ and ${}^3P_2$ channels have been calculated by Levenfish & Yakovlev [62]. Fig. 3.5 shows the contrast in C_v with depth in the star between the case where pairing is considered and that where it it is left out. Two different temperatures are considered to represent the early life of the star ($T = 10^8 K$) and it's later years ($T = 10^7 K$).

3.3.4. Neutrinos

Neutrino emission, from the crust as well as the core, is the dominant form of energy loss for a cooling neutron star until photon emission takes over at about 10^5 *years*.

Table 3.1 is merely a sample of possible neutrino emission processes, however it does include the main ones to be considered in this project. The second column decribes the process named in the first and the third column gives an order of magnitude estimate of the resulting emissivity, Q_ν. The R's in this column are control functions, such as those mentioned above in the context of the specific heat, to account for pairing effects such that $R = R(T/T_c)$. The final column refers to the efficiency of the process, whose presence or absense actually constrains the physical properties of the star.

The simplest neutrino emission mechanisms are the β-decay of the neutron and its inverse, otherwise known as the *Direct Urca* process for nucleons. For this reaction to occur, not only must energy be conserved but momentum as well. Since the matter in the neutron star core is degenerate, particles' energy and momenta are within $\sim k_B T$ of their Fermi energies and momenta. Furthermore, the Fermi energies, E_F are essentially equal to the chemical potentials, μ_i and energy conservation is given by the chemical equilibrium condition:

$$\mu_n = \mu_p + \mu_e \tag{3.32}$$

where μ_ν is neglected. Momentum conservation, on the other hand, is highly non-trivial and can be stated as the *triangle inequality*,

$$p_{F,n} \leq p_{F,p} + p_{F,e} \tag{3.33}$$

Charge neutrality would require that the number density $n_p = n_e$, which is related to the Fermi momentum by $n = p_F^3/3\pi^2\hbar^3$, thus requiring that $p_{F,p} = p_{F,e}$. The triangle inequality

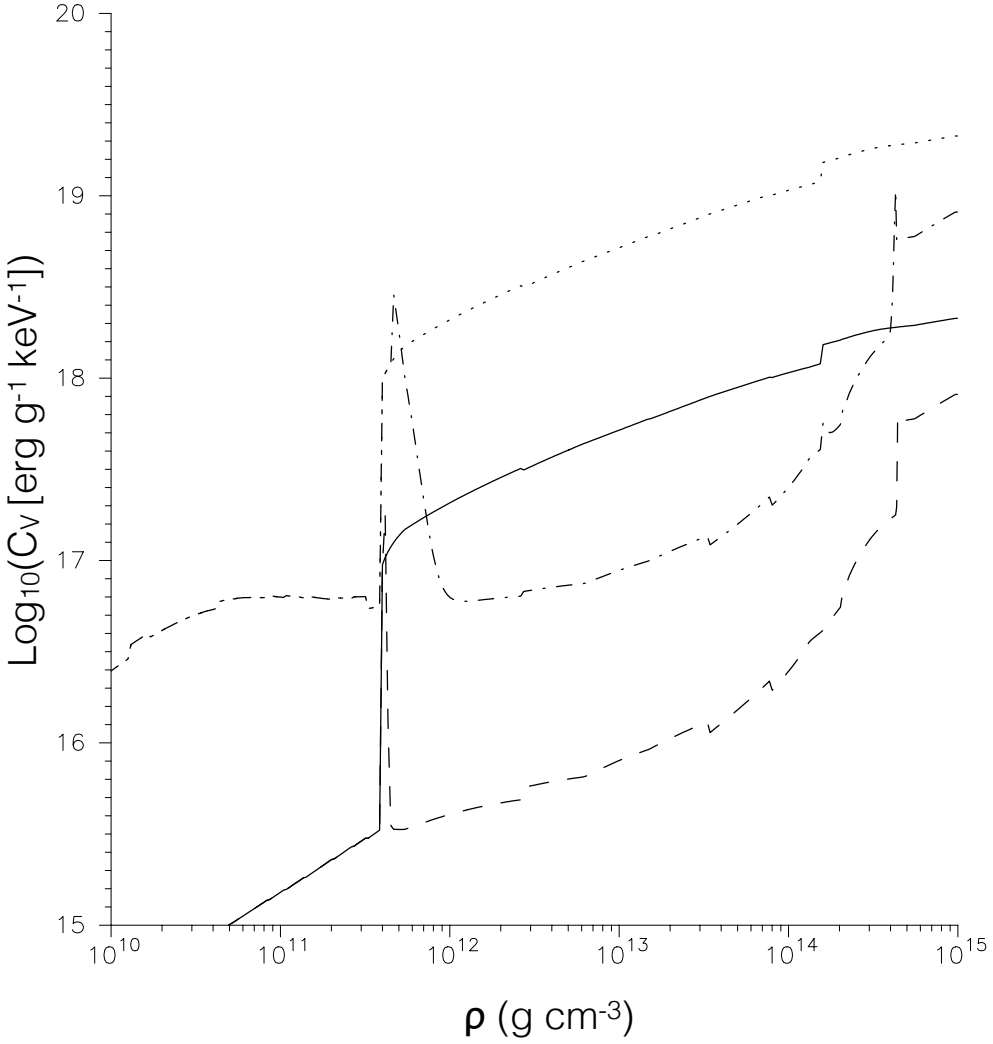

Figure 3.5 Specific Heat as a function of depth in the star for $T = 10^7 K$: *solid line*: no pairing, *dashed line*: pairing; and for $T = 10^8 K$: *dotted line*: no pairing, *dash-dot*: pairing. C_v is increasingly suppressed as $T << T_c$.

would then give $p_{F,n} \leq p_{F,p}$ which leads to $n_n \leq 8n_p$. Relating the proton fraction, $x_p \equiv n_p/n_B$ where n_B is the total baryon number density, the above gives $x_p \geq 1/9 \approx 11\%$ - a value higher than the estimated proton fraction of 5%, and suggesting from this simplistic case that the Direct Urca processes, and thus *fast* neutrino cooling, is out of reach. Hence the birth of the modified Urca (MUrca) processes.

MUrca processes have a spectator neutron, n', that satisfies the momentum conservation requirement, but since these processes now have five degenerate Fermions instead of only three, their emissivities become suppressed by approximately six orders of magnitude (this can be seen in comparing the emissivities of Table 3.1).

The reactions of other species of baryons can also be considered, depending on the input model star that one wants to study (see lower reactions of Table 3.1). Besides Urca processes there are also the Bremsstrahlung interactions through neutral currents (see middle of Table 3.1). They are the slowest processes considered here, by 2 orders of magnitude, but their contributions may not be all for naught when superfluidity comes in to play.

As with the specific heat discussed above, as T decreases below T_c, neutrino emmissivity is exponentially suppressed, their behavior characterized by control functions R [62]. This would seem bleak for cooling by neutrinos, except that when the phase transition to pairing first starts to take place the temperature in the star is still high enough that thermal agitation will break the pairs apart, thus releasing its binding energy in the form of neutrinos. This process is termed *Pair Breaking and Formation* or PBF and can potentially dominate neutron star cooling until T drops to aprroximately $0.2T_c$. Numerically, PBF also has it's control function. Although the reality of PBF has been around for many years ([28],[105]), it was not included in neutron star cooling calculations until [92] and [70].

Medium effects, mentioned above with respect to Cooper pair screening, have also been included in the MUrca process, modifying it to the Medium Modified Urca (MMUrca) which may be significantly more efficient than MUrca alone (though not so much so as the DUrca processes). The constraint on the DUrca processes was eventually shown to not be so strict [61] and can be included in recent cooling models.

It may seem that the core, comprising approximately 90% of the star, would be the dominant neutrino emitter, and general cooling agent. However, this is not necessarily the case. In the very early stages of a neutron stars life, the thermal diffusion time is less than its age and it's crustal temperature evolution is almost entirely independant of that in the core, thus entirely governing the evolution of the effective temperature. The dominant processes

Table 3.1. Sample of Neutrino Emission Processes [b]

Name	Process	Emissivity[a] ($erg\,cm^{-3}\,s^{-1}$)	
Modified Urca	$n+n \rightarrow n+p+e^- + \bar{\nu}_e$	$\sim 2 \cdot 10^{21} RT_9^8$	Slow
(neutron branch)	$n+p+e^- \rightarrow n+n+\nu_e$		
Modified Urca	$p+n \rightarrow p+p+e^- + \bar{\nu}_e$	$\sim 10^{21} RT_9^8$	Slow
(proton branch)	$p+p+e^- \rightarrow p+n+\nu_e$		
	$n+n \rightarrow n+n+\nu+\bar{\nu}$		
Bremsstrahlung	$n+p \rightarrow n+p+\nu+\bar{\nu}$	$\sim 10^{19} RT_9^8$	Slow
	$p+p \rightarrow p+p+\nu+\bar{\nu}$		
Cooper Pair	$n+n \rightarrow [nn]+\nu+\bar{\nu}$	$\sim 5 \cdot 10^{21} RT_9^7$	Medium
	$p+p \rightarrow [pp]+\nu+\bar{\nu}$	$\sim 5 \cdot 10^{19} RT_9^7$	
Direct Urca	$n \rightarrow p+e^- + \bar{\nu}_e$	$\sim 10^{27} RT_9^6$	Fast
(nucleons)	$p+e^- \rightarrow n+\nu_e$		
Direct Urca	$\Lambda \rightarrow p+e^- + \bar{\nu}_e$	$\sim 10^{27} RT_9^6$	Fast
(Λ hyperons)	$p+e^- \rightarrow \Lambda+\nu_e$		
Direct Urca	$\Sigma^- 1 \rightarrow n+e^- + \bar{\nu}_e$	$\sim 10^{27} RT_9^6$	Fast
(Σ^- hyperons)	$n+e^- \rightarrow \Sigma^- + \nu_e$		
π^- condensate	$n+ < \pi^- > \rightarrow n+e^- + \bar{\nu}_e$	$\sim 10^{26} RT_9^6$	Fast
K^- condensate	$n+ < K^- > \rightarrow n+e^- + \bar{\nu}_e$	$\sim 10^{25} RT_9^6$	Fast
Direct Urca	$d \rightarrow u+e^- + \bar{\nu}_e$	$\sim 10^{27} RT_9^6$	Fast
(u-d quarks)	$u+e^- \rightarrow d+\nu_e$		
Direct Urca	$s \rightarrow u+e^- + \bar{\nu}_e$	$\sim 10^{27} RT_9^6$	Fast
(u-s quarks)	$u+e^- \rightarrow s+\nu_e$		

[a] R's are the control functions used to include suppression from pairing. T_9 is temperature in units of $10^9 K$.

[b] Table data from [77].

for conditions of interest (i.e. neutron star temperatures) are plasmon, Γ, decay,

$$\Gamma \rightarrow \nu\bar{\nu}, \tag{3.34}$$

the electron-ion Bremsstrahlung process,

$$e^- + Nucleus \rightarrow e^- + Nucleus + \nu\bar{\nu}, \tag{3.35}$$

and pair annihilation,

$$e^- + e^+ \rightarrow \nu\bar{\nu} \tag{3.36}$$

the latter occurring at very high temperatures in order to allow for the presence of positrons.

The core neutrino control functions used in this work are from Levenfish & Yakovlev (1994) [62] whereas the crust neutrino calculations are from Itoh et al (1996) [53]. Fig. 3.6

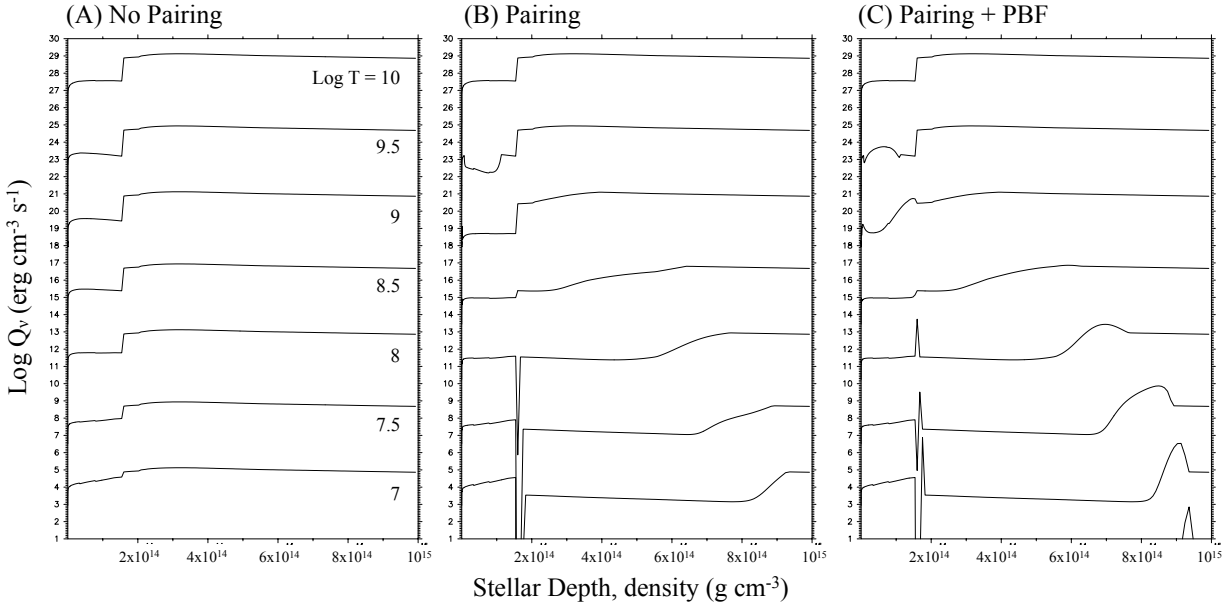

Figure 3.6 Neutrino emissivity, Q_ν, as a function of depth in the model star for a star of uniform temperature. Stellar depth has been displayed to emphasize the effects of pairing in the neutron star inner crust and core. (A) No pairing or PBF processing is considered; (B) The effect of pairing alone; and (C) The effect of pairing + PBF. As temperature decreases so does Q_ν.

shows the effect of pairing and PBF processes on neutrino emissivities for a range of temperatures representing the initial configuration of the model stars considered ($T = 10^{10}K$) to their later years ($T = 10^7K$). It can be immediately seen that in the early life of a neutron star, when core temperature is still very high, neutrino emmission plays the most important role in cooling. Fig. 3.6(A) shows neutrino emissivity with depth in the star for the case with no pairing considered. In the case of pairing alone, Fig. 3.6(B), as T drops below T_c neutrino emission is exponentially suppressed. In Fig. 3.6(C) when PBF processes are included, as T drops below T_c neutrino emission is still exponentially suppressed but is compensated for by neutrinos released in the PBF process when T is still high enough.

In order to establish evidence in favour of enhaced cooling, the *Minimal Cooling* paradigm was put forth by Page et al in [73] and [74] and excludes all "fast" neutrino emission mechanisms (see the DUrca processes of Table 3.1) while accounting for PBF. The idea behind

these models, which we have adopted in this project, is that certain theories of dense matter may be rejected if their restrictions do not meet observations. Conversely, if conditions are met then other theories of dense matter which do not embody them can then be rejected. (e.g. restrictions in the composition of certain combinations of light and heavy elements in envelope models or certain triplet gap sizes in the nucleus).

3.3.5. Conductivity

The next physical property to be considered in order to solve the Energy Balance equation of (3.14) are the agents for thermal conductivity κ. In the crust electrons dominate the thermal conductivity while in the core neutrons, in the case they are not superfluid, are the most efficient heat carriers. However, once paired, neutrons do not anymore contribute significantly and electrons are again the main agent of heat transport. In the crust, the principle considerations are electron interactions: e-phonons, e-ions and e-impurities. The lattice impurities are decribed by their concentration factor, Q. The crustal zone, whose composition is defined by the EOS adopted in this project and described in §3.2.2 and §3.2.3, is further divided from the crystal regime, where $\rho > \rho_{cryst}$ and e-phonons rule, to the liquid regime, $\rho > \rho_{liq}$ where e-ion interactions are more important. To avoid a discontinuity among the two regions, results from these interactions are interpolated. In the core, and in the presence of neutron superfluidity implying that electrons provide the major contribution to κ, electron-electron and electron-proton scattering are the processes controlling the thermal conductivity. The resulting conductivity is so high that the core is essentially isothermal, except possibly during the very early hase of evolution, at ages less then ~ 100 yrs. No data are available on such young neutron stars and discussing the effects of the core thermal conductivity is, at the present time, of purely academic interest. Three different model stars with calculations from different groups for each zone are contrasted in Fig. 3.7. *Model 1*: for $\rho > \rho_{cryst}$ e-phonon from [54] and e-impurity from [111], for $\rho < \rho_{liq}$ e-ion from [55]; *Model 2*: for $\rho > \rho_{cryst}$ e-phonon from [9] and e-impurity from [111], for $\rho < \rho_{liq}$ e-ion from [55]; *Model 3*: for $\rho > \rho_{cryst}$ e-phonon from [37] and e-impurity from [111], for $\rho < \rho_{liq}$ e-ion from [37]. Conductivity in the core in all models is taken from [96] for leptons and [8] for baryons.

Unless otherwise stated, *Model 2* from Fig. 3.7 conductivity calculations were used with the impurity fraction set arbitrarily to $Q_{imp} \approx 0.1$. The main reason this model was chosen

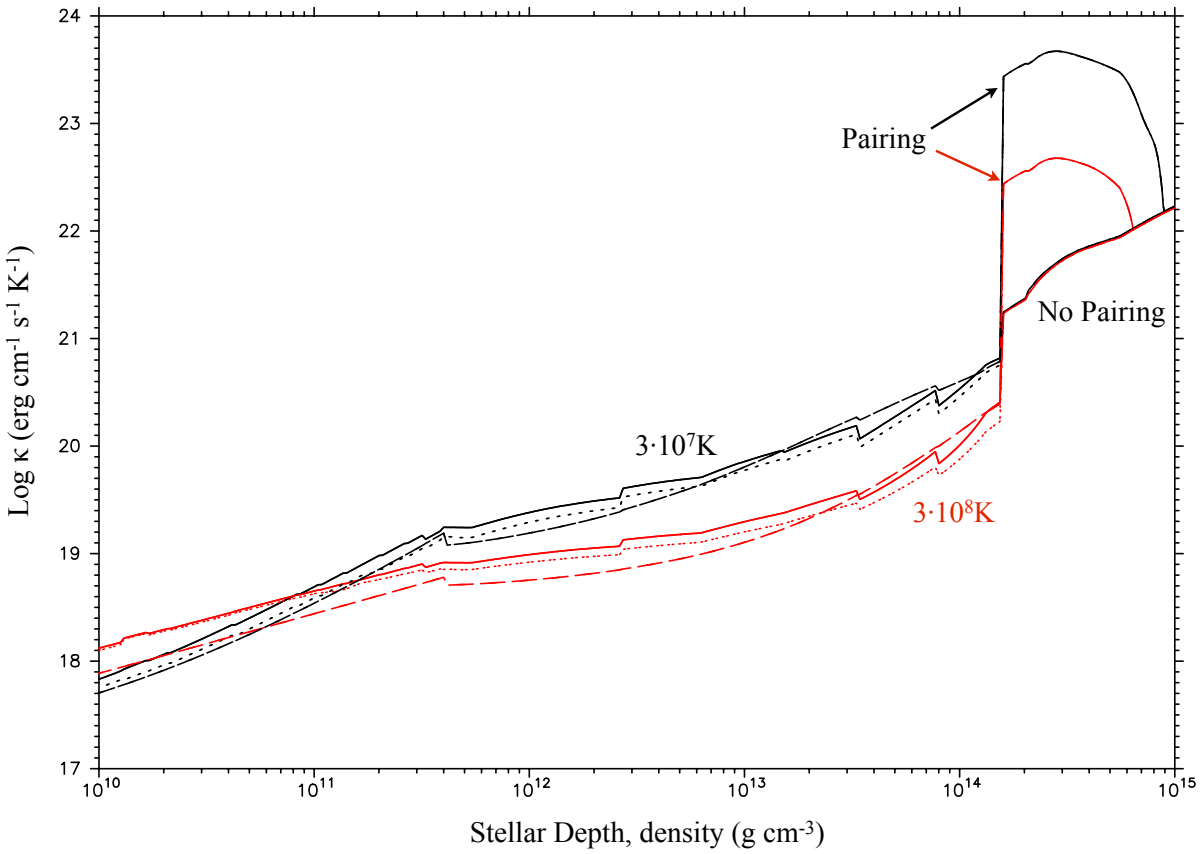

Figure 3.7 Conductivity , κ, with pairing and without as a function of stellar depth for three different models at $T = 3 \cdot 10^7 K$ (*black*) and $T = 3 \cdot 10^8 K$ (*red*) : [Model 1] *dotted line*: for $\rho > \rho_{cryst}$ e-phonon from [54] and e-impurity from [111], for $\rho < \rho_{liq}$ e-ion from [55]; [Model 2]*solid line*: for $\rho > \rho_{cryst}$ e-phonon from [9] and e-impurity from [111], for $\rho < \rho_{liq}$ e-ion from [55]; [Model 3] *dashed line*: for $\rho > \rho_{cryst}$ e-phonon from [37] and e-impurity from [111], for $\rho < \rho_{liq}$ e-ion from [37]. All models have core conductivity for leptons from [96] and for baryons from [8]. The impurity fraction set arbitrarily to $Q_{imp} \approx 0.1$.

over the calculations from *Model 3* is that for high temperature, as in the initial conditions for these model stars, the conductivity is very low near the surface and affects the ease of numerical calculation in that zone (see the dependence on conductivity κ in the Flux of the outer boundary condition).

3.3.6. Magnetic Field

One of the defining characteristics of neutron stars is their strong magnetic fields. Considering only the classical effect of Larmour rotation of electrons in a high magnetic field $> 10^{12} - 10^{13}G$, anisotropy of heat transport could extend throughout the entire crust, as in the case of a field with a strong meridian component confined entirely to the crust [32].

The expression for the thermal conductivity, κ, would become a tensor,

$$\kappa = \begin{pmatrix} \kappa_\perp & -\kappa_\wedge & 0 \\ \kappa_\wedge & \kappa_\perp & 0 \\ 0 & 0 & \kappa_\parallel \end{pmatrix} \tag{3.37}$$

with components,

$$\kappa_\parallel = \kappa_o \tag{3.38}$$

$$\kappa_\perp = \frac{\kappa_o}{1 + (\omega_B \tau)^2} \tag{3.39}$$

$$\kappa_\wedge = \frac{\kappa_o \omega_B \tau}{1 + (\omega_B \tau)^2} \tag{3.40}$$

where $\omega_B = eB/m_e^* c$ is the electron gyro-frequency and $1/\tau = \nu$ is the effective electron collisional frequency. $\omega_b \tau$ is referred to as the *Magnetization Parameter* and it's variation throughout the crust for a constant field of $10^{13}G$ can be seen in Figure 3.8 for several local temperatures. Particularly at lower temperatures $\omega_b \tau$ will have a strong effect on conductivity in the crust (see §4.4).

In the envelope of the neutron star, the low density $\rho < 10^{10} gcm^{-1}$ upper layer, classical and quantum magnetic field effects cause heat transport anisotropy which in turn reduces conductivity in the direction perpendicular to the field and enhances it parallel to the field (see above expressions for conductivity in equation (3.37)). Thus, the region around the magnetic poles is expected to be warmer than the region about the equator. The superfluid

core would remain isothermal and unaffected by the magnetic field. Greenstein & Hartke [43] showed that for fields $> 10^{10}G$ neutron star surface temperatures will not be uniform:

$$\begin{aligned} T_s(\theta,\phi)^4 &\equiv T_s(T_b;B,\Theta_B)^4 \\ &\approx \cos\Theta_B{}^2 \times T_s(T_b;B,\Theta_B=0)^4 \\ &\quad + \sin\Theta_b{}^2 \times T_s(T_b;B,\Theta_B=90)^4 \end{aligned} \tag{3.41}$$

where (θ,ϕ) are coordinates on the surface of the star and Θ_B is the angle between the magnetic field line and the normal to the surface. Potekhin et al [83] performed a more detailed calculation which eventually considered the neutrino emission in the outer crust [82]. Pons et al [80] further extended the former model by including ion/phonon heat transport in the envelope within their 2D model. Their magnetized envelope models build on the relationship presented in equation (3.41) in the following way:

$$T_s(B,\Theta_B,g_s,T_b) \approx T_s^{(0)}(g_s,T_b)\chi(B,\Theta_B,T_b) \tag{3.42}$$

where g_s is the surface gravity and χ is a function with terms transverse and logitudinal to the magnetic field lines that have been fitted to the model data:

$$\chi(B,\Theta_B,T_b) = \left[\chi_{\parallel}^{9/2}(B,T_b)\cos\Theta_B{}^2 + \chi_{\perp}^{9/2}(B,T_b)\sin\Theta_B{}^2\right]^{2/9} \tag{3.43}$$

Pons et al [80] give the following fits,

$$\chi_{\parallel}(B,T_b) = 1 + 0.05B_{12}^{0.25}T_{b,9}^{0.240} \tag{3.44}$$

$$\chi_{\perp}(B,T_b) = \frac{\sqrt{1+0.07B_{12}(0.03+T_{b,9})^{-0.559}}}{\left[1+0.9B_{12}/(0.03+T_{b,9})\right]^{0.4}} \tag{3.45}$$

and the results can be seen in Figure 3.10. Here, B_{12} is the magnitude of B in units of $10^{12}G$.

It has been shown ([63] and [17]) that a stable magnetic field configuration requires *poloidal + toroidal* components (see Figure 3.9). This toroidal component is maintained by poloidal currents in the crust. Geppert et al[33], and then later groups such as Pons et al [80], demonstrate that the effect of adding a strong toroidal component to the magnetic field entirely confined to the crust where it can be supported, is to strongly suppress radial heat flow in the regions where is it strongest. Thus, the magnetic poles are expected to equalize their temperature with the stellar core, but the blanketing effect of the toroidal field will maintain a cooler equatorial region.

Besides the large dipolar component, the exact structure of the magnetic field, which should evolve along with the star, is still uncertain and it is a goal of neutron star cooling models to test the viability of magnetic structure models.

3.3.7. Outer Envelope and Atmosphere

As mentioned above, the outer layers of a neutron star consist of low-density, not fully-degenerate matter on the scale of $\sim 10m - 100m$ possibly covered by an atmosphere on the scale of centimeters. These layers can be comprised of light elements (H and He), mixed heavy elements or rather a condensed solid surface if highly magnetized. This thin envelope is all that stands in the way between the hot neutron star interior and the emitted flux, $F(E)$, that we observe from Earth. The Photon Luminosity (Equation(3.16)) actually gives the definition of the Effective Temperature, T_e. As mentioned in §3.3.1, the $T_b - T_e$ relation relates the temperature at the outer boundary of the star to the effective temperature, which should be measurable (see Equations (3.17) to (3.19)).

The thermal relaxation timescale in the envelope is less than that of the core so it can be treated separately in cooling calculations as a layer always in a steady state. With this assumption, plus a plane-parallel approximation due to its thiness, solving the heat transport (3.13) and hydrostatic equilibrium (3.4) equations gives a relationship between the temperature at the bottom of the envelope, T_b, and the Flux, F, going through it (or equivalently with the effective temperature T_e, hence the $T_b - T_e$ *relationship*). The results of Gudmundsson et al (1982)[44] for neutron star envelopes are summarized by the following, simple $T_b - T_e$ relation,

$$T_e \simeq 0.87 \times 10^6 g_{s14}^{1/4} \left(\frac{T_b}{10^8 K} \right)^{0.55} \tag{3.46}$$

where g_{s14} is the surface gravity acceleration in units of $10^{14} cm\ s^{-2}$ and the composition assumed to be that of ^{56}Fe and Fe-like nuclei). This relation shows the dependence of T_e on g_{s14} only, which contains M and R, thus liberating it from dependence on $M(r)$. This allows one the ability to take an envelope model and effectively stick it on as the outer layer in a stellar model. Although equation (3.46) is based on *catalyzed matter*, real neutron star envelopes are likely more complicated in composition (e.g. He, He, C, O from the progenetor supernova) and there are many models out there exploring this (see Figure 3.10).

In the absence of thermal gradation effects such as strong magnetic field configuration or additional heating from processes like accretion, the stellar interior will become isothermal

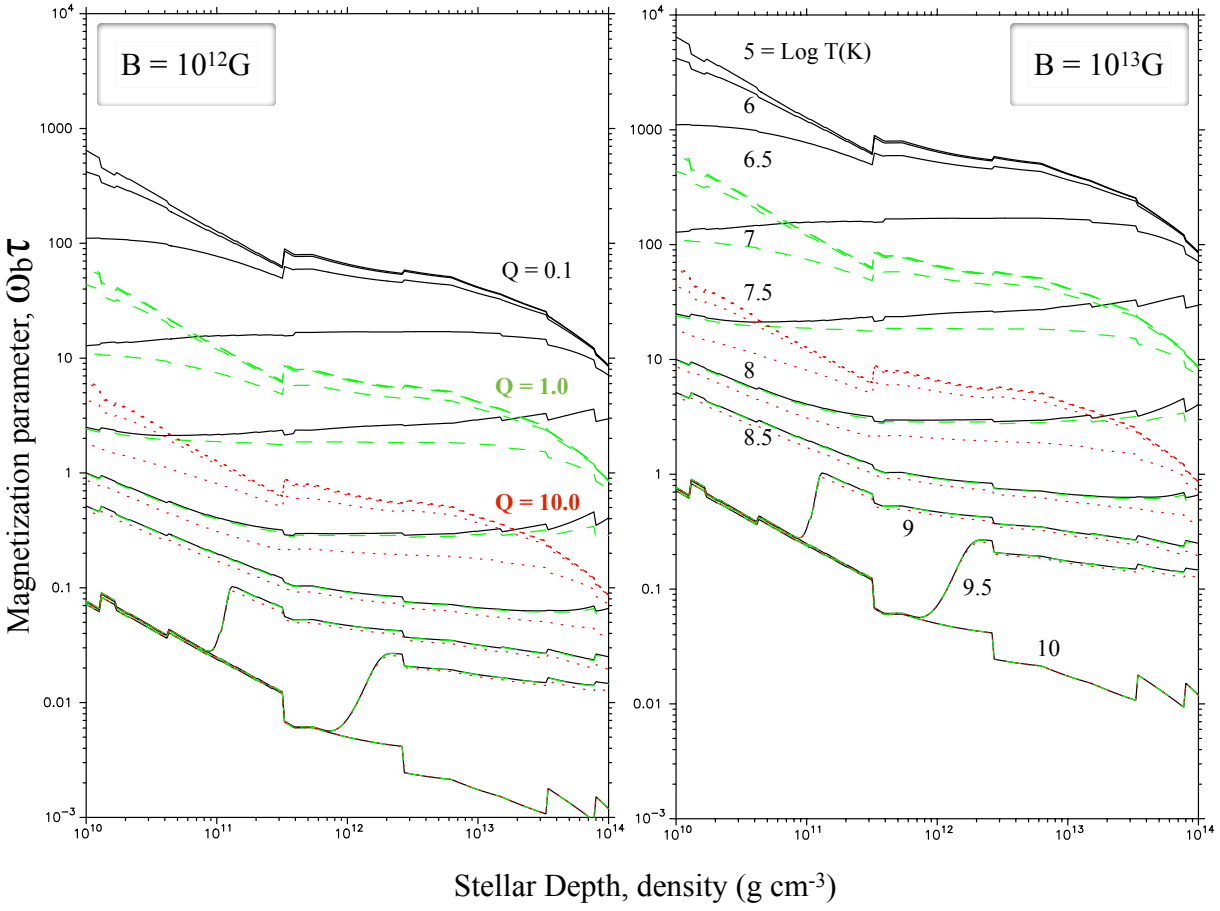

Figure 3.8 Magnetization Parameter $\omega_b\tau$ for a uniform field of $B = 10^{12}G$ (*left*) and $B = 10^{13}G$ (*right*) in a crust with impurity concentrations of $Q = 0.1$ (*black*), $Q = 1.0$ (*green*) and $Q = 10.0$ (*red*) . Various temperatures are presented starting with $T = 10^5K$ at the top and finally $10^{10}K$ at the bottom.

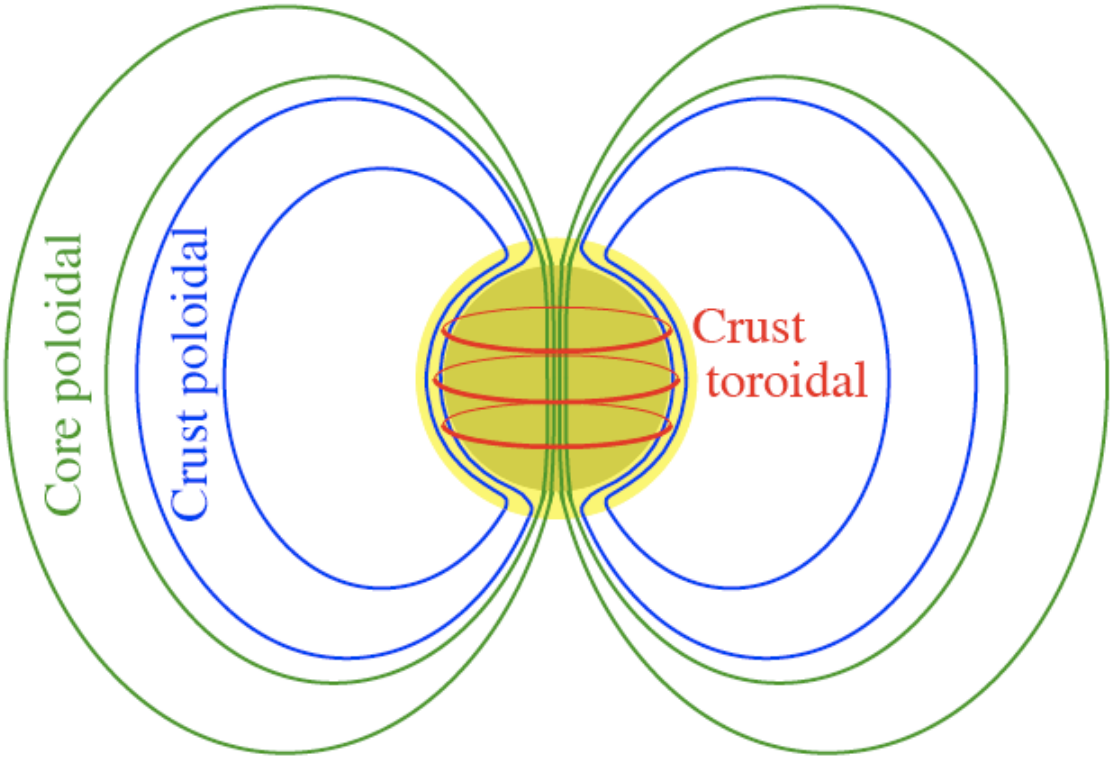

Figure 3.9 Schematic of magnetic field lines for a neutron star with a core-centered dipolar field plus a crustal poloidal + toroidal field (Artist: Dr. Dany Page)

by an age of ~ 100 *years*. This is due to the dominance of degenerate electrons as heat carriers. Photons are the main carriers in the lowest density layers until the density increases such that electrons are not yet fully degenerate (i.e. bottom of the layer, liquid). This zone is termed the *Sensitivity Strip* and acts to regulate the heat escaping from the interior. Thermal conductivity in this zone is proportional to Z^{-1}, therefore light elements penetrating this layer increase its ability to transport energy and thus higher T_e can be acheived. Conversely, higher T_e also means electron degeneracy starts deeper in the star, and a thicker layer of light elements would be needed to affect outgoing temperature [71].

Given the importance of the *sensitivity strip* to heat gradation, the compositon of the outermost layers of the atmosphere is not so important for the outgoing flux, F, but will determine the spectral distribution, $F(E)$. Observed spectra can then be fitted with model atmospheres in order to estimate T and R: light element models generally give lower T and larger angular size (sometimes too large); and heavy element models give higher T but sometimes too small R. Figure 3.10 shows some models including the Fe envelope considered by [44] (*sold line*) and a lighter envelope model by [81] (*dashed line*). The results of Potekhin et al [81] (*dash-dot*) are used for models that do not consider magnetic field effects, and those of Pons et al [80] (*dash-dot-dot*) are used for those stars with magnetic envelopes.

3.4. Observations

3.4.1. Pulsars and Magnetic Braking

Immediately after their creation, conservation of angular momentum causes neutron stars to rotate extremely rapidly (on the scale of ms) and they are also thought to be born with high magnetic fields ($> 10^{10}G$). Coupling of the rotating magnetic field with the external environment ("magneto-dipolar radiation") and particle ejection from the magnetosphere ("pulsar wind") produces a torque that continuously slows down the rotation. Assuming a dipolar field, the magnitude of the magnetic field at the equatorial surface of a neutron star can be inferred using the observational parameters of period, P, and spin-down period, $\dot{P}$

The most abundant type of neutron star studied to date is the radio pulsar, whose pulsed emission in radio and x-rays is generally considered as regular as clockwork. They are thought to be powered by rotational kinetic energy loss from magnetic braking, which also provides a convenient method for estimating dipolar magnetic field strength, B, from

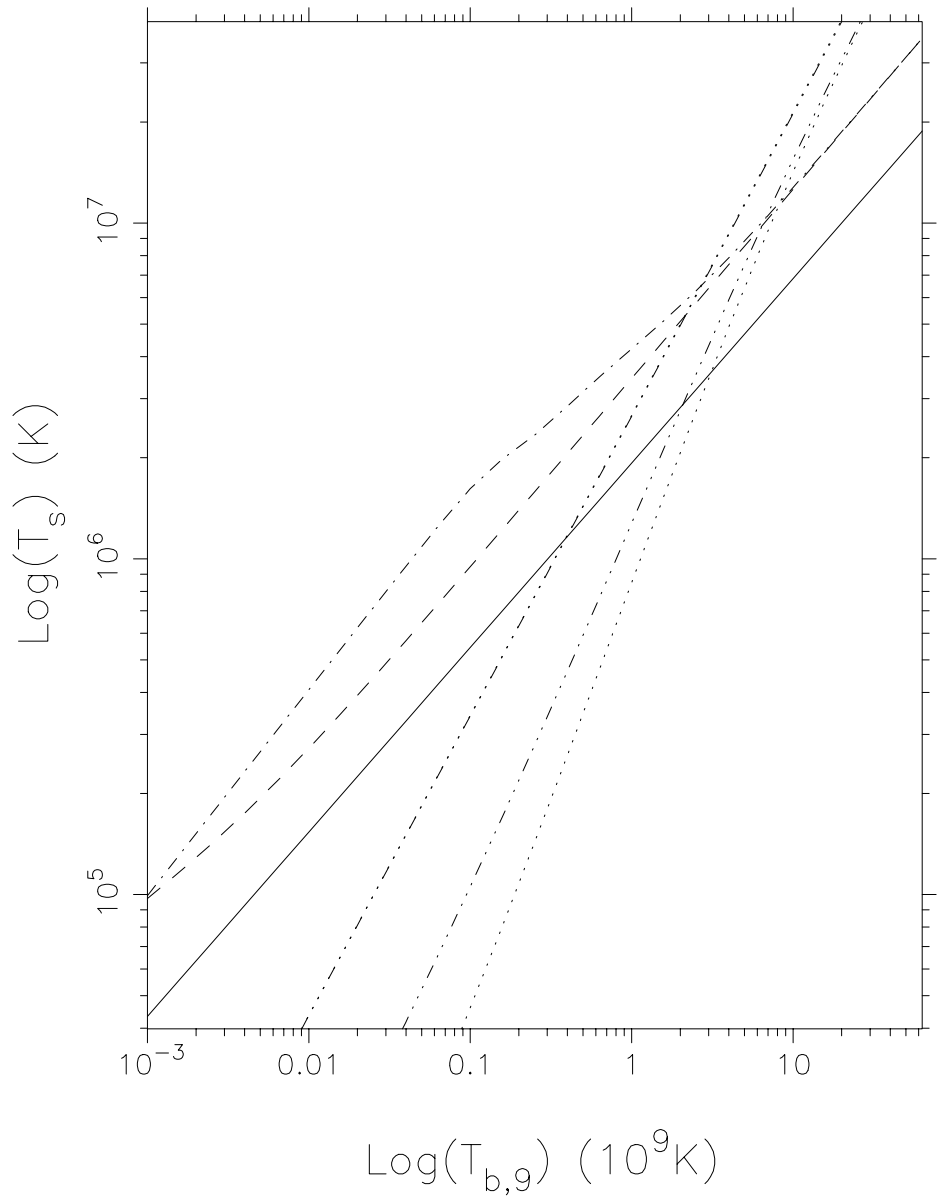

Figure 3.10 Envelope Models showing the relationship bewteen the surface temperature, T_s, and the temperature at the bottom of the envelope, T_b. The *solid* line shows the results of [44] for an Fe based envelope (see equation (3.46)), the *dashed* line includes light elements from [81], the *dash-dot* line is an unmagnetized model from [81] where as the *dotted* lines show the same model with $B = 10^{13}G$, finally the *dash-dot-dot* lines show a variation on the previous model done by [80]. For the magnetized models, the upper curves show T_s at the magnetic poles and the lower curves T_s at the equator.

their spin characteristics, $P - \dot{P}$.

The following Magnetic Dipole Model shows how pulsar emission can be derived from the kinetic energy of a rotating neutron star independant of the interior field geometry. A time-varying purely dipole moment, $\mathbf{m}$, as seen by an observer at infinity will have the following luminosity [95],

$$L = \dot{E} = -\frac{2}{3c^3}|\ddot{\mathbf{m}}|^2 \tag{3.47}$$

If the dipole moment is written:

$$m = \frac{1}{2}B_p R_{NS}^3(e_\parallel \cos\alpha + e_\perp \sin\alpha \cos\Omega t + e'_\perp \sin\alpha \sin\Omega t) \tag{3.48}$$

then the luminosity is:

$$L = \frac{-B_p^2 R_{NS}^6 \Omega^4 \sin\alpha^2}{6c^3} \tag{3.49}$$

where α is the angle between the angle of orientation between $\mathbf{m}$ and the rotation axis, and $\Omega = 1/P$ is the frequency of rotation. In terms of the rotational kinetic energy of the star,

$$E = \frac{1}{2}I\Omega^2 \tag{3.50}$$

$$\dot{E} = I\Omega\dot{\Omega} \tag{3.51}$$

Thus,

$$B_p^2\Omega^4 \propto \Omega\dot{\Omega} \tag{3.52}$$

which, after substitution of the relation $P = 1/\Omega$ and $\dot{P} = -\dot{\Omega}/\Omega^2$, gives the useful relation:

$$B_p \simeq \sqrt{\frac{c^3 I|\dot{\Omega}|}{\Omega^3 R^6}} \simeq 3.2 \times 10^{12}(P_s \dot{P}_{14})^{1/2}\ \mathrm{G} \tag{3.53}$$

where P_s is P measured in seconds and $\dot{P}_{14}$ is $\dot{P}$ is measured in 10^{-14} s s^{-1}. This is of course only a coarse estimate of the surface magnetic strength and, within the approximations involved in the model, the numerical coefficient also depends on the assumed values of I and R. The braking index, n, is given by $\dot{\Omega} \propto \Omega^n$. For the Magnetic Dipole Model $n = 3$. As a matter of interest, in the case of gravitational wave emission $n = 5$.

Fields from $10^8 G$ for millisecond Pulsars to $10^{15} G$ for Magnetars have been estimated from the $P - \dot{P}$ relation (see Figure 3.11) and used to diversify neutron stars into various, perhaps not wholly unrelated, classes that will be discussed in the next section *Observations*.

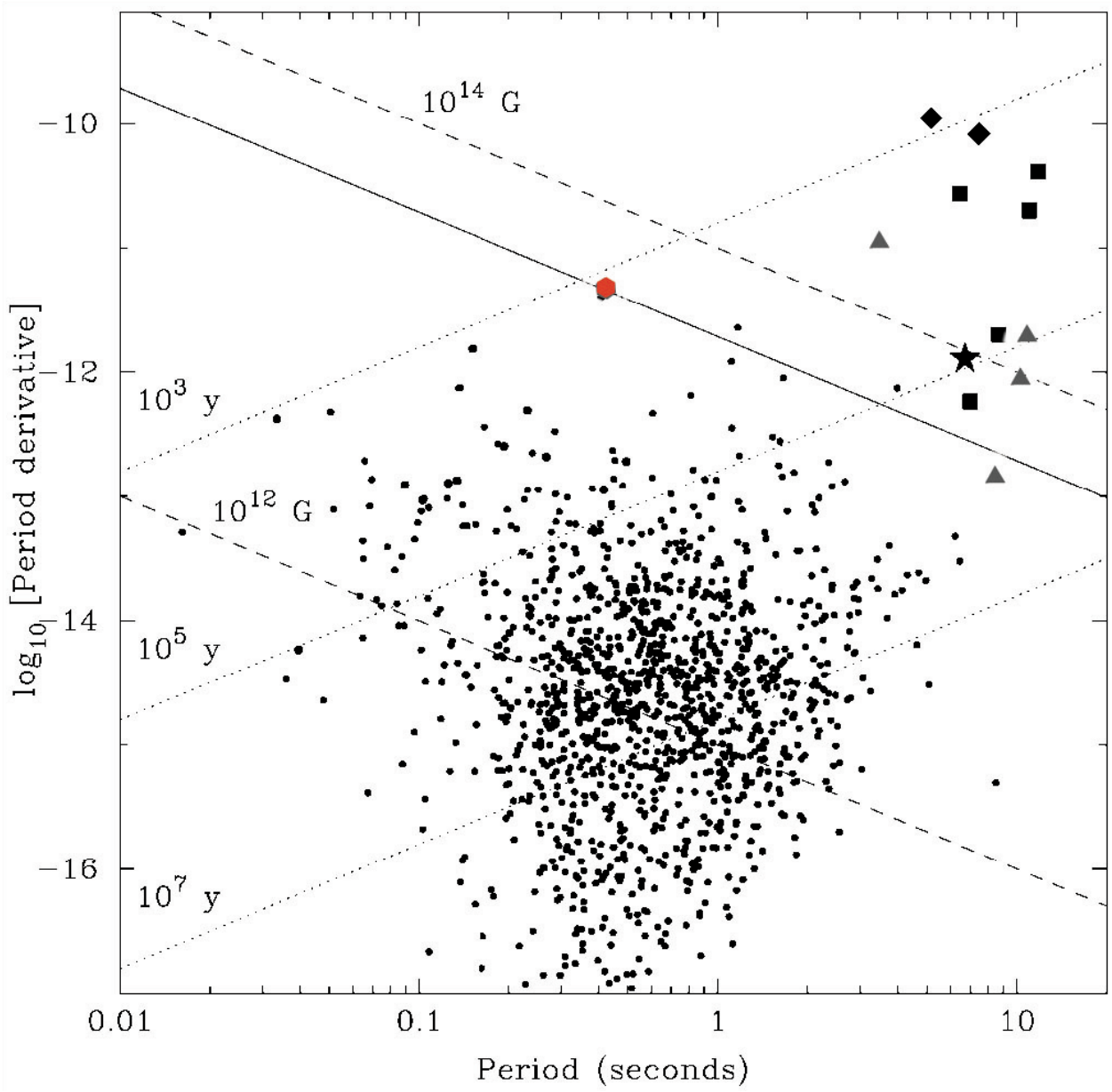

Figure 3.11 $P - \dot{P}$ diagram from McLaughlin et al. 2003 [65]. *dots*: represent radio pulsars, *diamonds* SGR's, *squares*: AXPs, *star* HBPSR J1847-0130 presented in the paper, *triangles*: XDINS presented in [45], *hexagon*: HBPRS J1119-6127 presented in [41]. *Dashed lines* show lines of constant inferred dipolar magnetic field strength (at the equator, i.e., $B_p/2$) and *doted lines* show constant characteristic ages. The *solid line* represents the Quantum Critical Field B_{CR}. As can be noted from the diagram, classes of magnetized neutron stars discussed in this project fall nearly in the same region suggesting a relation between them.

3.4.2. The Zoo

HBPSRs - High Magnetic Field Pulsars

Radio pulsars are by far the most commonly studied neutron stars. The first pulsar was discovered in 1967 by Jocelyn Bell and Anthony Hewish [49] and the extremely regular radio pulses were first thought to be a signal from extraterrestrials, which was later correctly interpreted as pulsar emission. Their power is generally thought to be due to the loss of rotational kinetic energy through magnetic dipole braking. The exact mechanism that converts rotational energy into the observed pulses is poorly understood, despite the consistancy of observations among sources. Pair production along the magnetic dipole axis is thought to produce radio emission which is then beamed within a radius dependant on the period of rotation of the star.

Previously, radio pulsars were divided from Magnetars by the Quantum Critical field, $B_{CR} \sim 4.4 \cdot 10^{13} G$. at which cyclotron energy equals the electron rest-mass energy. In fields above B_{CR} magnetic photon splitting overrides pair production and no radio emisiion is produced. Before the Parkes Multibeam Survey (1999) the largest magnetic dipole field inferred for a radio pulsar was $2.1 \cdot 10^{13} G$ and the aforementioned division held. However, with Parkes, radio pulsars with dipole fields above this limit have been discovered. PSR J1847-0130, shown as a *star* in Figure 3.11, was reported by McLaughlin et al (2003) to have a $B \sim 9.4 \cdot 10^{13} G$ which puts it in the same range as the Magnetars, specifically the AXPs. An upper limit on its x-ray luminosity shows it is a weaker emitter in x-rays than AXPs, however the similar B field strength suggests that the x-ray luminosities of some AXPs must be due to something other than just their strong dipolar magnetic fields. A natural candidate is the presence of multipolar, and also toroidal, components that would be much stronger in magnetars than in radio pulsars.

XDINs - X-Ray Dim Isolated Neutron Stars

There is a group of neutron stars, once dubbed *the Magnificent Seven* (their number has grown by now to eight [90], and the new member has been dubbed "Calvera" !) , all showing similar characteristics that distinguish them from other neutron stars. As their title sugests, they have low but persistent emission in x-rays ($L_x \sim 10^{30} - 10^{31}$ ergs s^{-1}) and no apparent emission in radio. Their x-ray spectra are best fit with a black body of temperature $kT \sim 40 - 110$ eV and some show one or a few broad absorption line(s). They

Table 3.2. Sample of High Magnetic Field Radio Pulsars

PSR	J1847-0130	J1718-3718	J1814-1744	J1846-0258	J1119-6127	J1357-6429[a]
B $(10^{13}G)$	9.4	7.4	5.5	4.8	4.1	0.8
$\dot{E}$ $(erg\ s^{-1})$	$1.7 \cdot 10^{32}$	$1.5 \cdot 10^{33}$	$4.7 \cdot 10^{32}$	$8.0 \cdot 10^{36}$	$2.3 \cdot 10^{36}$	$3.1 \cdot 10^{36}$
L_x $(erg\ s^{-1})$	$< 5 \cdot 10^{33}$	$\sim 10^{30}$	$< 6 \cdot 10^{35}$	$6.4 \cdot 10^{34}$	$2.0 \cdot 10^{33}$	$3.7 \cdot 10^{32} d_{2.5}^2$
$P(s)$	6.7	3.4	4.0	0.32	0.408	0.166
τ_c (kyr)	83	34	85	0.72	1.7	7.3
d (kpc)	~ 8	$4 - 5$	~ 10	~ 19	8.4	~ 2.5
PWN?	-	-	-	yes	yes	yes
PF (%)	-	-	-	-	74 ± 14	63 ± 15
Reference	McLaughlin et al. (2003) [65]	Kaspi & McLaughlin (2005) [59]	Pivovaroff et al. (2000) [79]	Helfand et al. (2003) [48]	Gonzalez et al. (2005) [41]	Zavlin (2007) [112]

[a]Aun que PSR J1357-6429 no califica como un HBPSR, esta incluido por comparason en la Tabla por su emision rayos-x y PF similar a PSR J1119-6127.

have an optical component in their spectra best fit with the low-energy tail of a black body of slightly lower temperature than the x-ray black body with an emitting radius much larger that the emitting radius of the warmer component ($\sim 3-5$ km). The assumed radius of a neutron star is between $10-15$ km, a range that lies between the radii indicated by the two thermal components of the spectrum. This shows that XDINs may have some sort of surface temperature anisotropy. In five sources, pulses in the light curve are observed with pulse fractions between 4% and 18%. Inferred dipole magnetic fields range between 10^{13} G and 10^{14} G for two of the XDINs. Fields in the same range were also inferred for 5 of the XDINs from interpretation of the broad absorption line as resulting from proton-cyclotron absorption.

It is thought that these are young, close-by cooling neutron stars between 10^5 and 10^6 years old which is consistent with the low observed column density ($N_H \sim 10^{-2}$ which implies $d \sim 10-100$ pc), the lack of association with a SN remenant (age $> 10^5$ yrs) and the thermal x-ray emission (age $< 10^6$ yrs) [45]. These neutron stars have been the specific study of the effects of the magnetic field on neutron stellar properties (e.g. surface temperature distributions) to explain observations such as light curves and x-ray spectra.

SGRs - Soft Gamma-Ray Repeaters

The trademark of SGRs is the repetition of short (~ 100 ms) soft gamma-ray and x-ray bursts with energies of $\sim 10^{41}$ ergs and risetimes of ~ 10 ms. There are 4-6 known SGRs located in the Galactic Plane and one in the LMC. Their burst spectra are well modelled by optically thin thermal Bremsstrahlung emission with $kT \sim 20-50$ eV. Burst activity is highly episodic with the occasional giant gamma-ray burst of energy $> 4 \cdot 10^{44}$ ergs. Three sources show pulse periods in x-rays during quiescence, two of which with inferred magnetic field of $\sim 10^{15}$ G. The spectra in quiescence are well modelled by a power-law with photon index of $2-3$. The pulses have broad profiles and resist coherent timing over spans longer than a few weeks (i.e. *noisy rotators*). The bursting and rotational behavior seem uncorrelated.

There are many factors that support the idea that SGRs are a manifestation of magnetars. In 1979, SGR 0525-66 was detected coming from the direction of a supernova remnant SNR. An 8 s periodicity modulated the decaying light curve of the burst, which had a luminosity > 6 Eddington Luminosities. In order to slow down a neutron star from a $P \sim 10$ ms at birth to a $P = 8$ s in $\sim 10^4$ years, the approximate lifetime of a SNR, a very high magnetic field is

needed. This argument predicted $\dot{P}$ for two more SGRs. Considering energy requirements to produce burst luminosities, rotation only gives a maximum of 10^{33} ergs and accretion is ruled out by the absence of a companion and the fact that such behavior has never been seen in an accreting system. A magnetic field $> 10^{15}$ G is needed for the energy of a giant burst to be a small fraction of available magnetic energy. As well, magnetar strength fields are required to confine hyper-Eddington burst to ~ 100 ms. Furthermore, they lower the Thompson cross-section thus reducing scattering opacity to allow these higher fluxes to escape. Fields $< 10^{14}$ G are not expected to decay rapidly whereas fields $> 10^{14}$ G decay via ambipolar diffusion in the core and Hall drift in the crust on timescales of about 10^4 years . It is thought that the quiescent x-rays originate from the surface by internal heating of the decaying magnetic field whereas bursts could result from the crust cracking under magnetic stress [58].

AXPs - Anomalous X-Ray Pulsars

AXPs are very similar to SGRs with some differences. Their behavior is typified by x-ray pulsations of $L_x \sim 10^{33} - 10^{35}$ ergs s^{-}1 and $P \sim 6 - 12$ s. Their x-ray spectra are relatively soft compared to most accreting x-ray pulsars and are best described by two components: a black body with $kT \sim 0.4$ keV; and a hard power-law with photon index $2.5 - 4$. Like SGRs they show broad pulse profiles and similar $P - \dot{P}$ characteristics in quiescent x-ray spectra. However, they are less *noisy rotators* with softer spectra, lower inferred B and more frequent association with a SNR. In two cases SGR-like burst were detected, however AXP bursts have a wider range of durations and show a correlation with rotation as they occur preferentially near pulse maxima. These bursts indicate a major event extended in time with one component from surface fracture(s) and the other more broadly distributed, as with magnetars. AXPs were initially dubbed *anaomalous* as they were thought to be similar to the x-ray pulsars found in high mass x-ray binaries, long pulse period and strong magnetic field, but no companions were found. For similar arguments as those presented above, it is likely that AXPs have magnetar-like fields. The absence of a companion is supported by the lack of Doppler shift in the pulses and the low characteristic age is supported by associations with SNR. In the case of 1E 2259+586, a glitch, the temporary spin-up of the period, suggests a possible disturbance in the superfluid core. Extended flux enhancement and pulse profile change suggests an excitation of magnetospheric currents plus crustal heating [58].

3.4.3. More Questions than Answers

The last decades has seen a great advancement in the quantity and quality of observations of the myriad of neutron stars and their related phenomena. Despite this, these objects still retain many of their secrets. It is still a mystery whether or not the phenomenon of the magnetars, pictures in the upper right quadrant of Fig. 3.11 are related or not.

Fig. 3.12 shows where some of these neutron stars lie in relation to a cooling curve (the model curve comes from a numerical simulation of a non-magnetized neutron star without the effects of superfluidity from §4.3 in the following chapter). It can immediately be seen that some stars lie very close to the model cuvre, whereas several more are grouped well above it: these are the magnetars and one of the challenges of modelling temperature diffusion inside magnetized neutron stars is to reach these relatively high effective temperatures for a mature star. At the moment, we can strive for these magnetar temperatures assuming a persistent heating source in the crust of the star (see §5.1).

The following chapter is dedicated to the calculations performed in this work to solve the Energy Balance Equation (3.10) and track the effective temperature, T_{eff}, of our model stars over time.

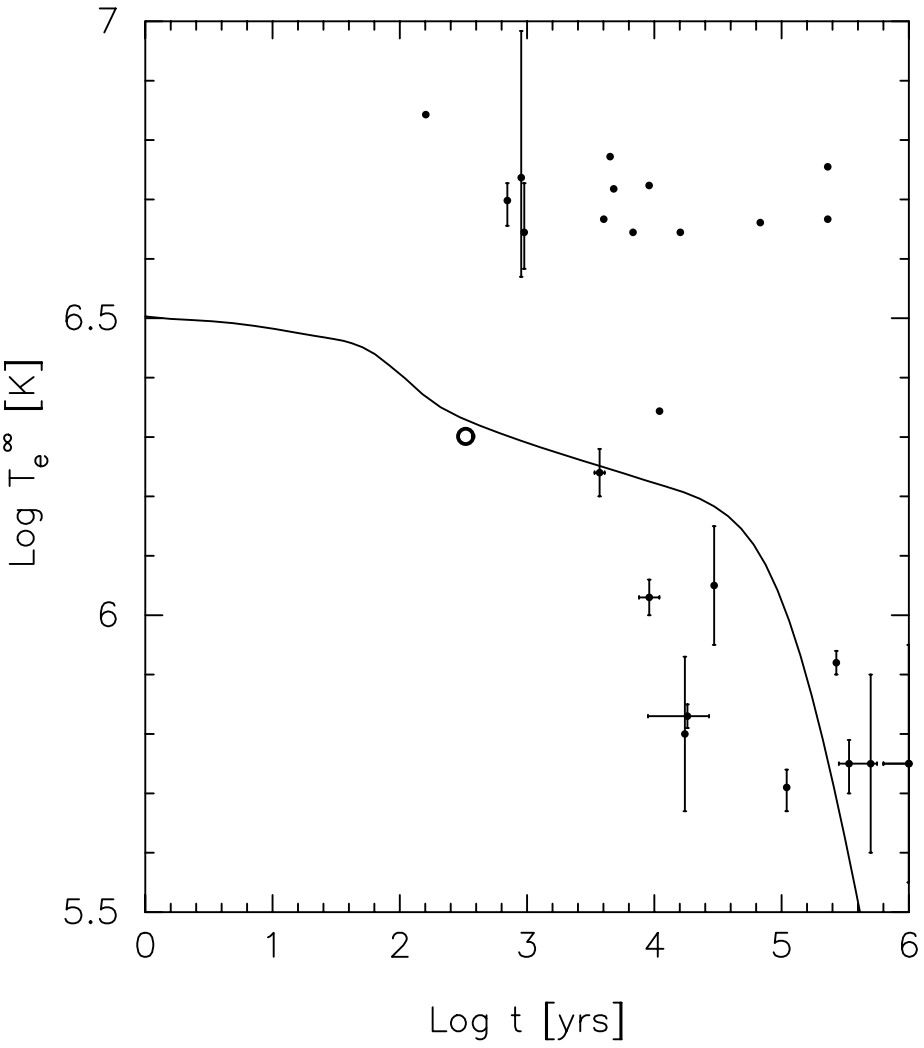

Figure 3.12 Observed neutron star effective temperatures on a cooling curve. The solid line are the results from the simulated cooling of a non-magnetized neutron star without the effects of superfluidity described in §4.3. The data can be found in the Tables 3.3 and 3.4.

Table 3.3. Sample Magnetar Data

Name	P (s)	dP/dt $(10^{-11}s/s)$	$B_{surf})$ $(10^{14}G)$	dE/dt $(10^{33}erg/s)$	τ_c (kyr)	N_H $(10^{22}cm^{-2})$	T_{BB} (keV)	d (kpc)	L_x $(10^{35}erg/s)$
4U 0142+61[a]	8.68832877(2)	0.20332(7)	1.3	0.12	68	0.96(2)	0.395(5)	3.6(4)	1.1
1E 1048.1-5937[a]	6.457875(3)	2.25	3.9	3.3	4.5	0.97(1)	0.51(1)	2.7(1)	0.059
1E 2259+586 [a]	6.9789484460(39)	0.048430(8)	0.59	0.056	230	1.012(7)	0.400(7)	4.0(8)	0.34
1E 1841-045 [a]	11.7828977(10)	3.93(1)	6.9	0.95	4.8	2.2(1)	0.45(3)	$8.5^{+1.3}_{-1}$	1.9
1E 1547.0-5408 [a]	2.0721255(1)	4.7	3.2	210	0.70	$3.1^{+0.7}_{-0.8}$	$0.43^{+0.03}_{-0.04}$	3.9(1)	0.0058
1RXS J170849.0-400910 [a]	11.003027(1)	1.91(4)	4.6	0.57	9.1	1.48(4)	0.456(9)	3.8(5)	0.59
XTE J1810-197 [a]	5.5403537(2)	0.777(3)	2.1	1.8	11	0.63(5)	0.19(3)	3.5(5)	0.00031
CXOU J010043.1-721134 [a]	8.020392(9)	1.88(8)	3.9	1.4	6.8	0.3(4)	0.38(2)	60	0.61
CXO J164710.2-455216 [a]	10.6106563(1)	0.073	0.89	0.024	230	1.9	0.49(1)	5	0.0044
CXOU J171405.7-381031 [a]	3.82535(5)	6.40(14)	5.0	45	0.95	$4.11^{+0.82}_{-0.34}$	$0.38^{+0.08}_{-0.05}$	8	0.22
PSR J1622-4950 [a]	4.3261(1)	1.7(1)	2.7	8.3	4.0	2	0.4	9	0.0063

[a]Data collected from the McGill SGR/AXP Online [64]

Table 3.4. Sample Neutron Star Data

Name	t_{sd}[a] ($log_{10} yrs$)	t_{kin}[b] ($log_{10} yrs$)	T_∞) ($log_{10} K$))	d (kpc))	L_∞ ($log_{10} ers\, s^{-1}$)
RX J0822-4247	3.90	$3.57^{+0.04}_{0.04}$	$6.24^{+0.04}_{-0.04}$	1.9-2.5	33.85-34.00
1E 1207.4-5209	$5.53^{+0.44}_{0.19}$	$3.85^{+0.48}_{0.48}$	$6.21{+}0.07_{0.07}$	1.3 3.9	33.27 33.74
RX J0002+6246		$3.96^{+0.08}_{0.08}$	$6.03^{+0.03}_{0.03}$	2.5 3.5	33.08 33.33
PSR 0833-45 (Vela)	4.05	$4.26^{+0.17}_{0.31}$	$5.83^{+0.02}_{0.02}$	0.22 0.28	32.41 32.70
PSR 1706-44	4.24		$5.8^{+0.13}_{0.13}$	1.4 2.3	31.81 32.93
PSR 0538+2817	4.47		$6.05^{+0.10}_{0.10}$	1.2	32.6 33.6

[a] sd is the spin-down age of the star availble when measurements of P and $\dot{P}$ can be taken.

[b] kin is the kinematic age of the star.

*Data compiled from Tables 1 and 2 from [73]

Chapter 4

A Virtual Laboratory: Numerical Methods

Heat transport within neutron stars is a subject of much interest due to the exotic nature of the ultra-dense material inside, the nature of which is, for the most part, unknown. Only surface temperatures of these objects can be observed from our current position, and the end goal of modeling the thermal profiles of neutron stars would be to create an accurate-as-possible picture of the cooling of said surfaces. A complete model would include the behavior of material at every depth of the star as well as any other influences to the thermal evolution, such as the presence of a magnetic field and relativistic effects. Such a model would thus be an excellent testing ground for, as an example, the equations of state of matter at supra-nuclear densities. As such, these are our only laboratories for testing ultra-dense matter.

In order to approach this problem, the energy balance equation relevant for regions of interest must be constructed. This equation, which describes thermal evolution within a neutron star and is presented below, can be put into a simplified form of a general diffusion equation for which a numerical method can be devised and tested. A desirable method can be extended to increasingly complicated cases.

In this work, Finite Difference methods are explored in order to solve this problem. The advantages of the methods used in this paper are that they can be modified to achieve second-order accuracy in both space and time, and are generally stable numerical schemes, while not being unnecessarily computationally expensive. The methods used were developed by Press et al. (1986)[85], and adapted accordingly for use with heat diffusion. One-dimensional problems are treated with the Crank-Nicolson method, a combination of implicit and explicit

schemes in order to combine stability with accuracy, while multi-dimensional problems, more the problems of interest, are treated by the Alternating Direction Implicit method (ADI). This last method, as will be shown, allows for second-order accuracy in time by dividing timesteps and for a relatively computationally inexpensive way to solve coupled linear equations.

The purpose of this section is to present a general reference for an algorithm appropriate for use in calculating the thermal history of neutron stars, although its application to other systems not considered here is certainly valid. The relevant equations to be solved are presented followed by their analytical solutions. Next come the Finite Difference schemes and their results compared analytical solutions. The section closes with a discussion of the application of the ADI method to the specific case of neutron star cooling.

4.1. Heat Transport and the Energy Balance Equation

We saw from Equation (3.14) the form of energy transport in the radial direction in terms of the luminosity, L. For modelling purposes it is advantageous to re-write this equation in terms of the change in Temperature, T, with time. For simplicity, we will ignore reletivistic effects such as the redshift factor, e^{Φ}. Equations (3.13) and (3.14) then become:

$$\frac{dL}{dr} = -4\pi r^2 \left(C_v \frac{dT}{dt} + Q_\nu - Q_h \right) \tag{4.1}$$

$$\frac{dT}{dr} = -\frac{1}{\kappa} \frac{L}{4\pi r^2} \tag{4.2}$$

Rearranging (4.1) and substituting (4.2) into it then gives:

$$C_v \frac{dT}{dt} = \frac{1}{r^2} \frac{d}{dr} \left[r^2 \kappa \frac{dT}{dr} \right] - Q_\nu + Q_h \tag{4.3}$$

Putting this equation in terms of the flux, $F = L/4\pi r^2 = -\kappa dT/dr$:

$$C_v \frac{dT}{dt} = -\frac{1}{r^2} \frac{d}{dr} \left[r^2 F \right] - Q_\nu + Q_h \tag{4.4}$$

This can be put more gerally into the following form which can be expanded depending on the number of dimensions to be considered,

$$C_v \frac{\partial T}{\partial t} = -\nabla \cdot \mathbf{F} - \text{Sinks} + \text{Sources} \tag{4.5}$$

where C_v is the specific heat per unit volume. Here, the heat flux, F, is described by,

$$\mathbf{F} = -\hat{\kappa} \cdot \nabla T \tag{4.6}$$

where $\hat{\kappa}$ is the heat conductivity tensor. It will be assumed that the system will be free of heat sources and sinks and C_v and κ will be taken as constant for purposes of simplicity, at least for the time being. Also, general relativistic effects and other influences (e.g. magnetic field) will not be discussed until later.

4.1.1. Heat Transport in Diffusion Equation Form: Constant C_v and κ

The aforementioned approximations simplify (4.5) greatly and thermal evolution in a homogenous medium can be put into a straightforward diffusion equation form,

$$\frac{\partial T}{\partial t} = \frac{\kappa}{C_v}\left(\frac{\partial^2 T}{\partial x^2} + \frac{\partial^2 T}{\partial y^2} + \frac{\partial^2 T}{\partial z^2}\right) \tag{4.7}$$

or, alternatively, in spherical coordinates,

$$\frac{\partial T}{\partial t} = \frac{\kappa}{C_v}\left[\frac{1}{r^2}\frac{\partial}{\partial r}\left(r^2\frac{\partial T}{\partial r}\right) + \frac{1}{r^2\sin\theta}\frac{\partial}{\partial \theta}\left(\sin\theta\frac{\partial T}{\partial \theta}\right) + \frac{1}{r^2\sin^2\theta}\frac{\partial^2 T}{\partial \phi^2}\right] \tag{4.8}$$

While (4.8) is written in three spherical dimensions, it is a simple matter to consider, say, axial symmetry by simply eliminating the last term inside the square brackets. (4.7) and (4.8) will hence, form the basic equations to be solved by the method described below.

Analytical Solution

The aforementioned simplifications, although physically unrealistic, enable analytic solutions to (4.7) and (4.8) to be found, which are a good starting points to test any numerical method. Below are a few cases relevant to this study.

Finite Cube Here, we will consider a homogenous medium defined within a cube with limits,

$$x = 0, \qquad x = l, \qquad y = 0, \qquad y = m, \qquad z = 0, \qquad z = n$$

The corresponding general diffusion equation is defined by (4.7).
Let,

$$a = \sqrt{\frac{\kappa}{C_v}}$$

and the initial condition be described by,

$$u|_{t=0} = f(x, y, z) \tag{4.9}$$

with the boundary condition.

$$u|_{x,y,z=0,l,m,n} = 0 \tag{4.10}$$

Particular solutions of (4.7) that satisfies the initial and boundary conditions (4.9),(4.10) are easily found by separation of variable with the form $u = e^{-\omega^2 t}X(x)Y(y)Z(z)$, the particulars of which can be found in [98]. The general solution is then obtained as follows,

$$u(x, y, z, t) = \sum_{\sigma,\tau,\rho=1}^{\infty} \alpha_{\sigma,\tau,\rho} e^{-\omega^2_{\sigma,\tau,\rho} t} \sin\frac{\sigma\pi x}{l} \sin\frac{\tau\pi y}{m} \sin\frac{\rho\pi z}{n}\,, \tag{4.11}$$

where the coefficients are given by,

$$\alpha_{\sigma,\tau,\rho} = \frac{8}{lmn}\int_0^l\int_0^m\int_0^n f(x, y, z) \sin\frac{\sigma\pi x}{l} \sin\frac{\tau\pi y}{m} \sin\frac{\rho\pi z}{n}\, dx\, dy\, dz\,,$$

and

$$\omega^2_{\sigma,\tau,\rho} = a^2\pi^2\left(\frac{\sigma^2}{l^2} + \frac{\tau^2}{m^2} + \frac{\rho^2}{n^2}\right).$$

It results from (4.11) that the heat does not spread at a finite speed, but instantaneously, which is the primary difference between the heat equation and the wave equation.

Solution for a Sphere The case of spherical coordinates can also be studied and is perhaps more relevant to the case of heat transport in neutron stars considered below. Here, the solution to (4.8) is at first simplified if we consider symmetry in θ and ϕ:

$$\frac{\partial u}{\partial t} = \frac{\kappa}{C_v}\left[\frac{1}{r^2}\frac{\partial}{\partial r}\left(r^2\frac{\partial u}{\partial r}\right)\right],$$

with initial condition,

$$u|_{t=0} = f(r)\,,$$

and boundary conditions,

$$\frac{\partial u}{\partial r} + hu = 0 \qquad \text{for} \qquad r = R\,,$$

where R is the radius of the sphere and the "external heat conductivity" $h > 0$. Supposing a solution of the form,

$$u(r,t) = Ae^{-\omega^2 t}U(r)\,,$$

the details leading to the final solution can be found in [98].

$$u(r,t) = \sum_{n=1}^{\infty} a_n e^{-a^2 k_n^2 t}\frac{\sin k_n r}{r}\,, \tag{4.12}$$

where the coefficients a_n are derived from the initial condition,

$$a_n = \int_0^R rf(r)\sin k_n r dr : \int_0^R \sin^2 k_n r dr\,.$$

The constants k_n are derived from the boundary conditions and are given by the roots of the equation,

$$kR\tan^{-1} kR = 1 - hR\,.$$

4.2. Numerical Methods

4.2.1. Finite Differencing: The Crank-Nicolson Method for One Dimension

Solving the Heat Transport Equation is an initial value problem. That is, given an initial temperature distribution (4.5) describes it's evolution through time. Equation (4.5) is an example of a diffusion equation and can be solved numerically in several ways. However, here we concentrate on "Finite Difference" methods.

A model diffusion equation in one spatial dimension with a constant diffusion coefficient, a^2, is taken from (4.7),

$$\frac{\partial u}{\partial t} = \frac{\kappa}{C_v}\left(\frac{\partial^2 u}{\partial x^2}\right) \tag{4.13}$$

Here, u is the quantity whose evolution through time we are interested in. In Finite Difference form this becomes,

$$\frac{u_i^{n+1} - u_i^n}{\Delta t} = a^2\left[\frac{u_{i+1}^n - 2u_i^n + u_{i-1}^n}{(\Delta x)^2}\right] \tag{4.14}$$

which can then be solved for u_i^{n+1} in a straightforward way. Here, n denotes increments in time (i.e. $n = 1, 2, \ldots, N$ where N is the maximum number of allowed time-steps) and i

denotes increments in space (i.e. $i = 1, 2, \ldots, I$ where I represents the outer boundary of the space in which u is evolving). Differences in u are centered on $i + 1/2$ and $i - 1/2$, otherwise known as *central differences*. The level of accuracy is determined by evaluating the error in the difference between the derivative of u and the limit in the central difference around u divided by Δx as Δx becomes small. The error in this approximation is proportional to the square of the spatial step $(\Delta x)^2$ and the scheme then obtains *second-order accuracy in space*. This is in contrast to *forward* or *backward* difference schemes whose error is on the order of $O(\Delta x)$ or only *first-order accurate* in space.

A numerical scheme such as 4.14 where the searched for value at time step $n + 1$, u^{n+1}, only appears in the l.h.s. time derivative while the r.h.s. spatial derivative is evaluated only at time step n, is called an *explicit scheme*.

A problem arises when considering the Δt required for stability. In general, the diffusion time across a cell size Δx is of the order $\tau \sim \Delta x^2/a^2$ which, for sufficiently small spatial scales and large overall time scales, is prohibitively small.

The goal is to accurately evolve the large-scale features while keeping the small-scale features as innocuous yet accurate as possible. One way to achieve this is to use a "fully-implicit" differencing scheme, as

$$\frac{u_i^{n+1} - u_i^n}{\Delta t} = a^2 \left[\frac{u_{i+1}^{n+1} - 2u_i^{n+1} + u_{i-1}^{n+1}}{(\Delta x)^2} \right]$$

where the searched for values at time step $n + 1$, u^{n+1}, are employed in both the l.h.s. time derivative and the r.h.s. spatial derivative.

It can be easily rearranged into the following form,

$$-\alpha u_{i+1}^{n+1} + (1 + 2\alpha) u_i^{n+1} - \alpha u_{i-1}^{n+1} = u_i^n, \qquad i = 1, 2 \ldots I \tag{4.15}$$

$$\alpha = \frac{a^2 \Delta t}{(\Delta x)^2}$$

Eq. (4.15) represents a tri-diagonal matrix which, with appropriate boundary conditions at $i = 1$ and $i = I$, can be solved at each time step with an appropriate method. Here, the system to be solved is $A \cdot x = B$ where A is an $I \times I$ matrix whose only non-zero elements lie along the diagonal plus or minus one column, as seen by the coefficients of 4.15. The unknown values of u are represented by the column matrix x and B is the right-hand-side

of 4.15. Direct methods to solve the set of equations represented by 4.15 would use $O(I^3)$ operations, a potentially huge number if I is large. However, using a technique that involves "LU decomposition", which is the breaking up of A into matrices with upper, U, and lower, L, triangular elements only, creates a triangular set of equations that are trivial to solve. More importantly, the number of operations is $O(I)$, a significant improvement over more "brute force" methods.

However, another problem arises in the limit $\Delta t \to \infty$. In this limit, 4.13 goes to its equilibrium form,

$$a^2 \frac{\partial^2 u}{\partial x^2} = 0$$

which is unconditionally stable for all Δt and gives the correct equilibrium solution, but is inaccurate at small-scales and only first-order accurate in time.

In order to get an unconditionally stable method that is second-order accurate in space and time, the average of both fully-implicit and fully-explicit methods is taken. This is called the Crank-Nicolson Method and has the following form,

$$\frac{u_i^{n+1} - u_i^n}{\Delta t} = \frac{a^2}{2} \left[\frac{(u_{i+1}^{n+1} - 2u_i^{n+1} + u_{i-1}^{n+1}) + (u_{i+1}^n - 2u_i^n + u_{i-1}^n)}{(\Delta x)^2} \right] \tag{4.16}$$

Here, the left-hand side of the equation is centered on a time step of size $n + 1/2$ and is thus second-order accurate in time. The fully-implicit portion of the equation ensures that it is stable for all Δt. This method, and variations thereof, are used to solve the energy balance equation.

4.2.2. Finite Differencing: Alternating Direction Implicit (ADI) Method, Methods for Multiple Dimensions

The diffusion equation in three dimensions has the general form,

$$\frac{\partial u}{\partial t} = a^2 \left(\frac{\partial^2 u}{\partial x^2} + \frac{\partial^2 u}{\partial y^2} + \frac{\partial^2 u}{\partial z^2} \right) \tag{4.17}$$

Now, this could be put into Crank-Nicolson representation as in 4.16 however, a solution requires solving a series of coupled linear equations. The equations involved still have mostly zero elements, however in order to minimize operations for the special order of more complicated sparse matrix patterns, one must often sacrifice stability. A desirable scheme would reduce the problem to the solution of a tri-diagonal matrix, the "simplest" sparse matrix

form, as in the aforementioned method, which uses the relatively stable regular LU decomposition. In general, 4.17 can be written as,

$$\frac{\partial u}{\partial t} = \Gamma u$$

where Γ is some operator. Furthermore, say the right-hand side of 4.17 can be divided into a linear sum of m pieces as follows,

$$\Gamma u = \Gamma_1 u + \Gamma_2 u + \cdots + \Gamma_m u$$

Suppose that for each operator Γ_m a scheme for updating u from time step n to $n+1$ is known. Then, u could be updated by a series of updating schemes, U_m, each one desirably stable for the Γ_m piece only,

$$\begin{aligned} u^{n+1/m} &= U_1\Big(u^n, \Delta t/m\Big) \\ u^{n+2/m} &= U_2\Big(u^{n+1/m}, \Delta t/m\Big) \\ &\vdots \\ u^{n+1} &= U_m\Big(u^{n+(m-1)/m}, \Delta t/m\Big) \end{aligned}$$

Thus, the time step from n to $n+1$ is divided into m pieces. At each fractional step, one term on the right-hand side of 4.17 is treated implicitly in turn. The three-dimensional diffusion equation would have the form,

$$\begin{aligned} u_{i,j,k}^{n+1/3} &= u_{i,j,k}^n + \frac{1}{3}\alpha\Big(\delta_x^2 u_{i,j,k}^{n+1/3} + \delta_y^2 u_{i,j,k}^n + \delta_z^2 u_{i,j,k}^n\Big) \\ u_{i,j,k}^{n+2/3} &= u_{i,j,k}^{n+1/3} + \frac{1}{3}\alpha\Big(\delta_x^2 u_{i,j,k}^{n+1/3} + \delta_y^2 u_{i,j,k}^{n+2/3} + \delta_z^2 u_{i,j,k}^{n+1/3}\Big) \\ u_{i,j,k}^{n+1} &= u_{i,j,k}^{n+2/3} + \frac{1}{3}\alpha\Big(\delta_x^2 u_{i,j,k}^{n+2/3} + \delta_y^2 u_{i,j,k}^{n+2/3} + \delta_z^2 u_{i,j,k}^{n+1}\Big) \end{aligned} \tag{4.18}$$

where α and $\delta_x^2 u_{i,j,k}^n$ would be the following,

$$\alpha \equiv \frac{a^2 \Delta t}{\Delta^2} \qquad \Delta \equiv \Delta x = \Delta y = \Delta z$$

$$\delta_x^2 u_{i,j,k}^n = u_{i+1,j,k}^n - 2u_{i,j,k}^n + u_{i-1,j,k}^n$$

Each sub-step looks very much like the Crank-Nicolson scheme with the slight difference that heat transfer in each direction is treated implicitly in turn during a time step 1/3 of the original Δt. Now, the solution becomes the relatively simple matter of solving three tri-diagonal systems one after the other. Going back to two-dimesions is straightforward: division of Δt into only two sub-steps and solving the two corresponding tri-diagonal systems.

4.2.3. Comparison with Analytical Solution

The energy balance equation for one-dimension and constant κ and C_v has the following form in the Crank-Nicolson Method,

$$\frac{T_i^{n+1} - T_i^n}{\Delta t} = \frac{\kappa}{C_v}\frac{1}{2r_i^2} \left[\frac{r^2_{i+\frac{1}{2}}(T^{n+1}_{i+1} - T^{n+1}_i) - r^2_{i-\frac{1}{2}}(T^{n+1}_i - T^{n+1}_{i-1})}{(\Delta r)^2} + \frac{r^2_{i+\frac{1}{2}}(T^{n}_{i+1} - T^{n}_i) - r^2_{i-\frac{1}{2}}(T^{n}_i - T^{n}_{i-1})}{(\Delta r)^2} \right] \tag{4.19}$$

Here, the general differencing form of 4.16 has been appropriately modified to a spherical representation (i.e. the right-hand side of 4.19 is not only centered on $n + 1/2$ but also on the spatial coordinate i).

The energy balance equation for three-dimensions in cartesian coordinates takes the form of 4.17 with temperature, T, in place of u and the diffusion coefficient, a^2, replaced with a constant value of $\kappa/C_v = 1$. A comparison with the solution for a finite three-dimensional homogenous medium, 4.11, is shown in Fig. 4.1.

Fig. 4.2 shows the results of using 4.19 to numerically solve the energy balance equation compared with the analytic solution described above for an initial Guassian T-distribution. For illustrative purposes $\kappa = C_v = 1$ was used, as well as $h = 0.1$ for the external boundary condition. For comparison, Fig. 4.1 shows the one-dimensional solution in cartesian coordinates. Colour has been used to show the passage of time, t, with *black* representing $\log t = 0$, *red* $\log t = +/-1$, *green* $\log t = +/-2$, and *blue* $\log t = +/-3$.

However, we are more interested in a spherical coordinate system in order to move to the next step of modeling the interior of a star. The following equations are the spherical

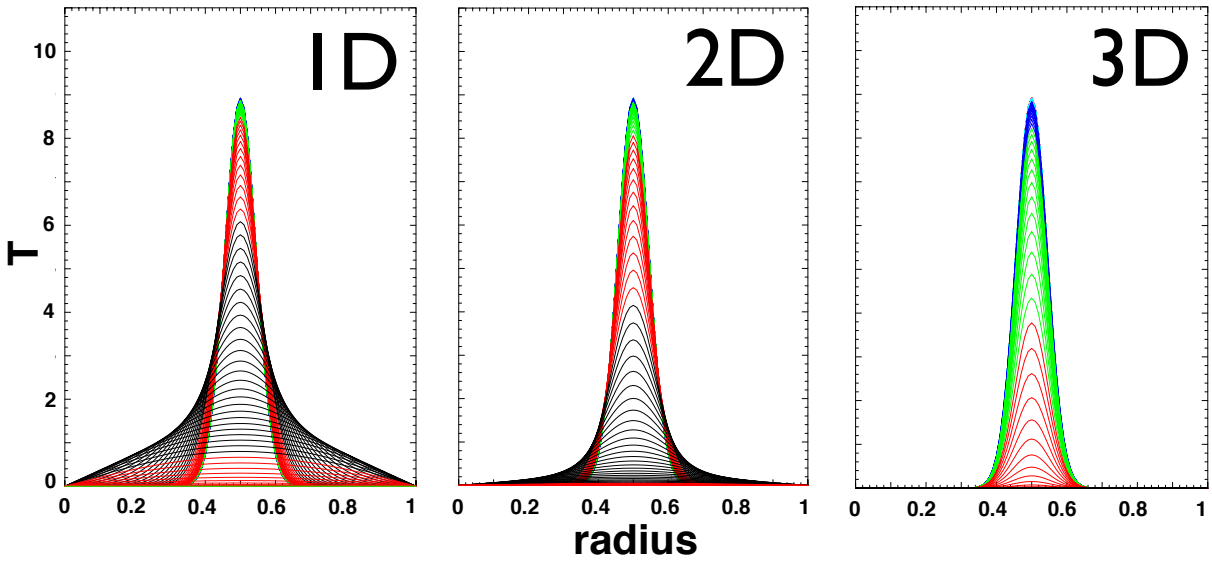

Figure 4.1 One-, Two- and Three-dimensional evolution of the diffusion equation in Cartesian coordinates. Initial temperature distribution is a Gaussian. Colour has been used to show the passage of time, t, with *black* representing $\log t = 0$, *red* $\log t = +1$ *and* -1, *green* $\log t = +2$ *and* -2, and *blue* $\log t = +3$ *and* -3.

equivalents of 4.18, the results of which are shown in Fig. 4.2:

$$\begin{aligned}
T^{n+1/3}_{i,j,k} &= T^{n}_{i,j,k} + \frac{\Delta t}{3}\frac{\kappa}{C_v}\left(\delta^2_r T^{n+1/3}_{i,j,k} + \delta^2_\theta T^{n}_{i,j,k} + \delta^2_\phi T^{n}_{i,j,k}\right) \\
T^{n+2/3}_{i,j,k} &= T^{n+1/3}_{i,j,k} + \frac{\Delta t}{3}\frac{\kappa}{C_v}\left(\delta^2_r T^{n+1/3}_{i,j,k} + \delta^2_\theta T^{n+2/3}_{i,j,k} + \delta^2_\phi T^{n+1/3}_{i,j,k}\right) \\
T^{n+1}_{i,j,k} &= T^{n+2/3}_{i,j,k} + \frac{\Delta t}{3}\frac{\kappa}{C_v}\left(\delta^2_r T^{n+2/3}_{i,j,k} + \delta^2_\theta T^{n+2/3}_{i,j,k} + \delta^2_\phi T^{n+1}_{i,j,k}\right)
\end{aligned} \tag{4.20}$$

with the general δ representations,

$$\begin{aligned}
\delta^2_r T^{n}_{i,j,k} &= \frac{r^2_{i+\frac{1}{2}}\left(T^{n}_{i+1,j,k} - T^{n}_{i,j,k}\right) - r^2_{i-\frac{1}{2}}\left(T^{n}_{i,j,k} - T^{n}_{i-1,j,k}\right)}{r^2_i(\Delta r)^2} \\
\delta^2_\theta T^{n}_{i,j,k} &= \frac{\sin(\theta_{j+\frac{1}{2}})\left(T^{n}_{i,j+1,k} - T^{n}_{i,j,k}\right) - \sin(\theta_{j-\frac{1}{2}})\left(T^{n}_{i,j,k} - T^{n}_{i,j-1,k}\right)}{r^2_i \sin(\theta_j)(\Delta\theta)^2} \\
\delta^2_\phi T^{n}_{i,j,k} &= \frac{\left(T^{n}_{i,j+1,k} - T^{n}_{i,j,k}\right) - \left(T^{n}_{i,j,k} - T^{n}_{i,j-1,k}\right)}{r^2_i \sin^2(\theta_j)(\Delta\phi)^2}
\end{aligned}$$

In contrast to the one-dimensional cases, two- and more so three-dimensional cooling appears more efficient and temperature will continue to decrease even as it's profile reaches isothermality. The greatest practical difference is, of course, computational expense as the number of operations increases with increasing dimension. Depending on the system and complexity of the input, a one-dimensional calculation could take on the order of minutes to complete, while a three-dimensional one could be on the order of days.

Now, the next step would be to apply more realistic physical parameters to 4.20, which will be discussed briefly below. The inclusion of realistic physics along with appropriate initial and boundary conditions into this numerical method will then provide a successful means by which solve heat transport within a neutron star.

4.3. 1D Neutron Star Modeling

The inclusion of non-constant physical coefficients can be a bit tricky. However, if they can be treated as dependent on only one spatial dimension the problem becomes significantly easier. For example, say the diffusion coefficient of 4.16 depended on x. Then, it could be

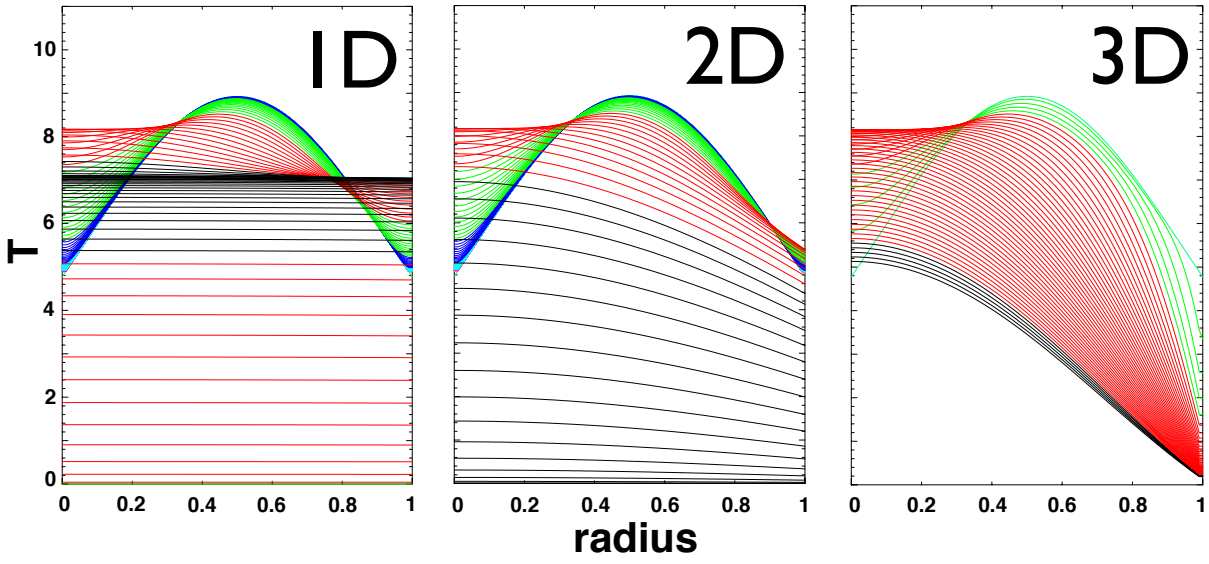

Figure 4.2 One-, Two-, and Three-dimensional evolution of the diffusian equation in Spherical coordinates. Initial temperature distribution is a Gaussian (*blue*). Although computationally more expensive, cooling appears more efficient, specifically at the surface. Colour has been used to show the passage of time, t, with *black* representing $\log t = 0$, *red* $\log t = +1$ *and* -1, *green* $\log t = +2$ *and* -2, and *blue* $\log t = +3$ *and* -3.

included in the difference over i of the difference in flux in the following way,

$$\frac{u_i^{n+1}-u_i^n}{\Delta t} = \frac{1}{2}\left[\frac{a^2_{i+\frac{1}{2}}(u_{i+1}^{n+1}-u_i^{n+1})-a^2_{i-\frac{1}{2}}(u_i^{n+1}-u_{i-1}^{n+1})}{(\Delta x)^2} + \frac{a^2_{i+\frac{1}{2}}(u_{i+1}^{n}-u_i^{n})-a^2_{i-\frac{1}{2}}(u_i^{n}-u_{i-1}^{n})}{(\Delta x)^2}\right] \tag{4.21}$$

This was seen above in the spherical coordinate representation of the diffusion equation, 4.19 and 4.20 where the physical coefficient a would now become part of the δ flux terms. This is easily extendible to the case of three-dimensional heat transport within a neutron star when considering C_v and κ borne from a particular equation of state (EOS) considered in the stellar model. Then physical properties of the star can be calculated depending on temperature and radius of the point in the star for which temperature flow is being calculated. Unfortunately, solving for these coefficients implicitly along with heat flux is prohibitively complicated since they themselves depend on the temperature, T. However, combining the aforementioned Finite Differencing methods with an iterative method to solve for the physical coefficients within a desired range works just as well, enabling an overall method that is still second-order accurate in both space and time. As well, adding an iterative component to the method helps to reduce numerical errors produced by the precision limit of the machine on which the simulation is running.

Similarly to adding physical coefficients that depend on spatial coordinates, other influences in the heat transport problem such as relativistic effects, neutrino emission and the presence of a magnetic field (see §4.4) can be successfully added to the ADI scheme. Factors such as redshift and length correction depend on global properties of the model and can be included as depending on only the radial dimension. Heat sinks such as neutrino emissivity, Q_ν, which depend on both depth within the star and local temperature can be solved for iteratively, as in the case of specific heat, C_v.

The majority of the input physics to the code used to produce the results presented here in this project were generated from pre-existing subroutines in the cooling code *NSCool* from Dr. Dany Page which uses a Henyey scheme in one dimension. An interface was written in order to communicate between the two codes while leaving their constituent subroutines and variables completely separate. In all cases, an initial temperature of $T = 10^{10}K$ is taken throughout the star.

Boundary Conditions In the radial direction, $F_r = 0$ is taken at the center of the star and at the surface $\tilde{F}_{r,i-1/2} = \sigma_{SB} T_{s,j}^4 e^{2\Phi}$ is evaluated using an appropriate $T_b - T_s$ relation depending on the model star being considered. When solving heat transport in the θ and ϕ directions, solutions at $r = 0$ and $r = R_{star}$ are not calculated. Along the poles, the ϕ-direction is not calculated and $F(\theta = 0) = F(\theta = \frac{\pi}{2}) = 0$. There are no true bounds in the ϕ-direction, however some must be imposed in order to take advantage of the relatively easy-to-solve tri-dimensional system. Therefore, the fact that $T(r, \theta, \phi = 0) = T(r, \theta, \phi = 2\pi)$ is imposed using temperatures calculated form the previous iteration.

Results Results from the one-dimensional ADI scheme described above are presented in Fig. 4.3. Each curve represents the temperature profile along depth in the star. As the star cools with time, different physical processes are activated (or deactivated as the case may be) at different densities. The top left panel shows a cooling neutron star without any pairing processes switched on. At earlier times, there is a marked difference in thermal profile between the crust and the core (marked on the upper edge of the panel at a density just above 10^{14} gcm^{-3}) as the crust cooling catches up to the more rapid neutrino cooling in the core. By an age of ~ 1000 years, the star is essentially isothermal and cooling passively by photons.

The other three panels of Fig. 4.3 show the effect on the model neutron star thermal profile as pairing channels are turned on. In the upper right hand side panel the neutron $^1S_0$ channel has been switched on, the effect of which can be clearly seen in the deep inner crust. The lower panels have the proton $^1S_0$ (left) and the neutron $^3P_2$ (right) processes added successively. The proton $^1S_0$ gap vanishes in the inner core whereas the neutron $^3P_2$ gap is more likely to reach the centre with high values. The dotted lines are the T_c values for each process included in each panel for comparison.

Though the effects of pairing on internal temperature within the star are evident in Fig. 4.3, the overall effect on the observable quantity of effective temperature, T_{eff}, is not immediately noticeable as each stellar configuration reaches near-isothermality at a similar age. Fig. 4.4 then compares the cooling evolution of T_{eff} (or T_e) with stellar age. The right hand side panel shows the observable difference between the model stars of Fig. 4.3. There are two regions where the confirmation of the presence of these processes within a neutron star could be verified: at the relatively young age of 10's to 100's of years as T drops below

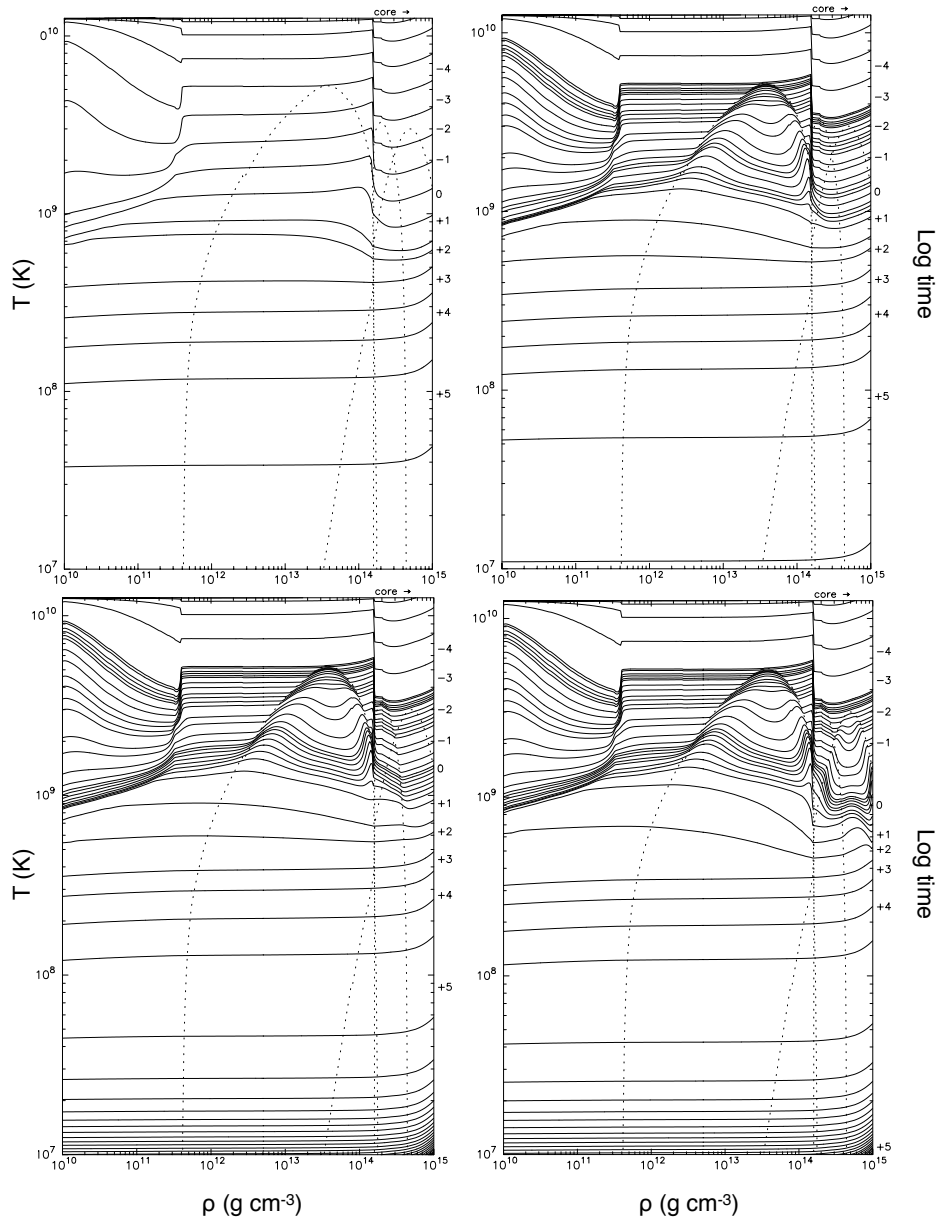

Figure 4.3 Local temperature evolution profile for 1D model neutron stars. The numbers along the right axis denote the Log of approximate age in years. *Top Left:* No pairing effects although the curves for T_c have been inserted for comparison (*dotted lines*). *Top Right*: The neutron $^1S_0$ process has been taken into account. The curve for the critical Temperature, T_c, can be clearly seen in the inner crust and core. *Bottom Left:* In this model, the proton $^1S_0$ process has been added. It's effect can be seen in the outer core. *Bottom Right:* The Neutron $^3P_2$ process has been added here and its effect can be clearly seen within the core.

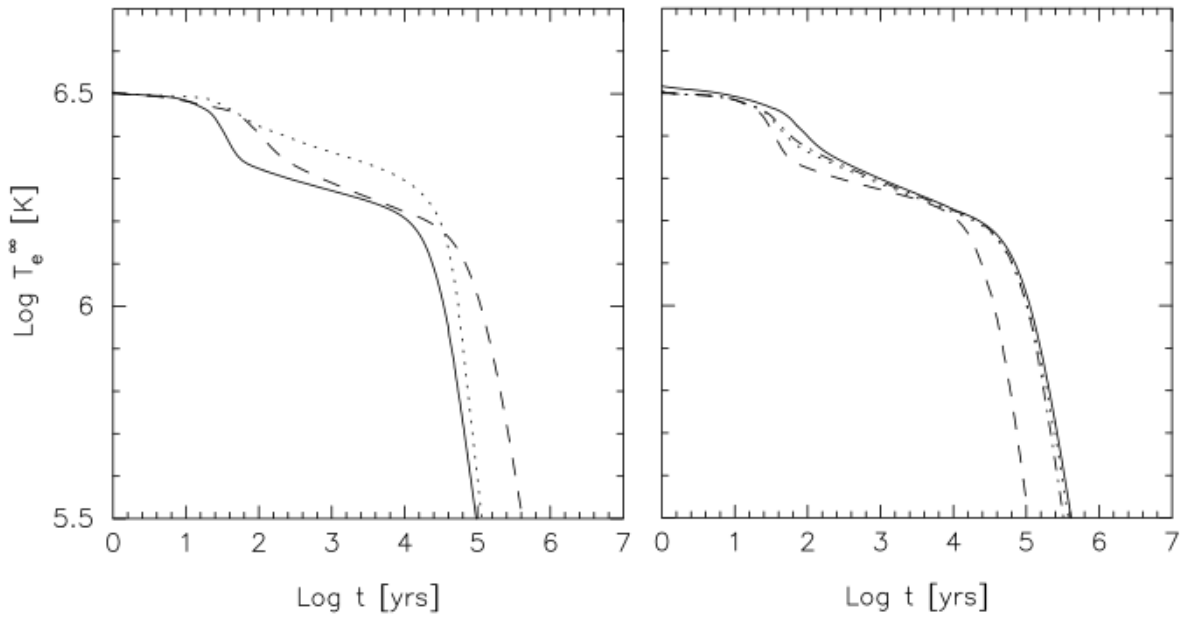

Figure 4.4 *Left:* Cooling curves for three model stars showing the importance of the PBF (Pairing Breaking and Formation) process: *dashed line* - no pairing; *dotted line*- pairing without PBF; *solid line* pairing with PBF. *Right:* cooling curves for four models stars showing the effect of including various pairing processes: *sold line* - no pairing; *dotted line* - N^1S_0 only; *dash-dot line*- N^1S_0 + P^1S_0; *dashed line* - N^1S_0 + P^1S_0 + N^3P_2.

T_c; and possibly during the photon cooling era for stars older than 10^5 years old where, according to the results presented here, the addition of the neutron $^3P_2$ process has cooled the star significantly faster.

In all the above model stars that include pairing effects, enhanced cooling from neutrinos produced in PBF processes have also been included. The left hand side of Fig. 4.4 shows the importance of this process on the evolution of T_{eff}. Without its inclusion (dotted curve) the star stays significantly warmer longer as T drops below T_c. This characteristic rapid cooling due to neutron superfluidity shown in both panels of Fig. 4.4 are evidence as presented by Page et al [75] in the case of Cassiopeia A, observations of which over time confirmed that superfluidity must have been "switched on".

4.4. 2D with Magnetic Field

As mentioned in the *Introduction*, magnetic field strength, configuration and location can have severe consequences on the heat flow within magnetized neutron star crusts. In the following model it is assumed that the core, where $\rho \geq 10^{14}$ g cm^{-3}, is composed of a Type II superconductor that provides an impenetrable barrier to the magnetic field. Thus, the core is considered isothermal and heat anisotropies are confined to the crust. The spherically axis-symmetric cases of a *poloidal* and *poloidal + toroidal* field are shown below [32].

4.4.1. Poloidal and Toroidal Fields

The core field, $\mathbf{B^{core}}$, is a dipolar field maintained by axis-symmetric currents in the core. A vacuum-like dipolar field will penetrate the crust with components oriented along the symmetry axis,

$$B_r^{core} = B_o^{core}\frac{\cos\theta}{x^3} \tag{4.22}$$

$$B_\theta^{core} = -\frac{B_o^{core}}{2}\frac{\sin\theta}{x^3} \tag{4.23}$$

$$B_\phi^{core} = 0 \tag{4.24}$$

where B_o^{core} is the magnitude of the magnetic field at the pole on the surface of the star and $x = r/R_{NS}$ is the dimensionless radial coordinate normalized to the neutron star radius, R_{NS}.

The crustal poloidal field, $\mathbf{B^{crust}}$, is maintained by toroidal currents circulating in the crust. The crust field, which continues beyond the surface as a dipolar vacuum field, is described by the Stokes Stream Function, $S = S(r,t)$.

$$B_r^{crust} = \frac{2\cos\theta}{r^2}S(r,t) = B_o^{crust}\frac{\cos\theta}{x^2}s(x,t) \tag{4.25}$$

$$B_\theta^{crust} = \frac{\sin\theta}{r}\frac{\partial S(r,t)}{\partial r} = \frac{B_o^{crust}}{2}\frac{\sin\theta}{x}\frac{\partial s(x,t)}{\partial x} \tag{4.26}$$

$$B_\phi^{crust} = 0 \tag{4.27}$$

where B_o^{crust} is the strength of the field at the pole and s is the normalized Stokes Function $s = 2S/B_o^{crust}/R_{NS}^2$ which satisfies the boundary condition $s = 0$ at the crust-core boundary and $s = 1$ with $\partial s/\partial x = -1$ at the surface.

From Maxwell's equation $\nabla \wedge \mathbf{B} = (\mathbf{4}\pi/\mathbf{c})\mathbf{j}$, with $\mathbf{j}$ being the electric current density, one deduces that $\mathbf{j}$ is todoidal with a ϕ component

$$j_{\phi}^{crust} = \frac{c}{4\pi}\frac{\sin\theta}{r}\frac{\partial}{\partial r}\left(\frac{\partial S}{\partial r} - \frac{2S}{r^2}\right) \tag{4.28}$$

while j_r and j_θ vanish. Besides its boundary conditions, S is arbitrary and its choice is, thus, equivalent to choosing where the currents generating the crust field are located in the crust.

Toroidal Fields The crustal toroidal field, $\mathbf{B^{tor}}$, is maintained by poloidal currents circulating in the crust. It is entirely confined to the crust, thus vanishes at the surface and does not penetrate the core. Therefore, $\mathbf{B^{tor}}$ does not have components in r or θ directions:

$$B_{\phi}^{tor} = \frac{\sin\theta}{r}T(r,t) = B_o^{tor}\frac{\sin\theta}{x}t(x,t) \tag{4.29}$$

where t derives from the same formalism as s, however, it must vanish at the surface and crust-core boundary while its maximum value is 1 at an arbitrary location with the crust. The currents producing the toroidal field are then given by

$$\begin{aligned} j_r^{tor} &= \frac{c}{4\pi}\frac{2\cos\theta}{r^2}T \\ j_\theta^{tor} &= -\frac{c}{4\pi}\frac{\sin\theta}{r}\frac{\partial T}{\partial r} \\ j_\phi^{tor} &= 0 \end{aligned} \tag{4.30}$$

As for the poloidal field, a choice of T is equivalent to choosing where the electric currents generating $\mathbf{B^{tor}}$ are located in the crust.

The total dipolar field has thus been decomposed in three components, two poloidal field, with currents in the core and in the crust, and one toroidal component with currents in the crust. A next, and natural, step would be to add higher order component (quadrupolar, both poloidal and toroidal, ...).

4.4.2. The 2D Algorithm

Considering that energy transport in neutron stars will be affected by the presence of a magnetic field as it re-directs heat carriers, the equation for heat Flux, $\mathbf{F}$ from Equation 4.6, must be revisited. The temperature gradient will be divided into terms parallel and

perpendicular to the magnetic field, $\mathbf{b}$, in the following way:

$$\begin{aligned}
\big(\boldsymbol{\nabla} T\big)_{\parallel} &= \big(\boldsymbol{\nabla} T \cdot \mathbf{b}\big)\mathbf{b} \\
\big(\boldsymbol{\nabla} T\big)_{\perp} &= \mathbf{b} \wedge \big(\boldsymbol{\nabla} T \wedge \mathbf{b}\big) = \boldsymbol{\nabla} T - \big(\boldsymbol{\nabla} T\big)_{\parallel} \\
\big(\boldsymbol{\nabla} T\big)_{\wedge} &= \mathbf{b} \wedge \boldsymbol{\nabla} T
\end{aligned}$$

where $\mathbf{b} \equiv \mathbf{B}/B$ is the unit vector in the direction of $\mathbf{B}$. The last term is the *Hall* component - a non-linear term in the magnetic induction equation for the evolution of magnetic fields resulting from a transverse force exerted on charge carriers by the magnetic field. Combining this expression for the temperature gradient with the tensor of thermal conductivity from Equation 3.37 gives the new expression for the heat flux

$$\begin{aligned}
\mathbf{F} &= -\hat{\kappa} \cdot \boldsymbol{\nabla} T = -\kappa_{\parallel}\big(\boldsymbol{\nabla} T\big)_{\parallel} - \kappa_{\perp}\big(\boldsymbol{\nabla} T\big)_{\perp} - \kappa_{\wedge}\big(\boldsymbol{\nabla} T\big)_{\wedge} \\
&= -(\kappa_{\parallel} - \kappa_{\perp})\big(\boldsymbol{\nabla} T \cdot \mathbf{b}\big)\mathbf{b} - \kappa_{\perp}\boldsymbol{\nabla} T - \kappa_{\wedge}\mathbf{b} \wedge \boldsymbol{\nabla} T
\end{aligned} \tag{4.31}$$

Using the expressions of Eq. (3.38), 3.39, and 3.40, one may explicitely obtain

$$\mathbf{F} = -\frac{\kappa_0}{1 + (\omega_B \tau)^2}\left[\boldsymbol{\nabla} T + (\omega_B \tau)^2 (\boldsymbol{\nabla} T \cdot \mathbf{b})\,\mathbf{b} + (\omega_B \tau)\,\mathbf{b} \wedge \boldsymbol{\nabla} T\right] . \tag{4.32}$$

An immediate consequence is that

$$\mathbf{F} \cdot (-\boldsymbol{\nabla} T) = \frac{\kappa_0}{1 + (\omega_B \tau)^2}\left[(\boldsymbol{\nabla} T)^2 + (\omega_B \tau)^2 (\boldsymbol{\nabla} T \cdot \mathbf{b})^2\right] > 0 \tag{4.33}$$

so that even if $\mathbf{F}$ is not aligned with $-\boldsymbol{\nabla} T$ the angle between the two is less than $90°$. In other words, the heat flow points toward decreasing T, in agreement with the Second Law of Thermodynamics!

The addition of the magnetic field complicates the Finite Differencing scheme somewhat by adding temperature gradients from each direction into each step of the ADI method of solving heat transport of the form $\mathbf{A} \cdot x = b$.

Expanding the above Equation 4.31 for *two dimensions only* and adding relativistec effects gives the following expressions for the radial, r, and meridonal, θ components of the Flux:

$$F_r = -e^{\Phi}\left[(\kappa_{\parallel} - \kappa_{\perp}) b_r (b_r \nabla_r \tilde{T} + b_\theta \nabla_\theta \tilde{T}) + \kappa_{\perp} \nabla_r \tilde{T} - \kappa_{\wedge} b_\phi \nabla_\theta \tilde{T}\right] \tag{4.34}$$

$$F_\theta = -e^{\Phi}\left[(\kappa_{\parallel} - \kappa_{\perp}) b_\theta (b_r \nabla_r \tilde{T} + b_\theta \nabla_\theta \tilde{T}) + \kappa_{\perp} \nabla_\theta \tilde{T} + \kappa_{\wedge} b_\phi \nabla_r \tilde{T}\right] \tag{4.35}$$

or, grouping the ∇_r and ∇_θ terms, and intruducing conductivity coefficients, χ and ξ:

$$F_r = -e^{\Phi}\Big[\chi_r \nabla_r \tilde{T} + \xi_r \nabla_\theta \tilde{T}\Big] \tag{4.36}$$

$$F_\theta = -e^{\Phi}\Big[\chi_\theta \nabla_\theta \tilde{T} + \xi_\theta \nabla_r \tilde{T}\Big] \tag{4.37}$$

where

$$\chi_r = \big\{(\kappa_\parallel - \kappa_\perp) b_r^2 + \kappa_\perp\big\} = \frac{\kappa_0}{1+(\omega_B\tau)^2}\left[(\omega_B\tau)^2 b_r^2 + 1\right] \tag{4.38}$$

$$\xi_r = \big\{(\kappa_\parallel - \kappa_\perp) b_r b_\theta - \kappa_\wedge b_\phi\big\} = \frac{\kappa_0}{1+(\omega_B\tau)^2}\left[(\omega_B\tau)^2 b_r b_\theta - (\omega_B\tau) b_\phi\right] \tag{4.39}$$

$$\chi_\theta = \big\{(\kappa_\parallel - \kappa_\perp) b_\theta^2 + \kappa_\perp\big\} = \frac{\kappa_0}{1+(\omega_B\tau)^2}\left[(\omega_B\tau)^2 b_\theta^2 + 1\right] \tag{4.40}$$

$$\xi_\theta = \big\{(\kappa_\parallel - \kappa_\perp) b_r b_\theta + \kappa_\wedge b_\phi\big\} = \frac{\kappa_0}{1+(\omega_B\tau)^2}\left[(\omega_B\tau)^2 b_r b_\theta + (\omega_B\tau) b_\phi\right] \tag{4.41}$$

These last terms in each of the above expressions, $\nabla_\theta \tilde{T}$ in F_r and $\nabla_r \tilde{T}$ in F_θ, complicates rearrangement of the heat transport equation into a neat tri-diagonal form of the matrix $\mathbf{A}$. If these terms were to be treated implicitly in each step, the equation could be rearranged into a *sparse matrix* form on one side. There are methods for solving sparse matrix systems (for example the *Biconjugate Gradient* method [84]) however they are more computationally expensive and have not yet been investigated in the scope of this project.

Now we need to take these changes to the conductivity coefficients of our star and return to the general heat diffusion equation:

$$C_V \frac{\partial T}{\partial t} = -\boldsymbol{\nabla}\cdot\boldsymbol{F} - Q_\nu \quad \text{with} \quad \boldsymbol{F} \equiv -\boldsymbol{\kappa}\cdot\boldsymbol{\nabla}T \tag{4.42}$$

gives in 2D spherical coordinates with axi-symmetry

$$\begin{aligned}
C_V \frac{\partial T}{\partial t} &= -\frac{1}{r^2}\frac{\partial}{\partial r}\left(r^2 F_r\right) - \frac{1}{r\sin\theta}\frac{\partial}{\partial\theta}\left(\sin\theta F_\theta\right) - Q_\nu \\
&= \frac{1}{r^2}\frac{\partial}{\partial r}\left(r^2\chi_r\nabla_r T + r^2\xi_r\nabla_\theta T\right) + \\
&\quad \frac{1}{r\sin\theta}\frac{\partial}{\partial\theta}\left(\sin\theta\chi_\theta\nabla_\theta T + \sin\theta\xi_\theta\nabla_r T\right) - Q_\nu \\
&= \frac{1}{r^2}\frac{\partial}{\partial r}\left(\chi_r r^2\frac{\partial T}{\partial r} + \xi_r r\frac{\partial T}{\partial\theta}\right) + \\
&\quad \frac{1}{r\sin\theta}\frac{\partial}{\partial\theta}\left(\chi_\theta\frac{\sin\theta}{r}\frac{\partial T}{\partial\theta} + \xi_\theta\sin\theta\frac{\partial T}{\partial r}\right) - Q_\nu
\end{aligned} \tag{4.43}$$

and let's rewrite it as

$$\frac{\partial T}{\partial t} = G_{rr} + G_{r\theta} + G_{\theta\theta} + G_{\theta r} - Q_\nu/C_v \tag{4.44}$$

where

$$
\begin{aligned}
G_{rr} &\equiv \frac{1}{C_V}\frac{1}{r^2}\frac{\partial}{\partial r}\left(\chi_r r^2 \frac{\partial T}{\partial r}\right) \\
G_{r\theta} &\equiv \frac{1}{C_V}\frac{1}{r^2}\frac{\partial}{\partial r}\left(\xi_r r \frac{\partial T}{\partial \theta}\right) \\
G_{\theta\theta} &\equiv \frac{1}{C_V}\frac{1}{r\sin\theta}\frac{\partial}{\partial \theta}\left(\chi_\theta \frac{\sin\theta}{r}\frac{\partial T}{\partial \theta}\right) \\
G_{\theta r} &\equiv \frac{1}{C_V}\frac{1}{r\sin\theta}\frac{\partial}{\partial \theta}\left(\xi_\theta \sin\theta \frac{\partial T}{\partial r}\right)
\end{aligned}
$$

When discretising in time, in the spirit of the Crank-Nicholson scheme, the r.h.s. is taken as time average of its values at t_n and $t_{n+1} = t_n + \Delta t$:

$$
\begin{aligned}
T^{n+1} - T^n &= \frac{\Delta t}{2}[G_{rr} + G_{r\theta} + G_{\theta\theta} + G_{\theta r} - Q_\nu/C_v]^{n+1} + \\
&\quad \frac{\Delta t}{2}[G_{rr} + G_{r\theta} + G_{\theta\theta} + G_{\theta r} - Q_\nu/C_v]^{n} \qquad (4.45)
\end{aligned}
$$

(exponents n and $n+1$ refer to values at times t_n and t_{n+1}). The first term in the r.h.s. at t_{n+1} must be found by iterating on $T^{n+1,m}$ since it contains T^{n+1} implicitly. Moreover, when discretizing in space the cross-derivatives in r and θ would link values of T at five adjacent mesh point.

It is initially tempting to take Eq. (4.45) and put it into an ADI scheme, where firstly the θ-terms are solved for implicitly with all the other T-dependant terms solved for iteratively, then secondly to do the same but with the radial terms now solved for implitly. Experience with attempting to implement the ADI method with non-constant coefficients, however, has shown that the iterations in the first step will not converge, resulting in an unstable code. Therefore, the trick is to solve Eq. (4.45) in such a way as to maintain the accuracy and stability of an ADI scheme meanwhile including the now complicated T-dependant conductivity coefficients.

It is valuable to notice that the second step of the aforementioned ADI scheme, where the radial flux terms were solved for implicity, did converge to a solution within the allotted maximum number of iterations. Therefore, why not keep the time-averaging operator of Eq. (4.45) for accuracy and it's overall form for stability while solving for the G_{rr}^{n+1} term implicitly and the other t^{n+1} terms iteratively. The stability of this new scheme is reinforced by the explicit t^n terms.

More explicitly, the scheme is:

$$T_{i,j}^{n+1,m+1} - T_{i,j}^{n} = \frac{\Delta t}{4}[G_{rr}]_{i,j}^{n+1,m|m+1} + \frac{\Delta t}{4}[G_{r\theta} + G_{\theta\theta} + G_{\theta r} - Q_\nu/C_v]_{i,j}^{n+1,m} + \frac{\Delta t}{4}[G_{rr} + G_{r\theta} + G_{\theta\theta} + G_{\theta r} - Q_\nu/C_v]_{i,j}^{n} \quad (4.46)$$

where the exponents in the r.h.s. mean:

- third line: n means the physics (C_V, Q_ν and the χ's and ξ's) and the spatial gradients are evaluated using the known T^n at previous time step.
- second line: $n+1, m$ means the physics and the spatial gradients are evaluated using the known $T^{n+1,m}$ from the previous iteration.
- first line: $n+1, m|m+1$ means the physics is evaluated using the known $T^{n+1,m}$ from the previous iteration while the spatial gradients in r use the searched for $T^{n+1,m+1}$.

Thus, for given i, the r.h.s. of Eq. (4.46) only contains the searched for $T_{i-1,j}^{n+1,m+1}$, $T_{i,j}^{n+1,m+1}$, and $T_{i,j+1}^{n+1,m+1}$, leading to a tri-diagonal matrix in i (for each j).

The full numerical scheme can now be written as follows:

Upper time indices mean, depending where the G_{xx} term is used:

$p = n$ in the third line

$p = n+1, m$ in the first and second line.

$p' = n+1, m+1$, in the first line for the fully implicit part: this implements the "$n+1, m|m+1$" notations of Eq. (4.46) and is only used for G_{rr}.

Reintroducing now the GR corrections, this gives us

$$[G_{rr}]^p_{i,j} = \frac{1}{[C_V]^p_{i,j}} \frac{1}{r_i^2} \frac{1}{\Delta l_i} \times \tag{4.47}$$
$$\left[e^{\Phi}_{i+1/2} [\chi_r]^p_{i+1/2,j} r^2_{i+1/2} \left(\frac{\tilde{T}^{p'}_{i+1,j} - \tilde{T}^{p'}_{i,j}}{\Delta l_{i+1/2}} \right) - \right.$$
$$\left. e^{\Phi}_{i-1/2} [\chi_r]^p_{i-1/2,j} r^2_{i-1/2} \left(\frac{\tilde{T}^{p'}_{i,j} - \tilde{T}^{p'}_{i-1,j}}{\Delta l_{i-1/2}} \right) \right]$$

$$[G_{r\theta}]^p_{i,j} = \frac{1}{[C_V]^p_{i,j}} \frac{1}{r_i^2} \frac{1}{\Delta l_i} \times \tag{4.48}$$
$$\left[e^{\Phi}_{i+1/2} [\xi_r]^p_{i+1/2,j} r_{i+1/2} \left(\frac{\tilde{T}^{p}_{i+1/2,j+1/2} - \tilde{T}^{p}_{i+1/2,j-1/2}}{\Delta \theta_j} \right) - \right.$$
$$\left. e^{\Phi}_{i-1/2} [\xi_r]^p_{i-1/2,j} r_{i-1/2} \left(\frac{\tilde{T}^{p}_{i-1/2,j+1/2} - \tilde{T}^{p}_{i-1/2,j-1/2}}{\Delta \theta_j} \right) \right]$$

$$[G_{\theta\theta}]^p_{i,j} = \frac{1}{[C_V]^p_{i,j}} \frac{1}{r_i \sin\theta_j} \frac{1}{\Delta \theta_j} \times \tag{4.49}$$
$$\left[e^{\Phi}_{i} [\chi_\theta]^p_{i,j+1/2} \frac{\sin\theta_{j+1/2}}{r_i} \left(\frac{\tilde{T}^{p'}_{i,j+1} - \tilde{T}^{p'}_{i,j}}{\Delta \theta_{j+1/2}} \right) - \right.$$
$$\left. e^{\Phi}_{i} [\chi_\theta]^p_{i,j-1/2} \frac{\sin\theta_{j-1/2}}{r_i} \left(\frac{\tilde{T}^{p'}_{i,j} - \tilde{T}^{p'}_{i,j-1}}{\Delta \theta_{j-1/2}} \right) \right]$$

$$[G_{\theta r}]^p_{i,j} = \frac{1}{[C_V]^p_{i,j}} \frac{1}{r_i \sin\theta_j} \frac{1}{\Delta \theta_j} \times \tag{4.50}$$
$$\left[e^{\Phi}_{i} [\xi_\theta]^p_{i,j+1/2} \sin\theta_{j+1/2} \left(\frac{\tilde{T}^{p}_{i+1/2,j+1/2} - \tilde{T}^{p}_{i-1/2,j+1/2}}{\Delta l_i} \right) - \right.$$
$$\left. e^{\Phi}_{i} [\xi_\theta]^p_{i,j-1/2} \sin\theta_{j-1/2} \left(\frac{\tilde{T}^{p}_{i+1/2,j-1/2} - \tilde{T}^{p}_{i-1/2,j-1/2}}{\Delta l_i} \right) \right]$$

Physical values are defined on the grid points that are located at

r_i: $i = 0, \ldots, I$, with $r_0 = 0$ and $r_I = R_b$ (with ρ_b usually taken as $\simeq 10^{10}$ g cm^{-3}). Values of r_i are *not* necessarily equally spaced. l_i is obtained from r_i as $l_i \equiv r_i/\sqrt{1-2Gm_i/r_ic^2}$.

θ_j: $j = 0, \ldots, J$, with $\theta_0 = 0^\circ$ and $\theta_J = 180^\circ$. Values of θ_j are equally spaced.

Quantities evaluated at half-integer points are defined as averages from neighbouring points. E.g. $T_{i+1/2,j} \equiv \frac{1}{2}(T_{i,j}+T_{i+1,j})$, $\theta_{j+1/2} \equiv \frac{1}{2}(\theta_{j+1}+\theta_j)$. In the case of more complicated physical quantities, as, e.g., C_V, there are two ways of averaging them. One could define $[C_V]_{i+1/2,j} \equiv \frac{1}{2}([C_V]_{i,j}+[C_V]_{i+1,j})$ (and similarly for $i, j+1/2$ and other half integer grid points). However, since actually $[C_V]_{i,j} = C_V(r_i, \theta_j; T_{i,j})$ where the r, θ dependence encompasses dependence on ρ, chemical composition, etc, ... and other time-independent quantities that could easily be calculated at $r_{i+1/2}$, one could also alternatively define $[C_V]_{i+1/,j} = C_V(r_{i+1/2}, \theta_j; T_{i+1/2,j})$. This second definition is physically more accurate: the physics at the average is not the average of the physics, particularly for quantities with strong T dependence.

Intervals, for the derivatives, are defined by consistency of the discretisation procedure:

$$\Delta l_i \equiv (l_{i+1} - l_{i-1})/2 \ , \ \Delta l_{i+1/2} \equiv l_{i+1} - l_i \ , \ \Delta l_{i-1/2} \equiv l_i - l_{i-1}$$
$$\Delta\theta_j \equiv (\theta_{j+1} - \theta_{j-1})/2 \ , \ \Delta\theta_{j+1/2} \equiv \theta_{j+1} - \theta_j \ , \ \Delta\theta_{j-1/2} \equiv \theta_j - \theta_{j-1}$$

With the detailed expressions Eq. (4.48), (4.49), (4.50), and (4.51) for the G_{xx} terms we can write explicitly the tri-diagonal equations as

$$DU_j(i)\ \tilde{T}^{n+1,m+1}_{i+1,j} + D_j(i)\ \tilde{T}^{n+1,m+1}_{i,j} + DL_j(i)\ \tilde{T}^{n+1,m+1}_{i-1,j} = R_j(i) \tag{4.51}$$

where

$$DU_j(i) = -\frac{\Delta t}{4}\ \frac{1}{\Delta l_i \Delta l_{i+1/2}}\ \frac{e^\Phi_{i+1/2} r^2_{i+1/2}}{r_i^2}\ \frac{[\chi_r]^{n+1,m}_{i+1/2,j}}{[C_V]^{n+1,m}_{i,j}} \tag{4.52}$$

$$DL_j(i) = -\frac{\Delta t}{4}\ \frac{1}{\Delta l_i \Delta l_{i-1/2}}\ \frac{e^\Phi_{i-1/2} r^2_{i-1/2}}{r_i^2}\ \frac{[\chi_r]^{n+1,m}_{i-1/2,j}}{[C_V]^{n+1,m}_{i,j}} \tag{4.53}$$

$$DL_j(i) = 1 - [DU_j(i) + DL_j(i)] \tag{4.54}$$

$$\begin{aligned} R_j(i) &= T^{n+1/2}_{i,j} + \frac{\Delta t}{4}[G_{r\theta} + G_{\theta\theta} + G_{\theta r} - e^{2\Phi} Q_\nu / C_v]^{n+1,m}_{i,j} \\ &+ \frac{\Delta t}{4}[G_{rr} + G_{r\theta} + G_{\theta\theta} + G_{\theta r} - e^{2\Phi} Q_\nu / C_v]^{n+1/2}_{i,j} \end{aligned} \tag{4.55}$$

while for $i = 1$, and $i = I$ we simply have:

$$\tilde{T}^{n+1,m+1}_{2,j} - \tilde{T}^{n+1,m+1}_{1,2} = 0 \quad \text{and} \quad \tilde{T}^{n+1,m+1}_{I,j} - \tilde{T}^{n+1,m+1}_{I-1,j} = \sigma T_s^4 \ . \tag{4.56}$$

We write these in a matrix form $A \cdot T = B$ with

$$A = \begin{pmatrix} -1 & 1 & 0 & 0 & 0 & ... & \\ DL_j(2) & D_j(2) & DU_j(2) & 0 & 0 & ... & \\ 0 & DL_j(3) & D_j(3) & DU_j(3) & 0 & ... & \\ . & . & . & . & . & . & . \\ . & . & . & . & . & -1 & 1 \end{pmatrix} \quad \text{and} \tag{4.57}$$

$$B = \begin{pmatrix} 0 \\ R_j(2) \\ . \\ R_j(i) \\ . \\ R_j(I-1) \\ 0 \end{pmatrix} \tag{4.58}$$

Boundry Conditions Boundary conditions are the same as those for the non-magnetized case, with the exception of the possibilty to add a magnetized envelope model. Figure 3.10 displays two such models, that of [82] (*dotted* lines) show a model with $B = 10^{13}G$ and a variation on this model derived from their own 2D simulations is that of [80] (*dash-dot-dot*). The latter model from [80] was used in the following simulations.

4.4.3. Observational Data

Observational data of thermal luminosities of isolated neutron stars are summarized in Fig. 4.5.

4.4.4. Results

Crust or Core Dominated Poloidal Fields The first consideration is the effect of the poloidal field on the temperature evolution of the star. What would be the effect if, say, the core-centred dipolar field dominated over the crust-confined poloidal field? Would the opposite situation be dramatically different? The lefthand side panels of Fig. 4.6 illustrate the (poloidal) dipolar magnetic field of the crust-dominated case (*upper*: $B_{crust} = 7.5 \cdot 10^{12}$ G & $B_{core} = 2.5 \cdot 10^{12}$ G) and the core-dominated one (*lower*: $B_{crust} = 2.5 \cdot 10^{12}$ G &

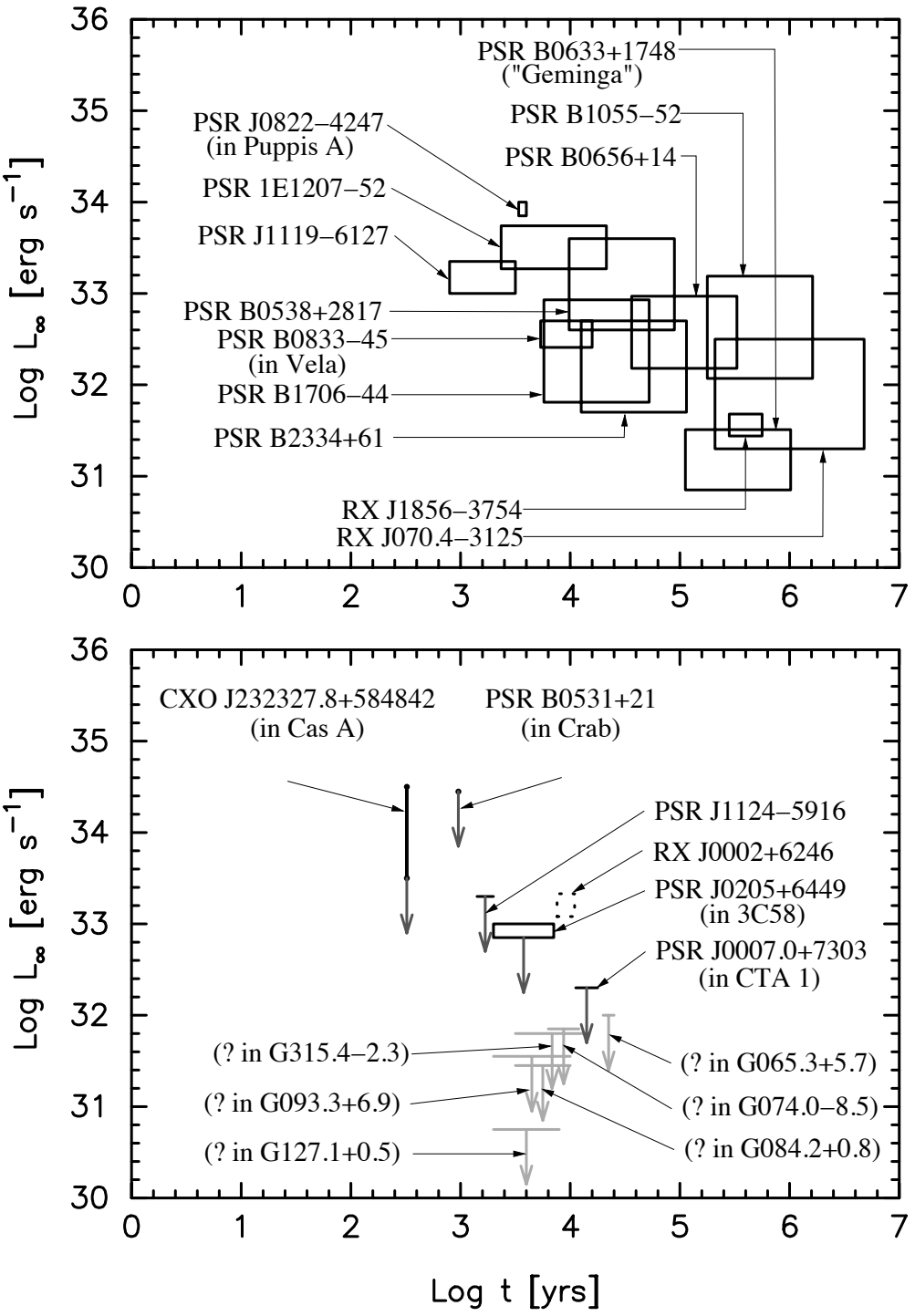

Figure 4.5 Summary of observational data on thermal luminosities of isolated cooling neutron stars. Upper panel: 12 stars for which a thermal spectrum has been clearly detected. Lower panel: the PSR in the nebula 3C58 seems to exhibit a thermal component, and could be presented in the upper panel, whereas in the case of the other objects a thermal component from the main stellar surface is not detected; consequently, the data shown are upper limits on the thermal luminosity. The labels "?" indicate that a compact object has not yet been detected in the supernova remnant. Figure from [74].

$B_{core} = 7.5 \cdot 10^{12}$ G). It can immediately be seen that the crust dominated case concentrates its power deep within the crust where B_θ overpowers. On the other hand, the core-dominated dipole allows for a stronger radial component of the magnetic field, B_r.

The righthand side panels of Fig. 4.6 illustrate the internal temperature profiles of these two model stars from the inner core to the bottom of the envelope (T_b) during their passive cooling phase, at an age $> 10^5$ years. It can be immediately seen that the crust-dominated poloidal field of the upper panels, whose maximum lies deep within the crust, forms what is effectively a "wall" blocking heat flowing perpendicular to it (see the vector field overlayed on the magnetic field profiles of the left hand side panels). The equatorial region in thus cooler at the surface than the two poles, which are between themselves a the same temperature, reflective of the core temperature. In the core-dominated case of the lower panels, the magnetic field is much stronger along the poles where field lines and thus energy flow, are almost purely radial. The temperature at the bottom of the envelope, then, is allowed to be cooler at the poles than the equator. Notice that the temperature at the outer boundary is then converted into a surface temperature through an envelope model: a band around the magnetic equator is then much cooler than the rest of the star due to the high sensitivity of the low density layers to the magnetic field.

The resulting surface temperature evolution are shown in Fig. 4.7. The cooling curves of the two models follow eachother, though the crust-dominated case has a slighly higher T_{eff}, a result of its warmer crust as seen in Fig. 4.6. The unmagnetized star has a higher T_{eff} than the magnetized ones mostly due to its non magnetized envelope which results in a uniform surface temperature.

Strong Toroidal Field & Depth In order to attempt a more complex picture of the internal magnetic field, the following simulation includes a strong toroidal field of maximum intensity 10^{15} G confined entirely to the crust. Fig. 4.8 shows arbitrary combinations of magnetic field Stokes functions with the maximum of the toroidal field at three fraction of the crust thickness: Model A at $0.25r_{crust}$; Model B at $0.5r_{crust}$; and Model C at $0.75r_{crust}$. The poloidal field has a dominant crust-confined poloidal compent at $7.5 \cdot 10^{12}$ G and a core-centered dipole at $2.5 \cdot 10^{12}$ G. The lefthand side panels of the following Fig. 4.9 shows the magnetic field profiles of the three model stars.

Careful inspection of Fig. 4.9 will show that the magnetic field is strongest at the centre of the toroidal field where the component of the field b_ϕ is close to a value of 1 and b_r and b_θ

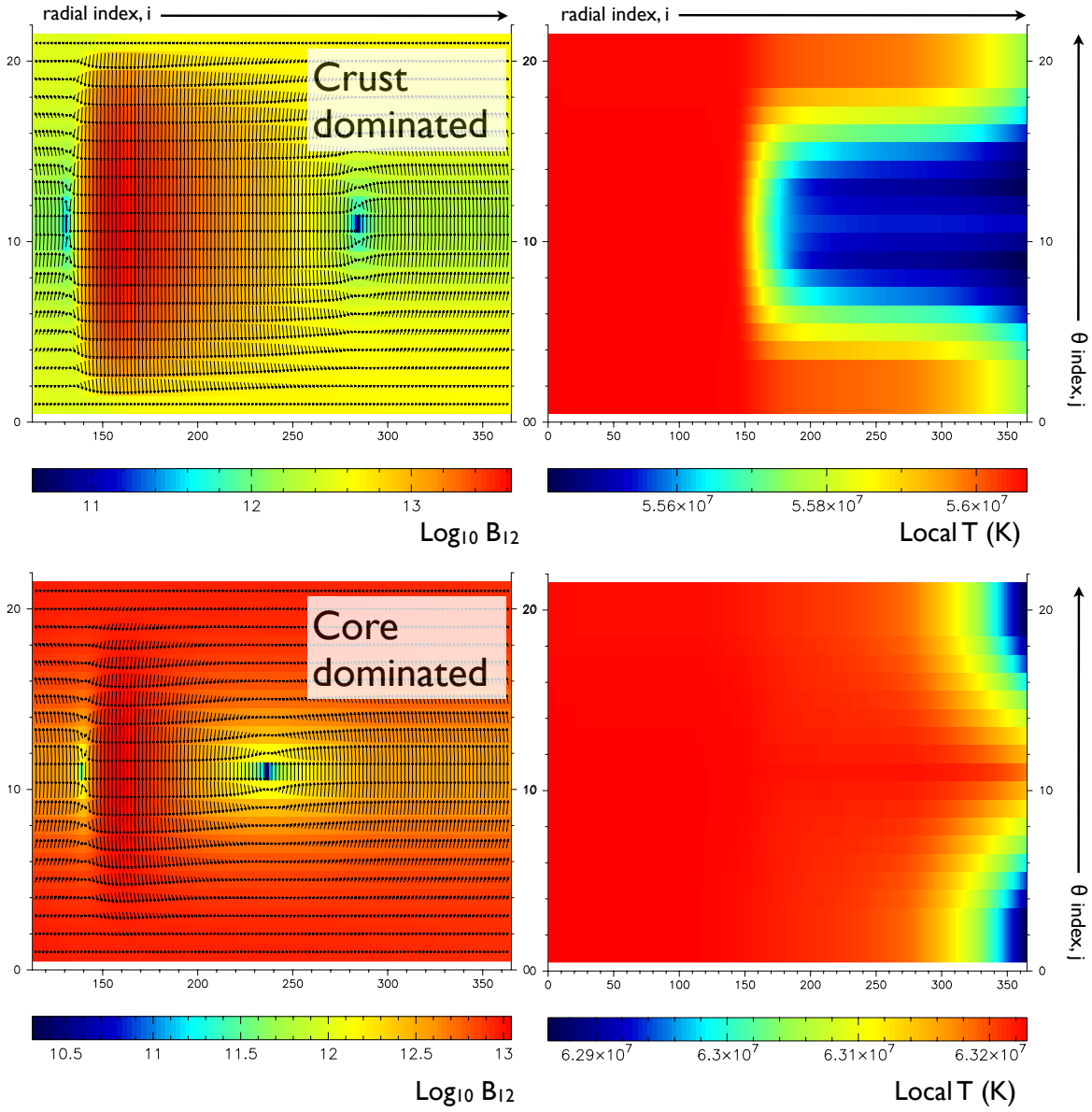

Figure 4.6 Magnetic field (*left*) and temperature (*right*) profiles inside two model stars who differ only in the dominant component of their poloidal fields. The upper model has a crust-dominant poloidal field, and the core-centred dipolar field dominates the lower model star. The magnetic field profiles also show the vector form of the poloidal field (*arrows*). These colour maps are for stars $> 10^5$ years old and vary horizontally by index i along the radius and index j along θ. The crust-core boundary is at index $i = 110$, corresponding to a density $\rho = 1.6 \times 10^{14} g\ cm^{-3}$ and a radus of approximately 10.6 km.

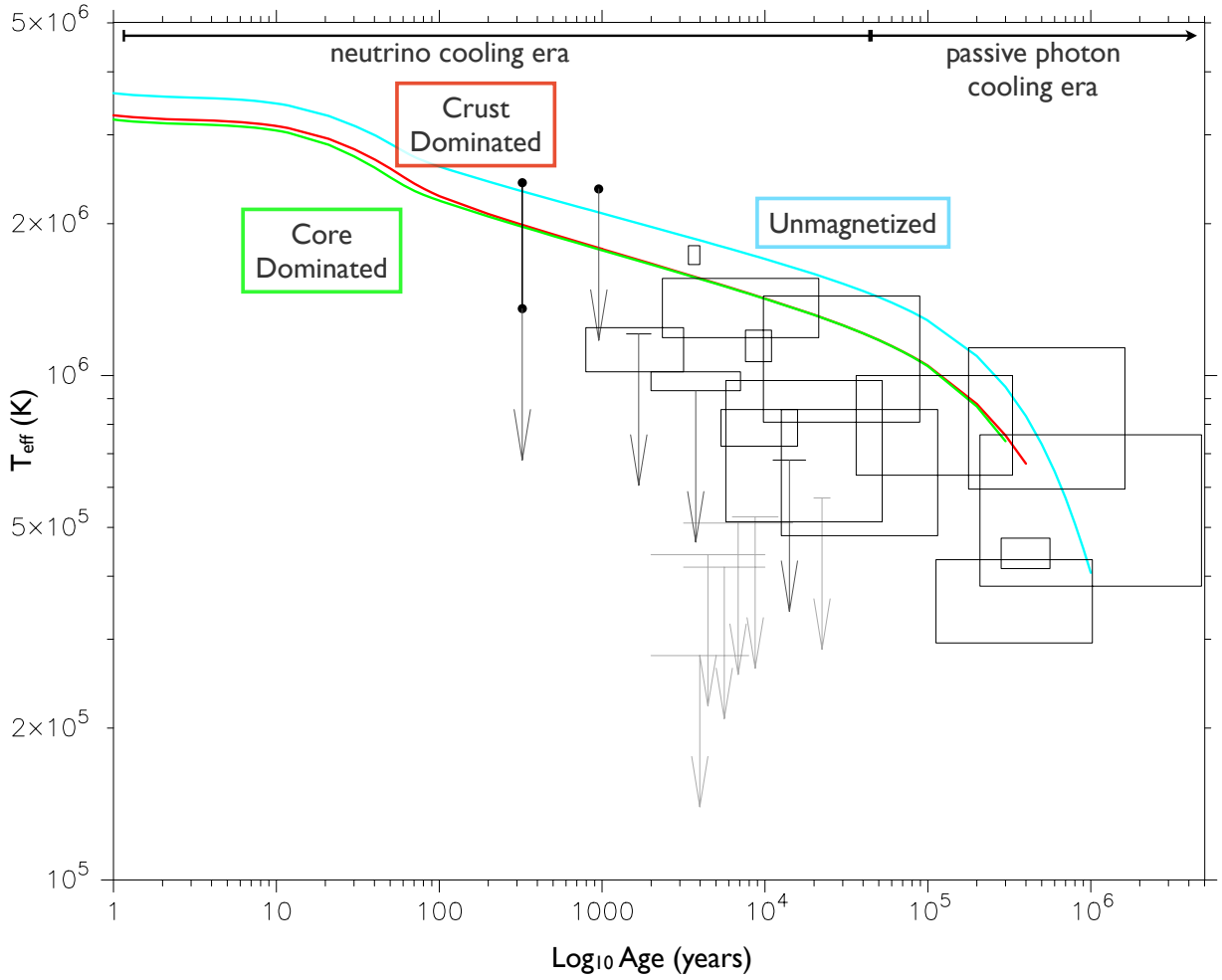

Figure 4.7 The cooling histories of a model star with either a crust and or a core-dominated poloidal magnetic field are not phenomenally different. Data are from Fig. 4.5.

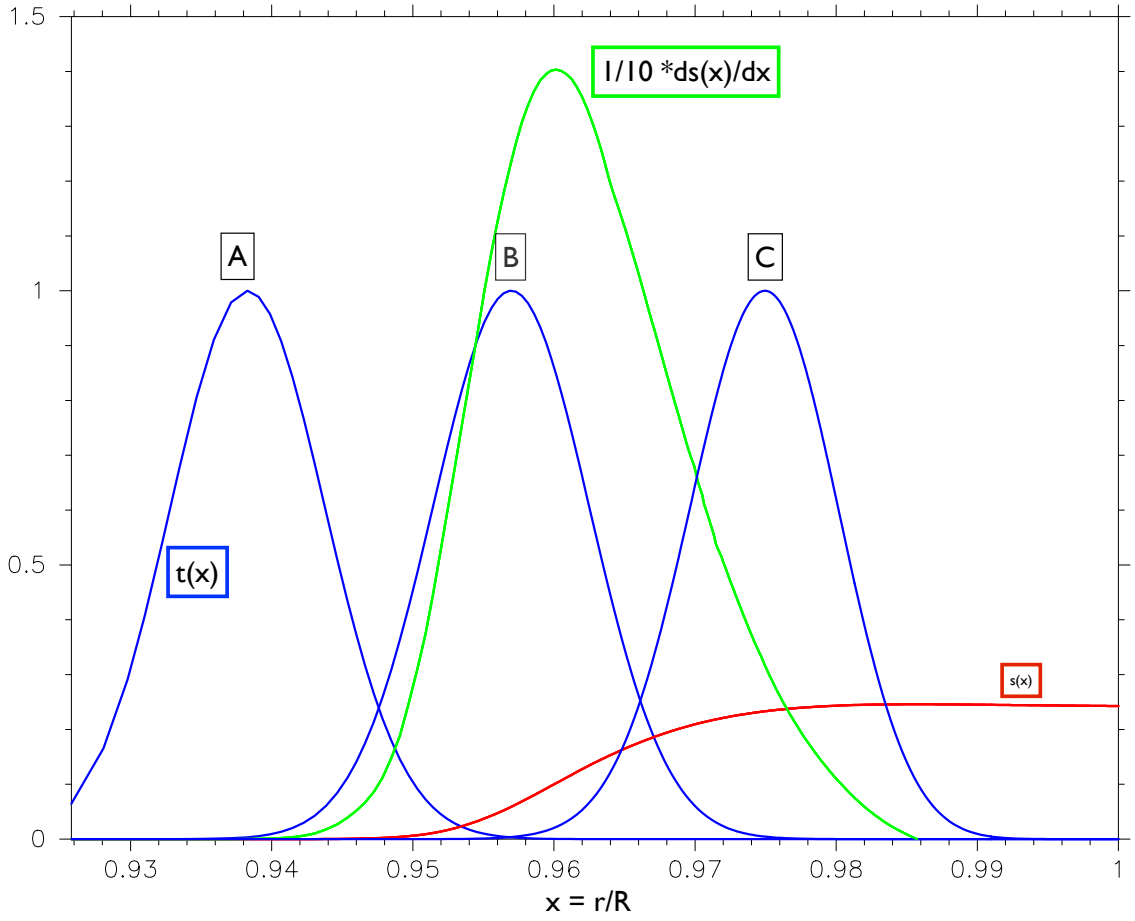

Figure 4.8 Stokes functions used in the construction of a static magnetic field for use inthe neutron star cooling evolution presented here. The function $s(x)$, and its derivative ds/dx, generates the poloidal component, see Eq. (4.25). Three types of toroidal components will be used, models A, B, and C, generated by the Stoke function $t(x)$, Eq. (4.29), which differ by their depth.

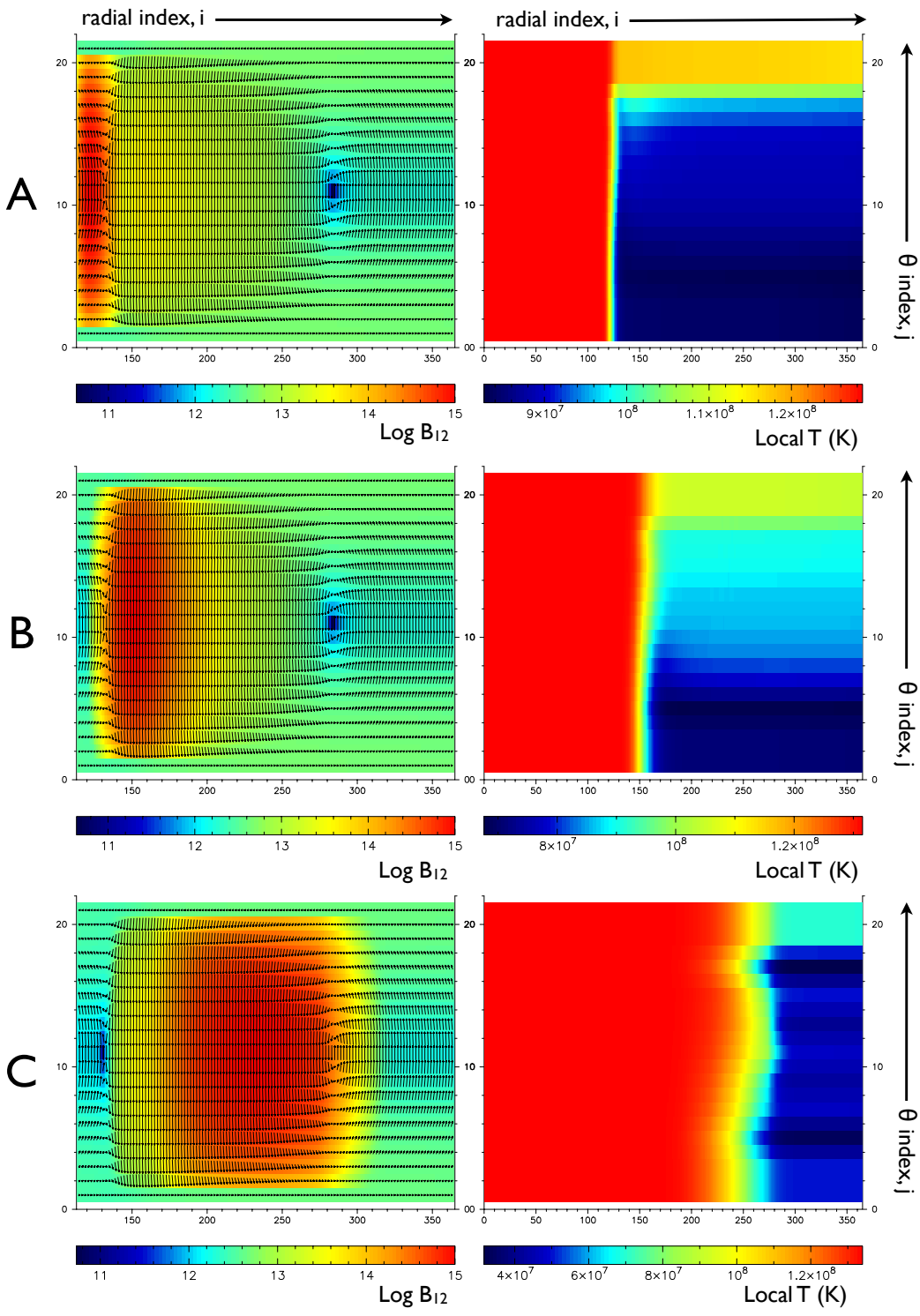

Figure 4.9 Magnetic field (*left*) and temperature (*right*) profiles inside the three model stars from Fig. 4.8 who differ only in the depth of their toroidal fields. The magnetic field profiles also show the vector form of the poloidal field (*arrows*). These colour maps vary horizontally by index i along the radius and index j along θ.

are small. As heat carriers (e.g. electrons) will tend to flow along magnetic field lines, one can imagine that the toroidal field will essentially create a wall blocking heat from escaping near the equatorial regions of the star. The arrows show the direction of the magnetic field in this region. While it would seem that directly along the poles heat should be allowed to flow from the core unhindered, directly off centre heat will be deflected perpendicularly. Recall that the boundary conditions along the poles state that $F_\theta = 0$. In the numerical scheme this is enforced by setting the temperature along the polar grid equal to the grid points immediately nect to it. In this way the poles "feel" the effect of the magnetic field. In the case of a strong toroidal field, this means that heat flow can still be hindered along the poles.

The effect of the toroidal "wall" can be clearly seen in the righthand side panels of Fig. 4.9, which show the internal temperature profiles for the model stars aged to 10^6 years. Notice that in Model A, though the toroidal field (maximum in red) is deep within the crust, the maximum of the crust confined poloidal field lies directly above it (yellow region) and also acts by diverging heat from flowing radially through equatorial regions.

The asymmetrical outcome of the combined poloidal + toroidal fields can also be clearly seen along the pole at $\theta = 0°$. The resulting surface temperature profiles in Fig. 4.10 further illustrate this asymmetry by showing the differing sizes of the warm "hotspot" regions centered on the magnetic poles. Minimum hotspot sizes are necessarily dictated by the resolution of the grid in the numerical method. For the illustrative observational geometry presented, where the observer's line of sight is in the plane of the dipolar field and perpendicular to the rotational axis of the star, the superficial hotspots with cooler equatorial belt can produce a characteristic modulation in received flux. Using a code presented in [69, §4.4], simulated pulsed fractions, PF, are calculated along with blackbody fit spectra in Fig. 4.10. The pulsed fractions are high, over 60%: this issue will be explored in depth in §5.2.

The cooling history of model stars A, B & C are shown in Fig. 4.11, where the dramatic effect of the inclusion of a strong magnetic field and it's matching magnetic envelope can be seen contrasted against the unmagnetized case. In all three cases, the star is "born" with the full magnetic field presented in Fig. 4.9, whose corresponding magnetic envelope is "switched on" during the crust relaxation phase. The initial temperature decrease due to the envelope is fairly dramatic (see envelope models contrasted in Fig. 3.10), though later during the Photon Cooling era the cooling is much softer, possibly due to the toroidal wall diverting radiative heat flow along the poles.

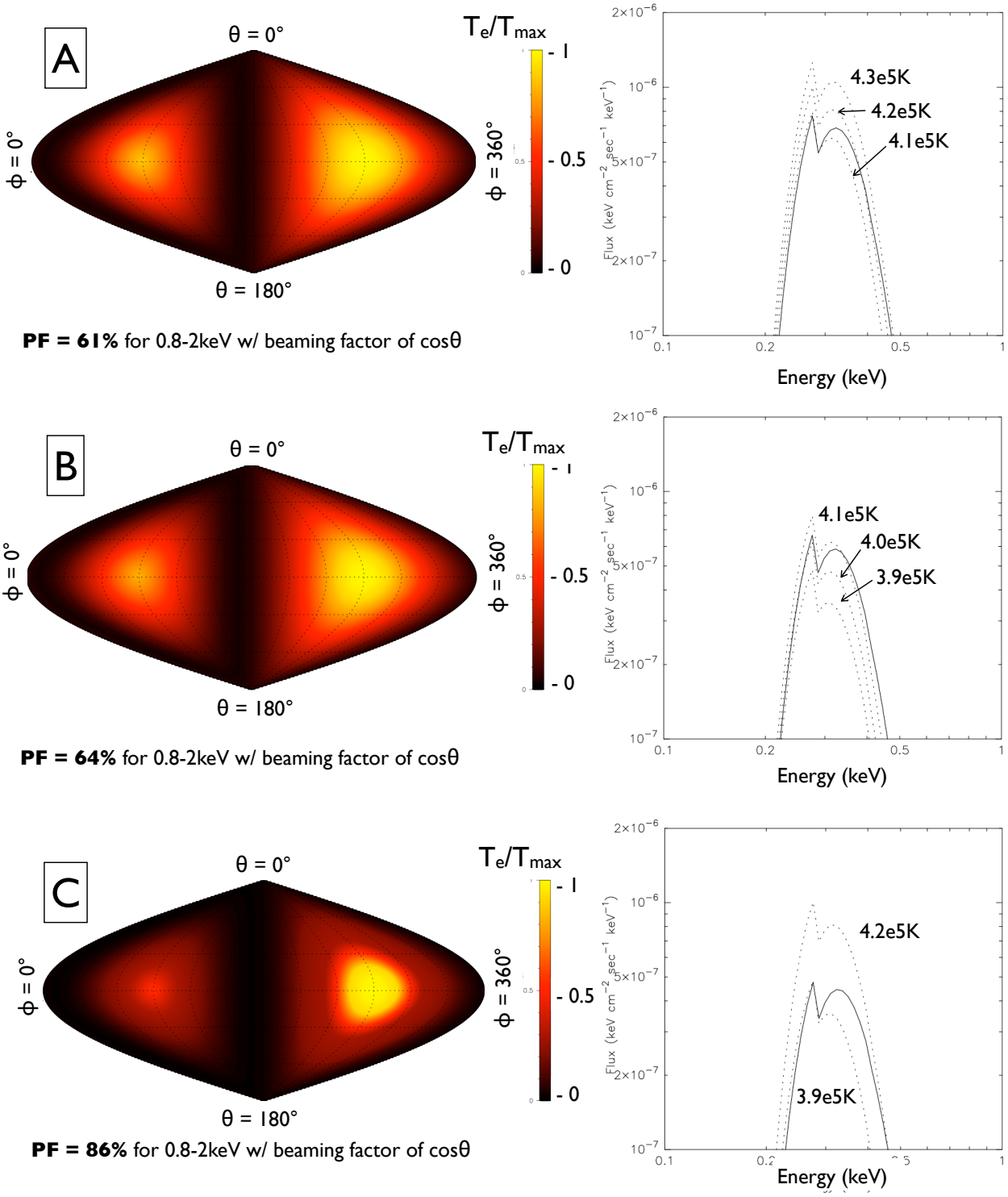

Figure 4.10 Surface temperature maps (*left*) and recieved spectra (*right*) for the model stars of Fig. 4.9, presented in using the code described in [69, §4.4]. For illustrative purposes, the observer is placed in the plane of the magnetic field which is then perpendicular to the stars rotational axis. The resulting Pulse Fractions, *PF*, are stated below.

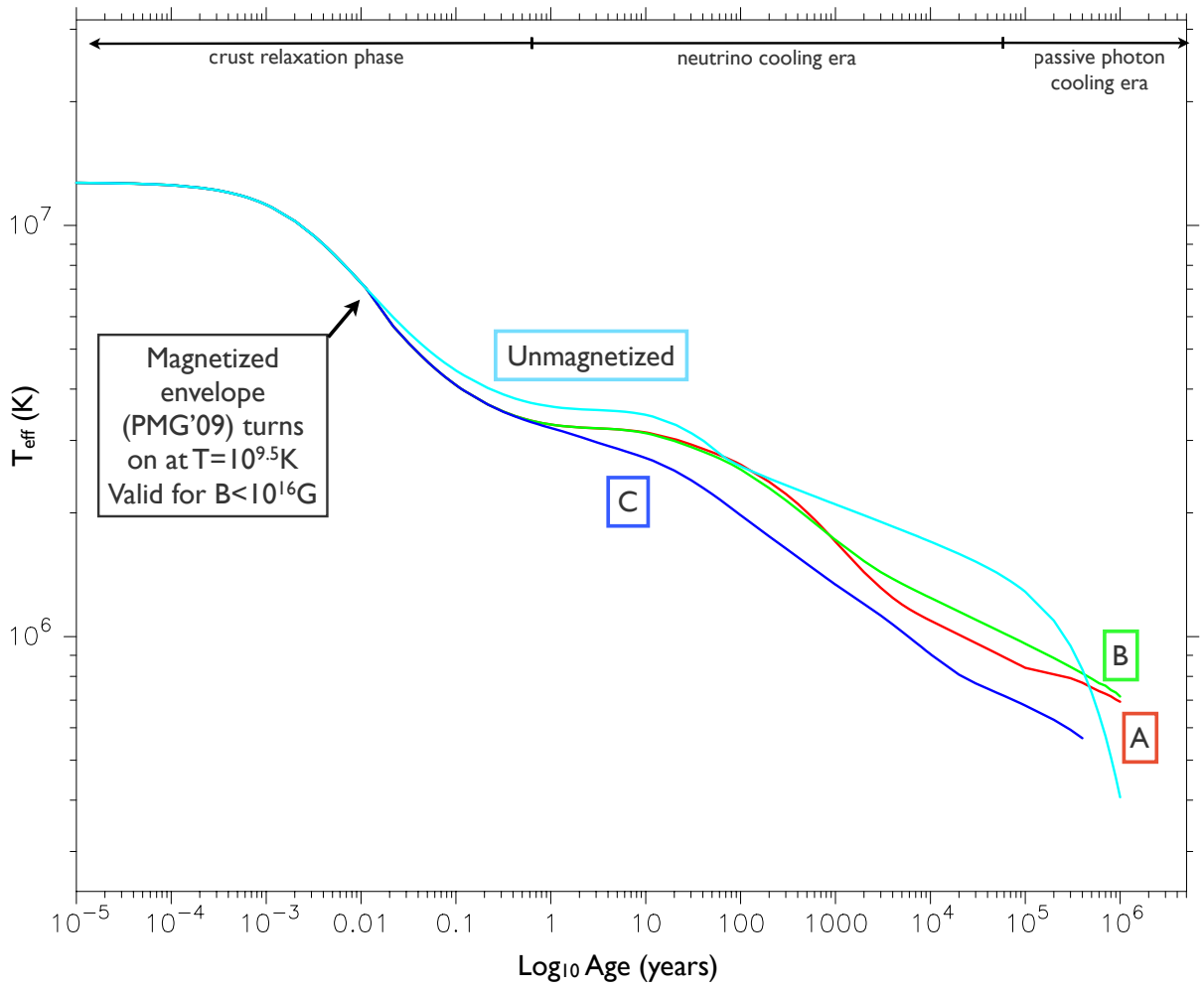

Figure 4.11 Cooling curves of the model stars in Fig. 4.9 contrasted with the unmagnetized case (*turquoise*).

Fast vs. Slow Magnetic Fields It was mentioned above that the model stars so far considered were "born" with their magnetic fields in place and that their strength and configuration never change. This is, of course, far from the realistic assumption that the magnetic field would actually evolve along with the star and increase or decrease in stength during its lifetime. As a first step, the effect of slowly increasing the magnetic field strength during the star's lifetime is considered. Fig. 4.12 shows the Model B star shown previously (*red curve*) contrasted with its slow cousin, (*green curve*) and the unmagnetized star (*blue curve*). The strength of the total magnetic field of the slow star is regulated by letting it reach its maximum at an age of $3 \cdot 10^5$ years. At this point in time you can see how it eventually matches the cooling of the fast star. Previous to which, the shape at least of the slow star matched the unmagnetized case, though the same magnetized envelope was applied since the beginning and served to still lower its overall effective temperature over time. If nothing else, it illustrates that even the simplest magnetic field evolution scenario can have an effect. A realistic field evolution scenario would involve solving the magnetohydrodynamic (MHD) equation for the magnetic field simultaneously with the thermal evolution. This is a formidable task which we leave for future work.

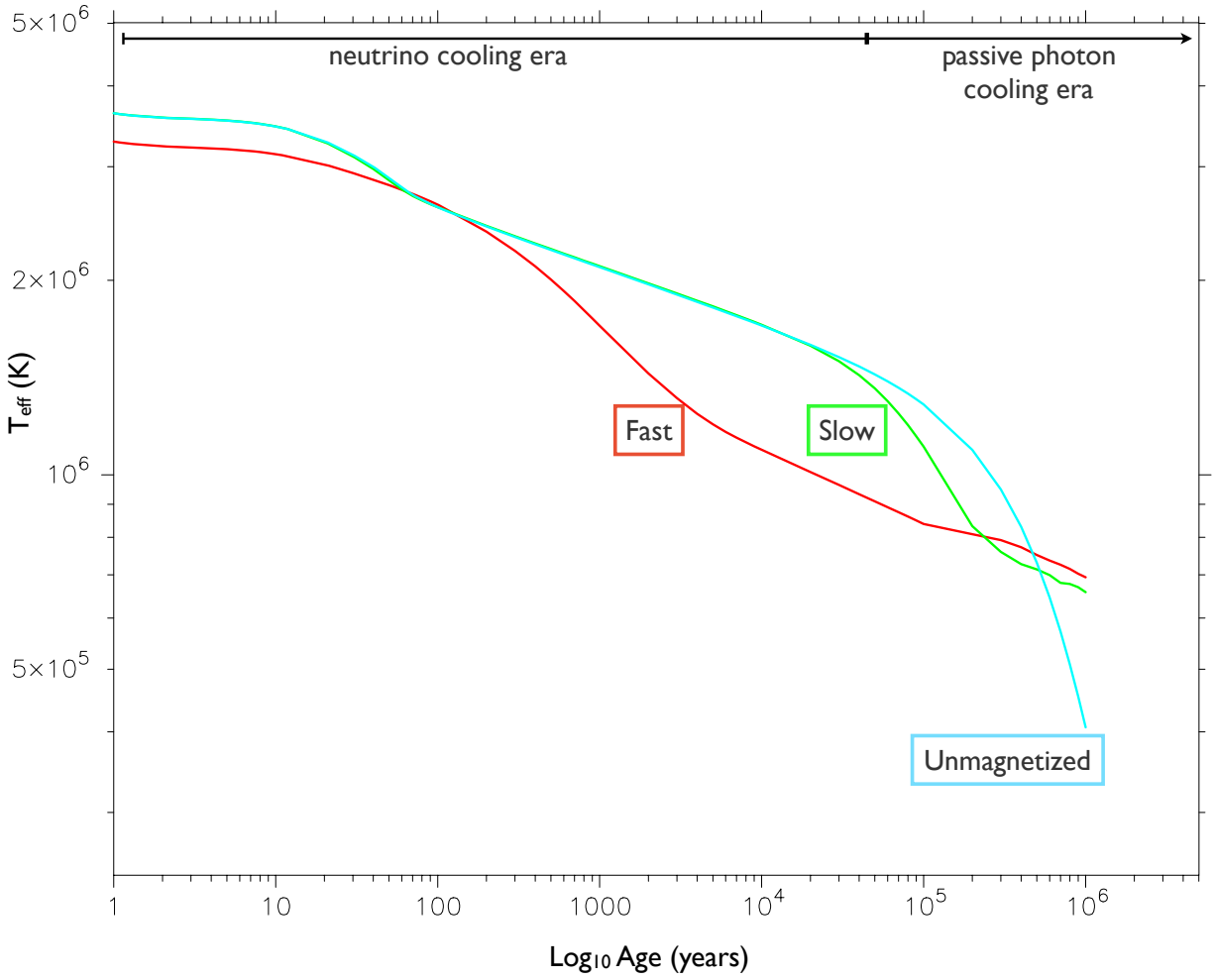

Figure 4.12 Cooling curve of Model B stars with fast magnetic field evolution (*red*, i.e. the star is "born" with a strong B essentially in place), and a slow evolution (*green*, the stregth of the total field, B, reaches its maximum at $3 \cdot 10^5 years$.).

Chapter 5

Case Studies

5.1. Magnetic Heating and Core Superfluidity

So far we have neglected the the term Q_h from Equation (3.13): heat sources within the star. In magnetic neutron stars, magnetic field decay could be one such source of energy [1].

In the core, it would have to compete with the efficiency of neutrino cooling, but could be important since it could influence when superfluidity actually occurs [24]. This in turn would affect various associated phenmena, such as glitches (see §3.2.1). The problem was addressed by Ho et al (2012)[50] who performed detailed one-dimensional simulations to check if the decay of a strong core-centered dipolar field of $10^{16}G$ could keep core temperatures high enough to delay the onset of superfluidity. They found that heat generated from field decay was not strong enough to overwhelm neutrino cooling. Here, we confirm their analysis by performig a similar calculation but with two dimensional cooling with the addition of a magnetized envelope of Pons et al (2009)[80].

The heating term, q_h is calculated by considering magnetic field decay due to bipolar diffusion [40] and is given by,

$$q_h \approx \frac{B}{4\pi}\frac{dB}{dt} \approx \frac{B^2}{4\pi\tau^{amb}} \tag{5.1}$$

$$= 1 \cdot 10^{20}\,\mathrm{ergs\,cm^{-3}\,s^{-1}} \times \left(\frac{\rho}{\rho_{nucl}}\right)^{-2/3}\left(\frac{T}{10^9\,\mathrm{K}}\right)^{-2}\left(\frac{B}{10^{16}\,\mathrm{G}}\right)^{4} \tag{5.2}$$

where the the ambipolar diffusion timescale, τ^{amb} is controlled by particle collisions in neutron

star matter. From it's form you can note that it operates at high T,

$$\tau^{amb} \sim 2.5 \cdot 10^3 \,\mathrm{yrs} \left(\frac{L}{1\,\mathrm{km}}\right)^2 \left(\frac{\rho}{\rho_{nucl}}\right)^{2/3} \left(\frac{T}{10^9\,\mathrm{K}}\right)^2 \left(\frac{B}{10^{16}\,\mathrm{G}}\right)^4 \tag{5.3}$$

Finally, the actual decay of the magnetic field is given by the following simple formula,

$$B(t) = \frac{B_o}{1 + t/\tau_{decay}} \tag{5.4}$$

whose justification lies in the fact that it has a similar form to that found in the literature (for example Dall'Osso (2009)[24] and of course the model paper from Ho et al (2012)[50]) and results can thus be compared. The decay timescale, τ_{decay}, is taken to be 10^4 yrs. Magnetic field decay in times less than 10^4 yrs is not yet well understood or even guaranteed to occur [40].

Figure 5.1 shows the 2D cooling calculation of a star similar to the one in Ho et al (2012)[50]) with T_c for neutron $^1S_0$ from Wambach et al (1993)[106] and proton $^1S_0$ from Chen et al (1993)[22]. The neutron $^3P_2$ channel for a *deep* appearance of the gap, however, is from Elgarøy et al (1996)[25].

Figure 5.2 has the simulated B-decay heating added in the core. Along the right-hand axis are approximate ages, Log(t/years), labels and when compared to the case without heating (Figure 5.1), it is clear that onset of the neutron $^3P_2$ Gap is delayed by $\sim$ 1000 years.

However, the above equation for τ^{amb} is for the *solenoidal* mode only. The transition to the non-solenoidal mode at lower temperatures from beta chemical equilibrium should be taken into account and occurs at $\tau^{tr} = 7 \cdot 10^8$ K. Proton superconductivity occurs before this at $\sim (2-3) \cdot 10^9$ K [75]. The conversion to superconducting protons would suppress beta equilibrium, thus changing τ^{amb} and the heating rate of Equation (5.1). It was found by Ho et al (2012)[50]) that taking this into account results in no delayed onset of proton superfluidity in the core from magnetic field decay, and cooling occurs much as in the case without the additional core heating.

Kaminker et al (2006)[57] proposed that in order to keep a neutron star hot enough to reach the T_{eff} of Magnetars, additional heating (q_h) must come from a heat source in the outer crust, where it would not be overwhelmed by neutrino cooling. Ho et al (2012)[50]) confirmed these results and here we perform the same analysis but with the two-dimensional calculation and the addition of a magnetized envelope.

The q_h term for the crust is given by a phenomenological model given in Kaminker et al (2009)[56] and Ho et al (2012)[50] rather than a detailed analysis of physical processes that may be occurring (such as presented in Pons et al (2009)[80]). The exact nature of the added energy is not important for the purposes of this model, rather the fact that it must be present in order to account for the high T_{eff} of magnetars. q_h is given thus,

$$q_h = q_o \exp\Big\{ - \big[(\rho - \rho_h)/\Delta_h\big]^2 \Big\} \exp\Big(- t/\tau_h \Big) \tag{5.5}$$

where $q_o = 3 \cdot 10^{20}$ ergs cm^{-3}, $\rho_h = 6 \cdot 10^{10}$ g cm^{-3}, $\Delta_h = 1 \cdot 10^{10}$ g cm^{-3}, and $\tau_h = 10^4$ yrs. The timescale during which the crust will maintain a high temperature, τ_h, is chosen such that it approximates the age of the oldest magnetar.

Figure 5.3 shows a simulation with the above crustal heating scheme placed within. It is clear that a high surface temperature will be maintained until the expected timescale, $\tau_h = 10^4$ years and $\tau_h = 10^5$ years. Note that the pairing channels are distinct from 5.1 (see Figure 4.3), but do not affect the T_s for the purposes of this particular simulation.

The cooling curves for the crustal heating models are plotted in Figure 5.4. Without any added heating mechanism the star shows what we would expect for a neutron star (*turquoise line*). With the addition of core heating T_s would actualy be maintained longer as can be seen in it's profile from Figure5.2: the star reaches isothermality with the core then decreases with it. The addition of the magnetized envelope from Pons et al (2009)[80] aids in keeping T from leaking, particularly for such a high magnetic field ($10^{16}G$). However, as found by Ho et al (2012)[50], only with the addition of crustal heating near the surface (*red and green lines*) can the possibility of maintaining a high T_s long enough to reach Magnetar temperature be kept alive.

5.2. Light Curves and Large Pulse Fractions

Although most pulsars have derived B values below the quantum critical value of $4.4 \cdot 10^{13}G$, there are a small number of objects with B fields near or above this QED value, some of which are still detected in the radio, otherwise known as High-Magnetic Field Pulsars (HBPSRs).

First Detected in the Parkes Multibeam Survey [18], PSR J1119-6127 is one such object with a spin-down inferred B of $4.1 \cdot 10^{13}$ G, one of the highest magnetic fields measured for a pulsar. Later detected in x-rays by Gonzalez et al (2005) [41] with XMM-Newton, this star

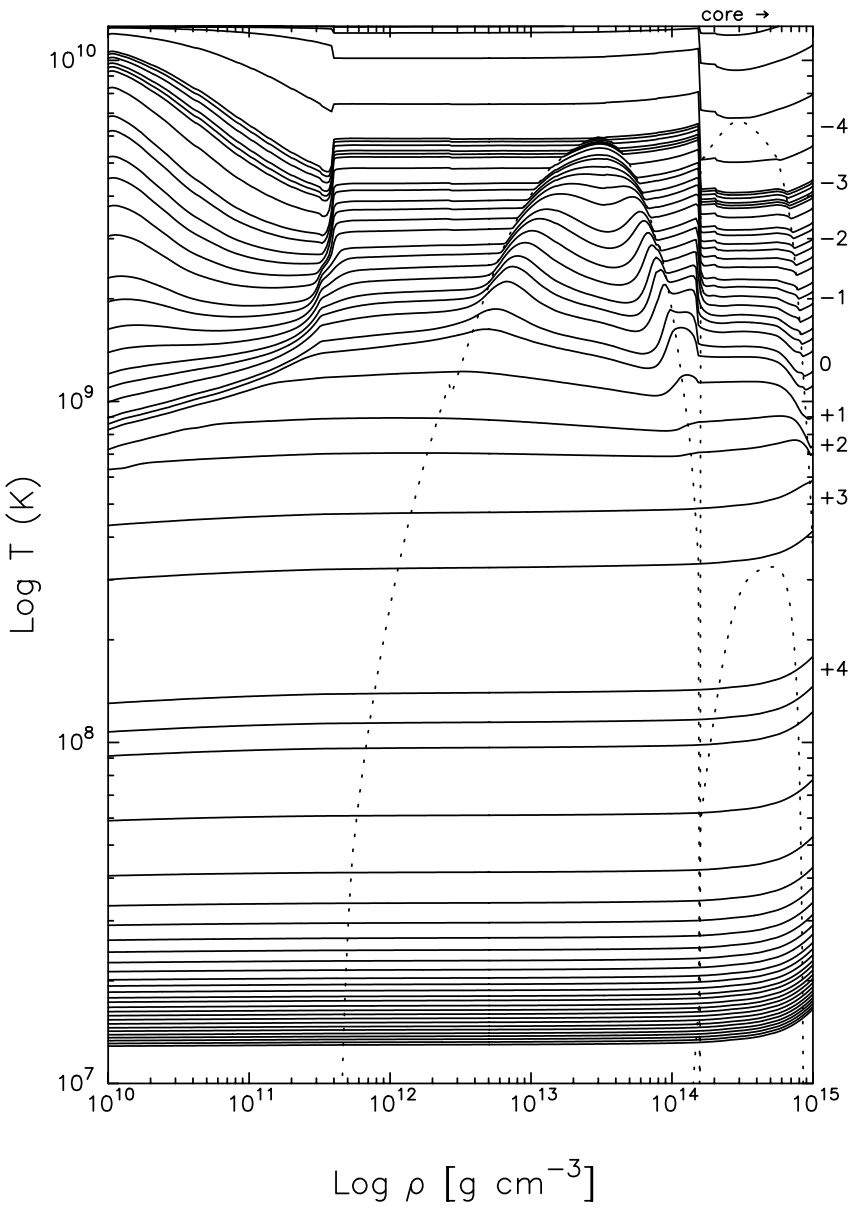

Figure 5.1 Internal temperature profile as a function of stellar age for a model without any additional heating terms. Superfluid critical temperatures T_c for the processes outlined in §3.3.2 are added for comparison (*dotted* curves): neutron $^1S_0$ from [106] (left); proton $^1S_0$ from [22] (top); and neutron $^3P_2$ from [25] (bottom). Age is marked along the right-hand axis as $Log(years)$.

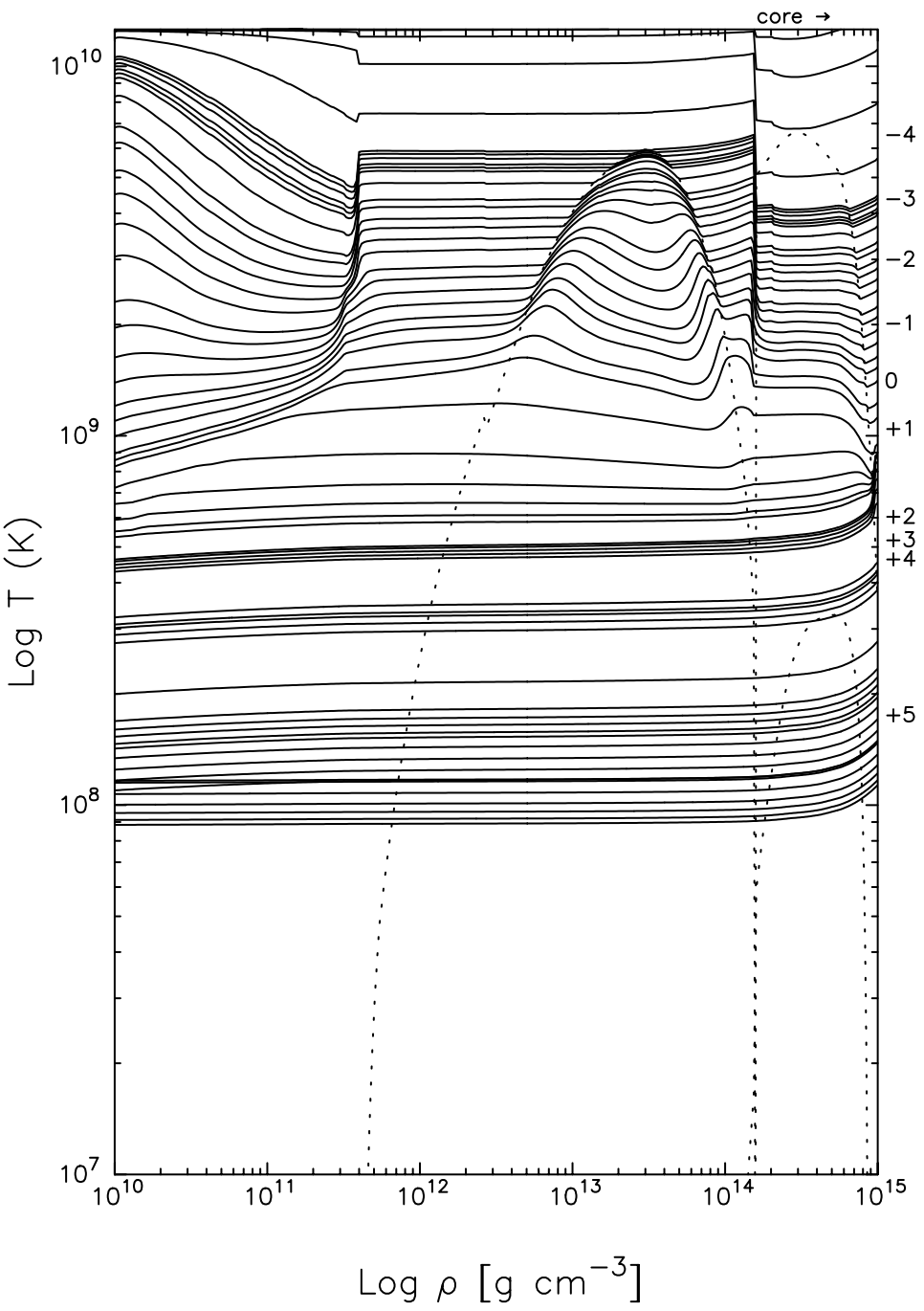

Figure 5.2 Internal temperature profile as a function of stellar age for a model with heating from magnetic field decay in the core. Superfluid critical temperatures T_c for the processes outlined in §3.3.2 are added for comparison (*dotted* curves): neutron $^1S_0$ from [106] (left); proton $^1S_0$ from [22] (top); and neutron $^3P_2$ from [25] (bottom). Age is marked along the right-hand axis as $Log(years)$. Note that when compared to the case for no heating (see Figure 5.1 the onset of neutron $^3P_2$ superfluidity has been delayed.

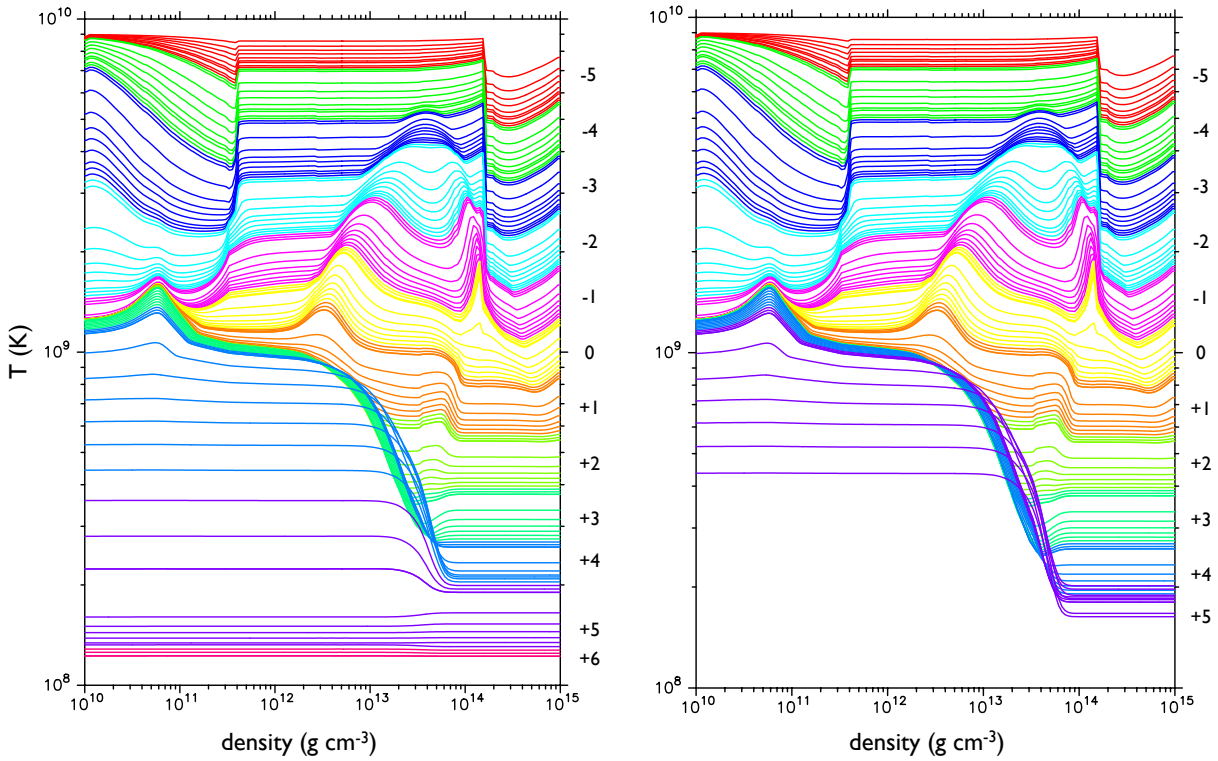

Figure 5.3 Internal temperature profile as a function of stellar age for a model with heating in the crust. Age is marked along the right-hand axis as $Log(years)$. Note that when compared to the case for no heating (see Figure 5.1 the temperature in the outer crust remains essentially isothermal for thousands of years and is expected to do so for the timescale of the input heating model (*Left:* $\tau_h = 10^4 yrs$ and *Right:* $\tau_h = 10^5 yrs$). The pairing channels are distinct from 5.1 (see Figure 4.3), but do not affect the T_s for the purposes of this particular simulation.

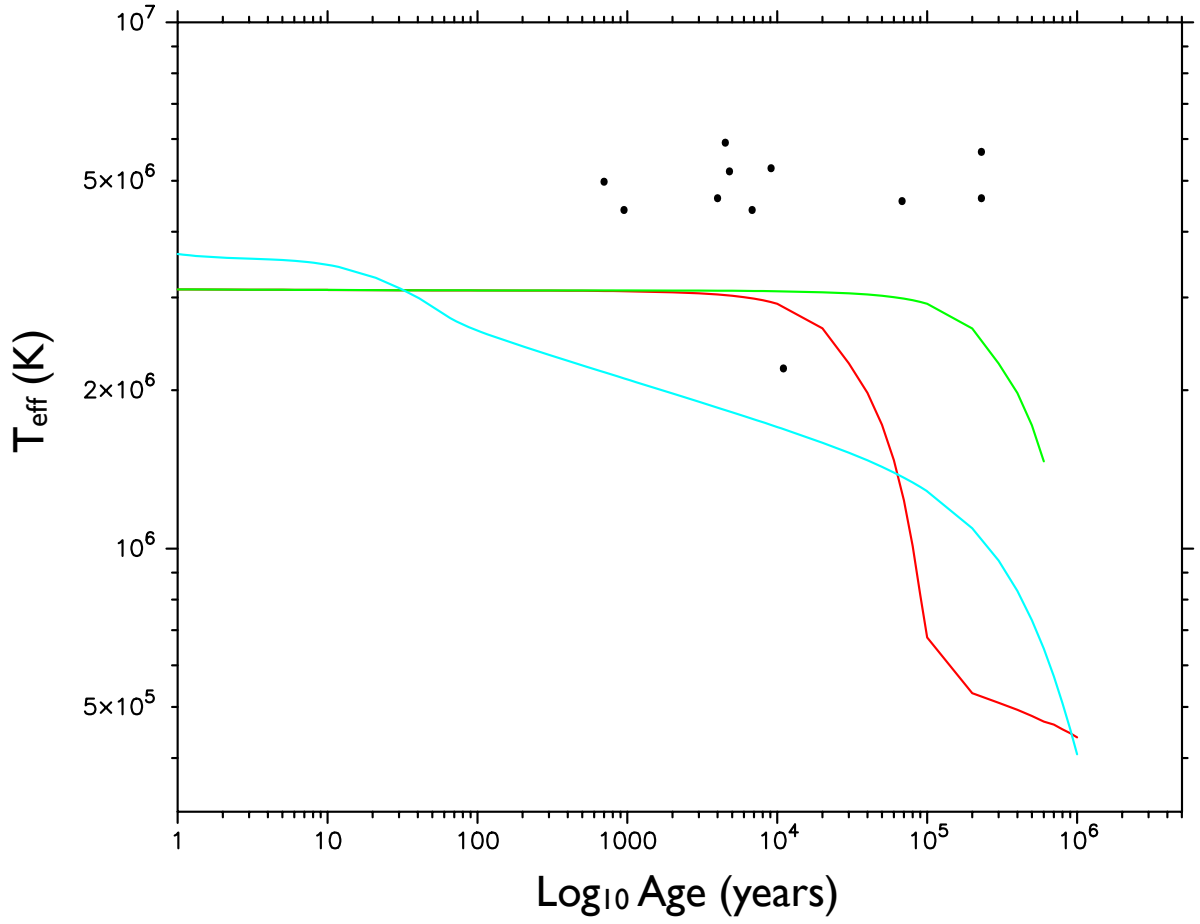

Figure 5.4 Cooling curves for the models presented in Figures 5.1 (*turquoise line*) and 5.3 (*red curve for* $\tau_h = 10^4$ *years and green for* $\tau_h = 10^5$ *years*). Approximate ages and Black Body temperatures for the Magnetars from Table 3.3 are plotted for comparison. It is evident that some sort of crustal heating is most likely necessary in order to reach Magnetar temperatures.

showed pulsed emission in soft x-rays ($0.5 - 2.0$ keV) with a very high pulsed fraction (PF) of $74 \pm 14\%$. It's spectra in the $0.5 - 10.0$ keV range was best fit by a blackbody in soft, low energy x-rays plus a power law for the hard, high energy x-ray emission, implying that the lower energy pulsed emission is thermal in origin, most likely from the stellar surface either due to initial cooling evolution of the star or reheated polar caps by magnetospheric processes.

It is the view in this project that the most reasonable scenario is that non-uniform surface temperature distributions from cooling resulting in the presence of superficial hot-spots centered upon the magnetic dipole axis surrounded by a cooler equatorial belt are responsible for the pulsed thermal soft x-ray emission. Previous cooling calculations have shown that the presence of a strong toroidal field in the crust can produce such a scenario and does result in detectable pulsed emission ([78], [33], §4.4 of this text).

It is the purpose of this section to explore the effect on pulsed emission of hot spot configuration, ultimately due to magnetic field configuration, along with other important effects on radiation emission, such as an angular dependance on $\vec{B}$ and gravitational light bending. The theory of this influence on radiated emission is discussed below followed by a description of the numerical model used to simulated the effects as well as their results. The particular case of PSR J1119-6127 and related objects is examined.

The strong gravitational field of a compact star causes a lensing effect: that is, a photon emitted at an angle α with respect to the radial direction will have it's trajectory bent to an angle $\psi > \alpha$. The result being that an observer at infinity will be able to see more than half of the stellar surface (see Fig. 5.5).

The effect is quantified in a simple and elegant analytical form from Beloborodov (2002)[15]. In this work a relationship between observed pulsed fraction and stellar size in a Schwarzschild metric is developed, valid for radii $R \geqslant r_g$ where $r_g = 2GM/c^2$ is the gravitational radius.

Beloborodov [15] considers a pulsar with two antipodal point-like "hotspots" (spot diameter $< 10^\circ$), presumably produced by the presence of a dipolar magnetic field whose axis is at an angle $\theta \leqslant 90^\circ$ with the rotation axis of the star (see figure 5.5). The normal pointing towards the observer is denoted by $\mathbf{d}$ and the angle between $\mathbf{d}$ and the rotation axis is i. The spot closest to the observer is designated as "primary" with normal $\mathbf{n}$ and inclination $\mu = \mathbf{n} \cdot \mathbf{d}$. The antipodal spot then has normal $\bar{\mathbf{n}}$ and inclination $\bar{\mu} = \bar{\mathbf{n}} \cdot \mathbf{d}$. The spot inclinations will vary in time, $\mu = \mu(t)$, between $\mu_{min} = \cos(i + \theta)$ and $\mu_{max} = \cos(i - \theta)$. The visible part of the star is defined by a circle $\mu = \cos\psi$. In a flat spacetime $\mu > 0$, but

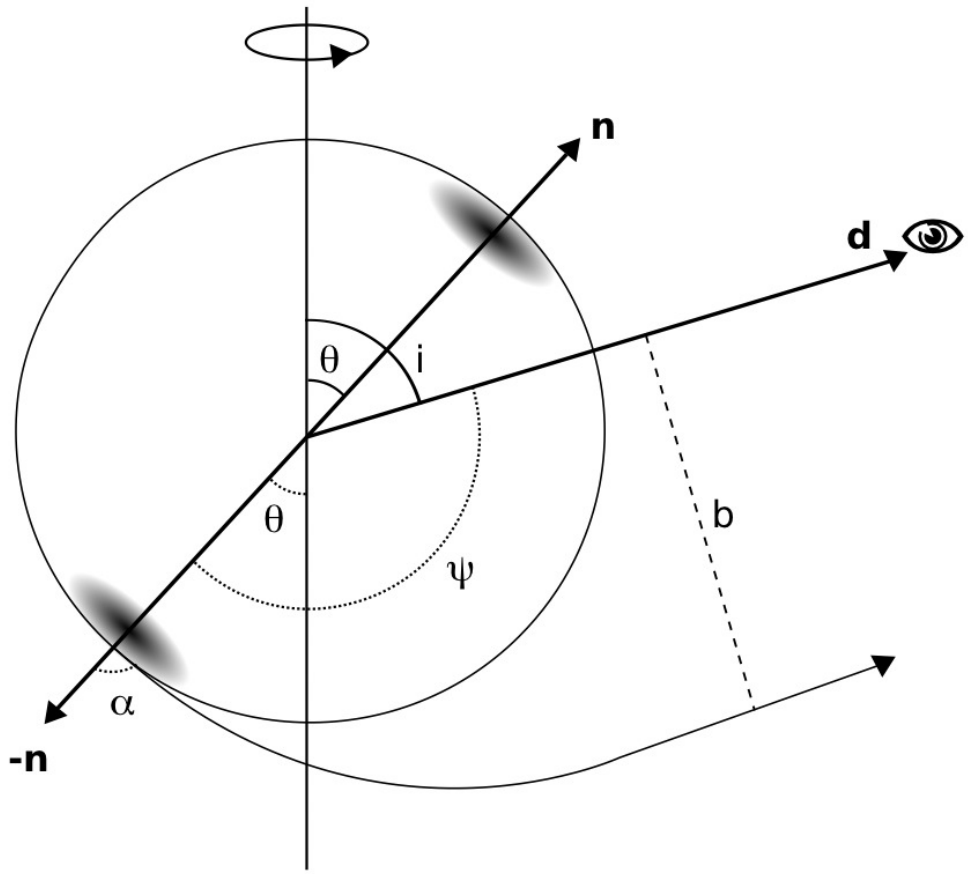

Figure 5.5 Effect of gravity on light emitted near a compact star. Here, a photon emitted from the antipodal spot at an angle α with respect to the radial direction escapes to infinity at an angle ψ and impact parameter b.

in a curved spacetime μ can be negative up to a maximum μ_v at which point photons are emitted tangentially to the stellar surface.

Using the following approximation in a Schwarzschild spacetime,

$$1 - \cos\alpha = (1 - \cos\psi)\left(1 - \frac{r_g}{R}\right) \tag{5.6}$$

the observed flux, dF, from a visible area, dS, is given by,

$$dF = \left(1 - \frac{r_g}{R}\right)^2 I_o(\alpha)\cos\alpha\frac{dS}{D^2} \tag{5.7}$$

where $I_o(\alpha)$ is the surface radiation intensity seen by an observer at distance $D \gg R$. Using a point-like spot approximation, the flux from a spot of area s viewed directly would be $F_1 = (1 - r_g/R)^2 I_o s/D^2$ and the observed fluxes from the primary, F, and antipodal, $\bar{F}$, spots as the star rotates would be,

$$\frac{F}{F_1} = \mu\left(1 - \frac{r_g}{R}\right) + \frac{r_g}{R}, \qquad \frac{\bar{F}}{F_1} = -\mu\left(1 - \frac{r_g}{R}\right) + \frac{r_g}{R} \tag{5.8}$$

The primary spot is seen when $\mu > \mu_v$ and the antipodal spot is seen when $\bar{\mu} > \mu_v$ (from equation 5.6, $\mu_v = -r_g/(R - r_g)$). Both spots should be seen when $\mu_v < \mu < -\mu_v$ at which point the observed flux, F_{obs}, will be constant.

Depending on the initial configuration of spot and observer angle, (θ, i), the observed light curves can be generally divided into four classes [15, Figures 3,4]. *Class I* describes a "perfect" sinusoidal light curve produced when the primary spot is viewed at all times and the antipodal spot is never seen ($\mu_{min} > -\mu_v$). *Class II* describes a situation where the primary spot is always seen and the antipodal spot appears occasionally, at which point both spots are seen and $F_{obs} = constant$. The characteristic light curve for this scenario is a sinusoidal profile interrupted by a plateau between the peaks ($\mu_v < \mu_{min} < -\mu_v < \mu_{max}$). *Class III* pulsed profiles are characterized by a main sinusoid from the primary spot interrupted by a plateau which is in turn interrupted by a sinusoid with smaller amplitude from the antipodal spot. In this situation, whenever the primary is not seen, the antipodal spot is ($\mu_{min} < \mu_v$). The final *Class IV* is produced by a configuration in which both spots are seen at all times and the resulting light curve is constant ($\mu_v < \mu_{min},\ \mu_{max} < -\mu_v$).

The corresponding PF's defined by $PF = (F_{max} - F_{min})/(F_{max} + F_{min})$ for all classes

are given by,

$$PF = \left\{ \begin{array}{ll} \frac{(\mu_{max}-\mu_{min})}{(\mu_{max}+\mu_{min}-2\mu_v)} & Class\ I \\ \\ \frac{(\mu_{max}+\mu_v)}{(\mu_{max}-3\mu_v)} & Class\ II, III \\ \\ 0 & Class\ IV \end{array} \right\} \tag{5.9}$$

If $\mu_{max} = 1$ and $\mu_{min} < -\mu_v$ then $PF_{max} = (R - 2r_g)/(R + 2r_g)$.

Magnetic field effects In order to include possible effects from magnetic field orientation on photon trajectories (i.e. "beaming") in the above equations a beaming factor, BF, was added to equation 5.7 to refine the photon emission in the following way,

$$dF = \left(1 - \frac{r_g}{R}\right)^2 I_o(\alpha)(\cos\alpha)^{BF+1}\frac{dS}{D^2} \tag{5.10}$$

which has the corresponding effect on μ_v and PF_{max} (see equation 5.6),

$$\mu_v \longrightarrow \frac{-(r_g/R)^{BF+1}}{1-(r_g/R)^{BF+1}}$$

$$PF_{max} \longrightarrow \frac{1-2(r_g/R)^{BF+1}}{1+2(r_g/R)^{BF+1}}$$

In this study, BF's of $0, 1, 2$ were considered.

Numerical Model and Results

Antipodal hot spots For the purpose of this investigation, model stars were produced by setting antipodal hotspots of varying diameter and constant temperature ($T_{sp} = 5 \cdot 10^6 K$) at specific angles, θ, with respect to the rotation axis. The rest of the surface of the star was kept at a constant $T_{main} = 10^5 K$ (see figure 2) and the star was "rotated" to produce model light curves for each configuration of spot and observer angles $(\theta, i) = (45°, 45°), (30°, 60°), (60°, 80°)$, spot diameter ($diam = 10°, 30°, 50°$), stellar size ($2 \leqslant R/r_g \geqslant 4$) and beaming factor ($BF = 0, 1, 2$). In this simulation a distance of 100 pc and $N_H = 10^{20} cm^{-2}$ was used. Variation of these parameters would have an effect on observed intensity and spectra but not necessarily on PF amplitudes. A mass of $1.4 M_\odot$ was used, but again, while varying the mass will change the R for a particular PF, it has no effect on PF $vs.$ R/r_g. Virtual observations were made in the energy range $0.5 - 2$ keV, representing the majority

of the pulsed emission. A more in-depth description of the code used to produce the model data can be found in [69, §4.4]. *Note*: As seen in Fig. 5.6, as long as T_{sp} is about an order of magnitude greater than T_{main}, temperature does not play a significant role in determining the amplitude of observed pulse fractions.

The results of PF *vs.* R/r_g are plotted in Fig. 5.7 where each panel represents a different (θ, i) configuration. Three sets of curves become distinctly separated in each plot corresponding to different BF's, where PF increases with increasing beaming, as intuition may dictate. Two "theoretical" curves are also plotted for each BF, the higher one corresponding to the maximum PF_{max}, and the lower corresponding to the PF of equation 5.9, which depends on the (θ, i) configuration. Perhaps also intuitively, PF decreases for increasing spot size, represented by the three descending curves for each BF. *Note*: The apparent plateau in the PF *vs.* R/r_g curves for zero beaming at small radii is an effect of numerical noise from the model resulting from an effort to keep angular resolution computationally reasonable and should be ignored.

Non-antipodal hot spots The symmetric antipodal case is not the only configuration that needs to be addressed. There exists the possibility that the hotspots could be asymmetric, or lie in the same hemisphere (i.e. less than 180° apart). Results for a few Class II (θ, i) configurations are considered in Fig. 5.8. In all cases, very high PF's can be reached without the need for significant beaming.

High Field Radio Pulsars

Case Study: PSR J1119-6127. XMM-Newton observations of PSR J1119-6127 published by Gonzalez et al (2005)[41] report a very high pulsed fraction of $74 \pm 14\%$ in the soft x-ray range $0.5 - 2$ keV, the upper and lower bounds of which are marked in Figures 5.7 and 5.8 (horizontal lines). The characteristic shape of the light curve for this pulsar shows one narrow peak every phase and can probably be classified as Class II (see light curve class definitions above). The favoured fit to the spectrum of this star consists of a two-component Black Body (BB) + power law, with the BB component (< 2 keV) dominating the pulsed emission, contributing over $\sim 85\%$ of the flux. It is a fairly good assumption that the pulse in the light curve profile is produced by this thermal emission originating from the primary spot on the stellar surface. Making the further assumption of antipodal hot spots, it is immediately clear from Figure 5.7 that in order to reach a PF of at least 60% some beaming

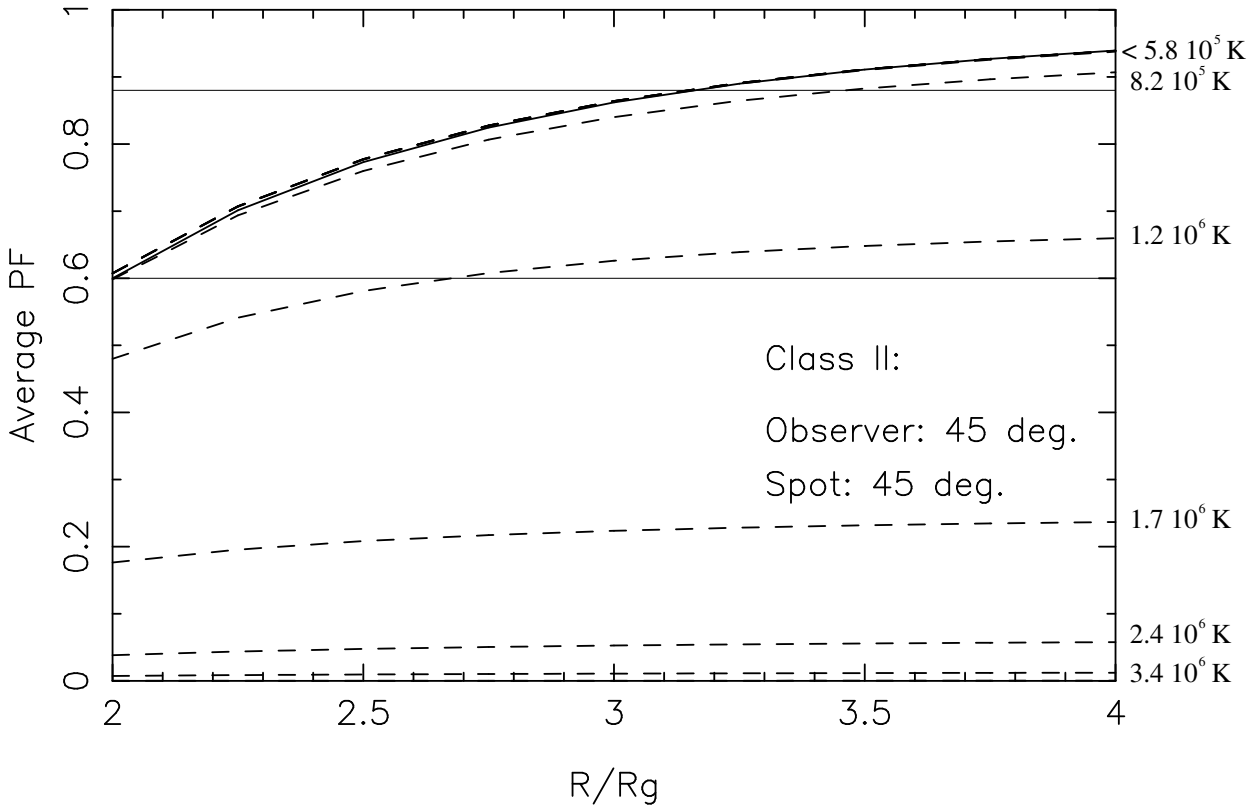

Figure 5.6 The effect of temperature difference between hot spots, T_{sp}, and the main surface, T_{main}. The dashed lines represent PF *vs.* R/r_g for the model star with $BF = 2$, $diam = 10°$, and $(\theta, i) = (45°, 45°)$. The solid line represents PF_{max} fron [15]. T_{sp} is kept at $5 \cdot 10^6$ K and no deviation in PF occurs until $T_{main} = 8.24 \cdot 10^5$ K. The horizontal lines represent the upper and lower bounds for the $PF = 74 \pm 14\%$ of the high field pulsar PSR J1119-6127 [41].

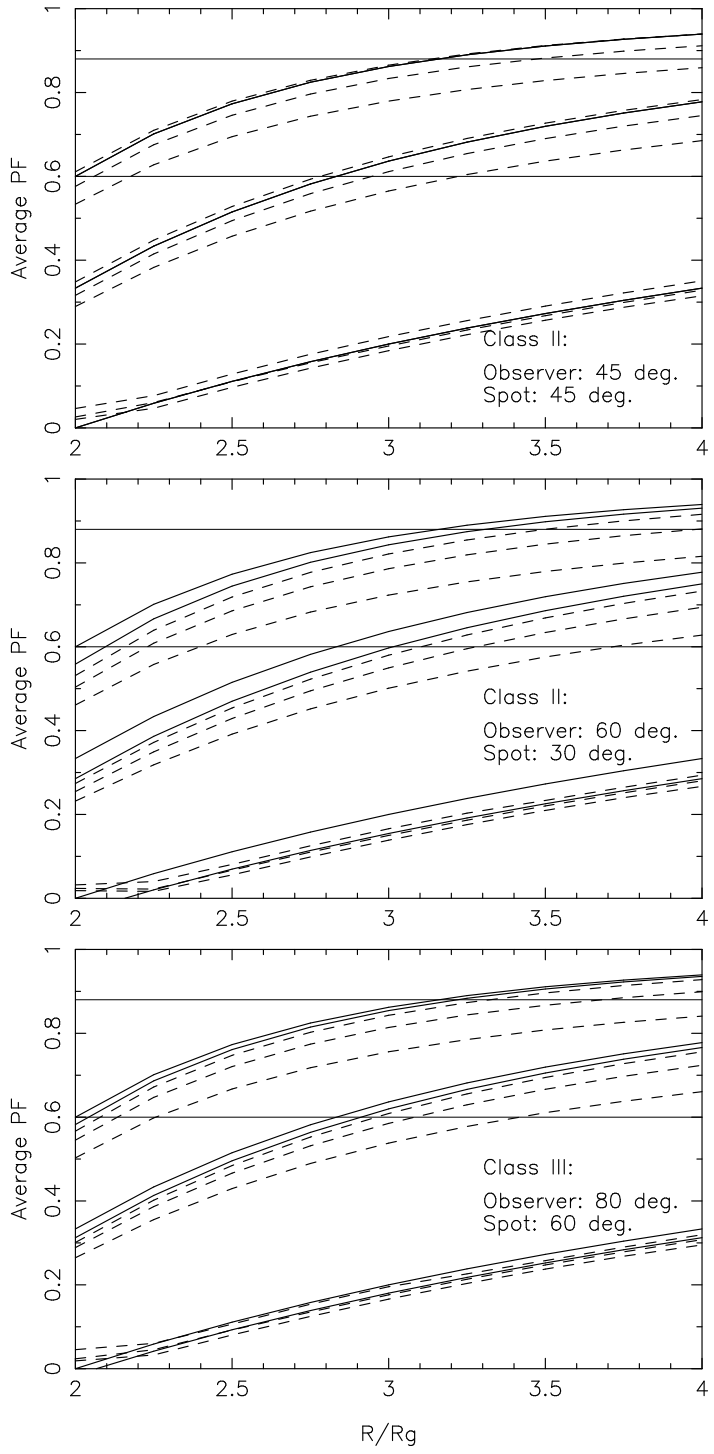

Figure 5.7 Effect of spot diameter and beaming factor on black body pulsed profiles. $(\theta, i) = (45°, 45°) - top, (30°, 60°) - middle, (60°, 80°) - bottom$. Each line type represents a different beaming factor: $BF = 0$ $(dashed\ line)$, $BF = 1$ $(dash - dot\ line)$, $BF = 2$ $(dotted\ line)$. There are three curves per BF which descend with increasing spot size $(diam = 10°, 30°, 50°)$. The solid curves represent theoretical PF_{max} (upper) and PF from equation 5.9, developed from [15]. The horizontal lines represent the upper and lower bounds for the $PF = 74 \pm 14\%$ of the high field pulsar PSR J1119-6127 [41].

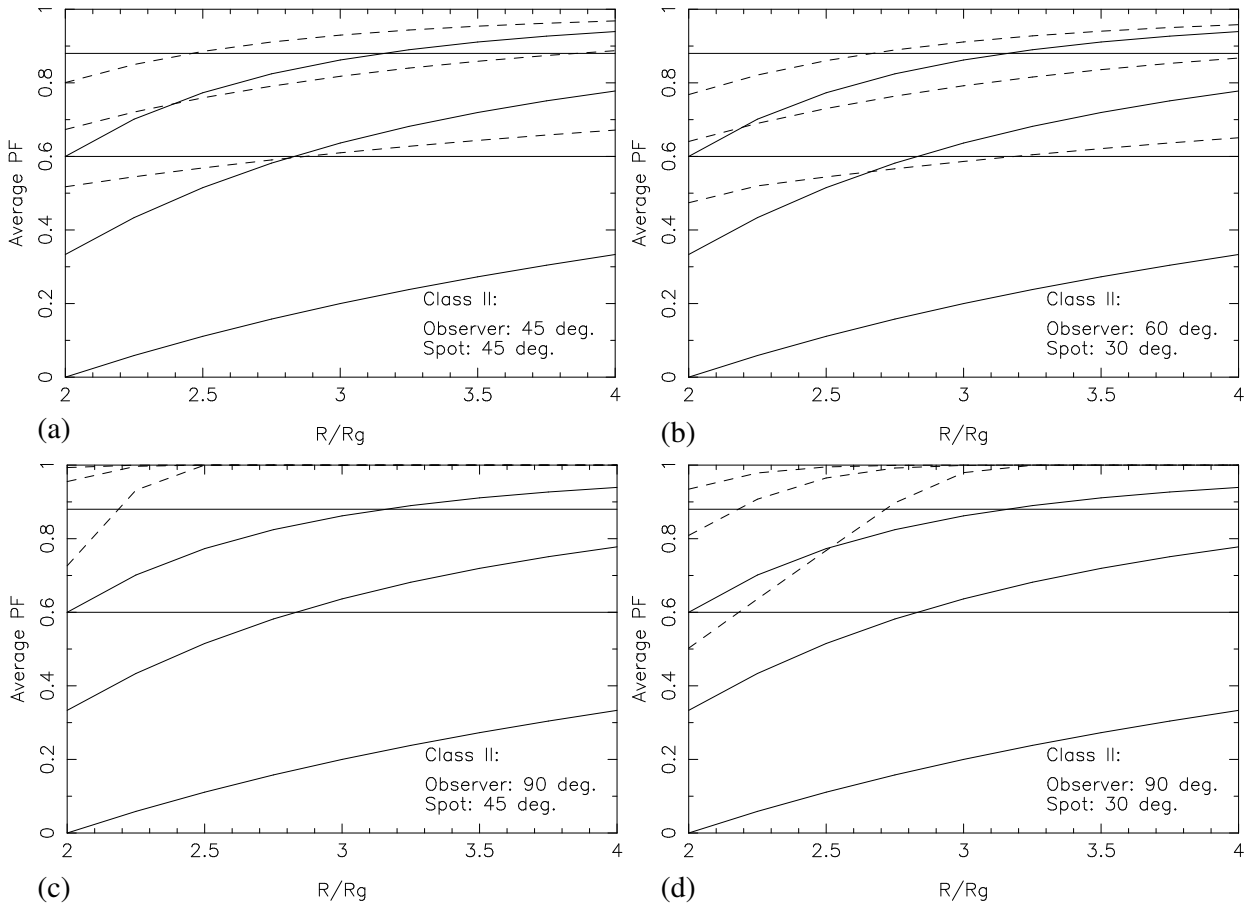

Figure 5.8 Effect of asymmetric hot spots on observed pulsed fraction. Both spots are located in the same hemisphere. $(\theta, i) = a : (45°, 45°), b : (30°, 60°), c : (45°, 90°), d : (30°, 90°)$. A spot diameter of 10° is used. Each line type represents a different beaming factor: $BF = 0$ (*dashed line*), $BF = 1$ (*dash−dot line*), $BF = 2$ (*dotted line*). The solid curves represent theoretical PF_{max} developed from [15] for the antipodal case. The horizontal lines represent the upper and lower bounds for the $PF = 74 \pm 14\%$ of the high field pulsar PSR J1119-6127 [41].

($BF \geqslant 1$) is required. A minimum R is also required depending on the size of the spot (i.e $R \sim 3r_g$ for a spot of $diam = 10°$).

The scenario that initial cooling of neutron stars with strong magnetic fields (i.e. poloidal plus toroidal crustal fields) could account for non-homogenous surface temperatures resulting in hot spots is certainly plausible ([78], [33]) and has been explicitly shown in the previous chapter where Pulsed Fractions over 64% are routinely generated with the approriately strong internal toroidal magnetic fields. Figure 5.9 shows the results for the (θ, i) configurations of the middle panel of Figure 5.7. In this configuration with a 1.4 $M_\odot$ star of radius 14 km and hotspots of diamater 25°, an average PF of 62.6% was reached with a $BF = 1$.

Figure 5.10 shows the results of a simulation supposing that the apparent two-component profile in the observations is statistically significant. In this case in order to produce the profile the two hotspots are *not* antipodal, nor are they of the same temperature. In accordance with Figures 5.6, 5.7 and 5.8, in order to keep the PF within range, the main surface temperature of the star had to be increased as were the spot diameters ($diam = 60°$).

For illustrative purposes, stellar models of the configurations in Figure 5.8 were also used to produce light curves and spectra. Although pulsed fractions approachings 100% were produced for configurations with the observer at 90° to the rotation axis (see Figure 5.8), reasonable PF's within the bounds for PSR J1119-6127 could be achieved for the other configurations, although beaming would still need to be considered for small stars (i.e. $R = 10\ km$ and $BF = 1$).

Other High Field PSR's PSR J1119-6127 is one of a select group of radio pulsars, all of whom are primarily characterized by their high magnetic fields ($B \gtrsim$ the QED value of $4.4 \cdot 10^{13}\ G$ inferred from spin-down characteristics, the $P - \dot{P}$ relation). Although, it's high B field seems to be the only thing it has in common with these other objects. It does not power a bright pulsar wind nebula (PWN), a general characteristic of young energetic pulsars. Neither does it exhibit magnetar-like x-ray emission, as recently manifested by PSR J1846-0258 [31], with whom it shares similar spin properties. Table 3.3 lists some of the properties of the pulsars in this group. Unfortunately, as of yet, none of the other HBPSR's have been detected in thermal x-rays.

Other High PF Pulsars Although PSR J1119-6127 does not share similar x-ray emission properties with other stars in the HBPSR group, nor magnetars, it does have comparable $\dot{E}$

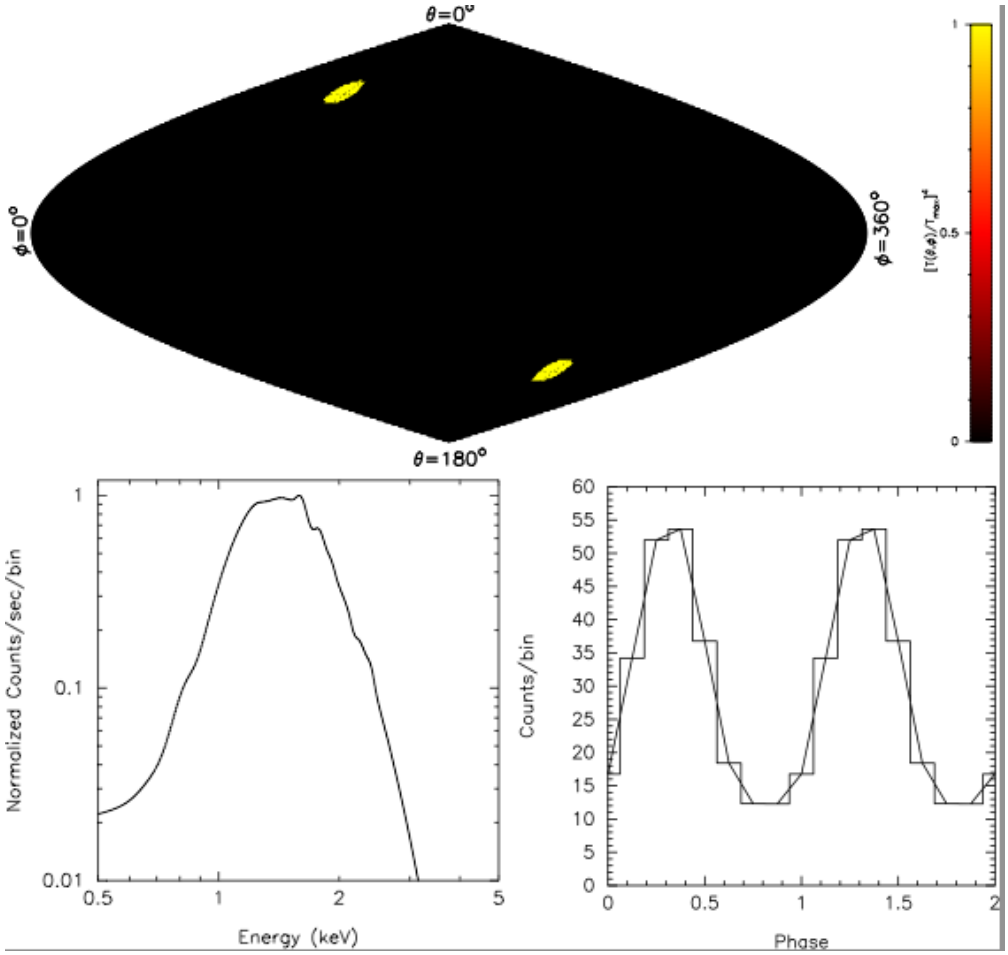

Figure 5.9 Simulated XMM-Newton spectrum (bottom left) and light curve (bottom right) from the model star with a surface temperature distribution consisting of two hotspots ($T_{sp} = 2.8 \cdot 10^6 K$) with $(\theta, i) = (30°, 60°)$ and a cooler main surface ($T_{main} = 3 \cdot 10^5\ K$) (upper panel) in the $0.5 - 2\ keV$ range. Here, a PF of 65.6% was achieved.

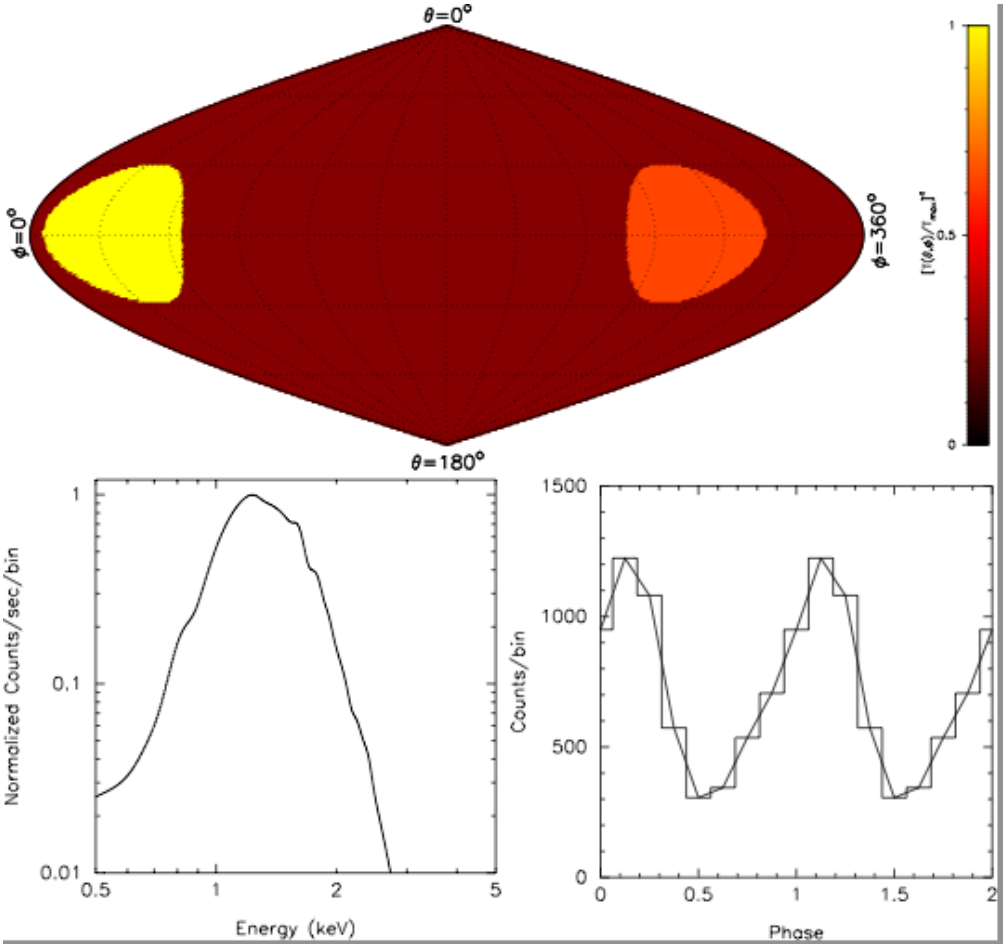

Figure 5.10 Same as Fig. 5.9, except that the two hotspots are not antipodal (located 108° from eachother in ϕ) nor of the same temperature ($T_1 = 2.5 \cdot 10^6 K$ and $T_2 = 2.8 \cdot 10^6 K$) with $(\theta, i) = (90°, 90°)$ and a warmer main surface ($T_{main} = 2 \cdot 10^6\ K$). Here, a PF of 62.6% was achieved.

and dominating thermal x-ray component in its spectrum (< 2 keV) to the more "classical Vela-like" pulsar PSR J1357-6429 [112]. A rather high pulsed fraction in thermal x-rays was also reported for this star ($PF = 63 \pm 15\%$) and was interpreted as originating from anisotropic emission from a magnetized NS atmosphere and non-uniform surface temperature as a result of the magnetic field distribution, the latter nicely coinciding with the argument in this work for the origin of the pulsed thermal emission coming from PSR J1119-6127.

Discussion

It has been shown ([78], [33]) that hot surface caps surrounded by a cooler equatorial belt can be produced from cooling models including the presence of a strong toroidal field in the crusts of neutron stars. As shown above, assuming that the observed thermal x-ray emission does come from the surface of the star, high PF's, as seen in some neutron stars, can be explained by this cooling scenario. In the above models, the most important considerations are beaming effects, stellar size and spot size. In general, if you can say with some kind of certainty that there is symmetry in the hotspot configuration of your particular star, then, according to this study, you can put restrictions on M and R. However, it has not been ruled out that hotspots could occur in the same hemisphere of the star, thus producing higher PF's and leaving the possible ranges of M and R as open as ever.

As per usual, better observations are needed in order to constrain neutron star surface characteristics. Higher timing resolution would be necessary in order to see the real structure of the light curve. That is, if the secondary peak is statistically significant or not as it presence would be a strong indicator for non-antipodal hotspots. This and a deeper observation in order to raise photon counts would also be useful to check for pulsations in the hard band (> 2 keV) and confirm the nature of the hard emission (hard x-rays originating from the magnetosphere of the pulsar are expected to be pulsed).

In an effort to establish, or not, a link between high-field pulsars, isolated neutron stars and magnetars, it has been proposed [41] to search some nearby HBPSRs for thermal surface x-ray emission. If detected, and determined to be pulsed, these sources could be modeled in a similar way to PSR J1119-6127.

As a final note, perhaps a more sophisticated scheme for the dependence of local flux on α should be considered since it is apparent, at least for antipodal hotspots, that some beaming is required in order to reach the realm of PF's over 30% (e.g. [113]).

5.3. Asymmetric Toroidal Fields

Along the lines of the above discussion of neutron star spectra explained by thermal emission from non-uniform surface temperature distributions, a.k.a *hotspots*, we present the curious case of te pulsar PSR J0821-4300, the compact central object in the supernova remnant Puppis A. Gotthelf et al (2010 [42]) showed that its spectrum could be fit by a double blackbody and, furthermore, be explained by a pair of thermal, antipodal hotspots on it's surface and viewing geometry.

Their favoured model is presented in Fig. 5.11, where the surface temperture distribution and observed emission properties have been modelled. The emission is dominated by a relatively small hot spot ($radius = 6.61°$, $T \sim 6 \times 10^6$ K) and a much larger antipodal spot that is a factor of two times cooler ($radius = 34.04°$, $T \sim 3 \times 10^6$ K). The extended cool equatorial region was set arbitrarily low at $T = 10^6$ K. The viewing angle is 86° with respect to the axis of rotation of the pulsar. Its pulsed fraction is 21.7% in the range $1.5 - 4.5$ keV compared to the published value of 19.6%.

One of the tricks in modelling neutron star cooling is choosing a magnetic field geometry. Often, symmetric fields, such as those presented in §4.4 are chosen for their simplicity and overall effects on the surface temperature distribution. The most likely scenario is that the interior of a neutron star is not perfectly symmetric at all, but subject to local dynamics such that one could imagine any possible angular dependence on the supossed crust-confined magnetic field components.

The core-centred dipolar magnetic field of PSR J0821-4300 has a relatively weak upper limit of 2×10^{11} G compared to the highly magnetized neutron stars generally considered so far. In the context of surface hotspots generated from the thermal history of the star leaves the responsibility of their extreme difference up to a very strong, and more importantly *confined*, magnetic field. The idea of a submerged magnetic field in young neutron stars is not a new one. Geppert et al (1999 [34]) considered the effect of accretion from core-collapse supernovae on the internal magnetic field. In cases where the flow from accretion would overpower ohmic diffusion, the initial magnetic field would be pushed down and frozen at greater depths within the star. As the star ages, it's magnetic field would diffuse outwards resulting in a delayed "switch on" of its pulsar properties.

A star of a young age such as PSR J0821-4300 at 3700 years, could still conceivably have such a magnetic field, the bulk of which is still frozen within the crust. The following

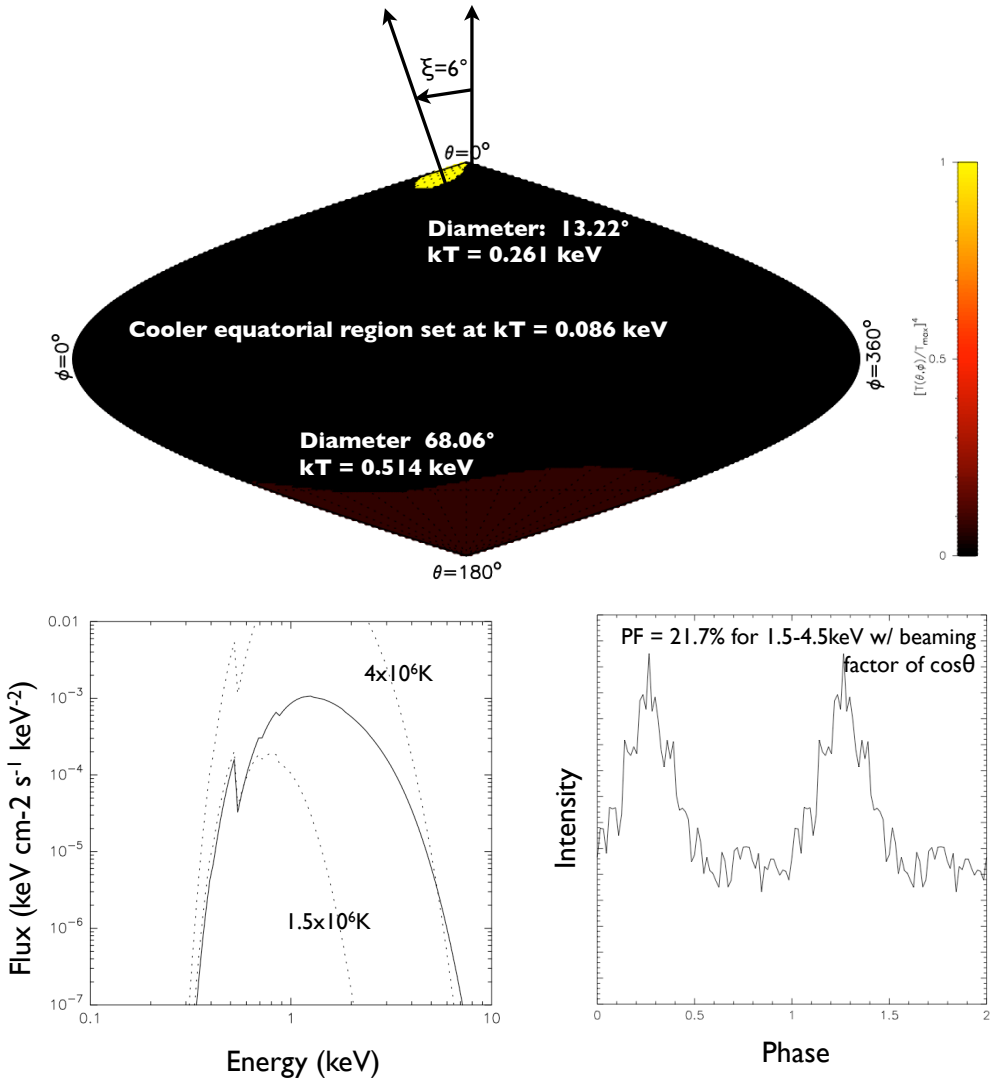

Figure 5.11 Surface temperature model of PSR J0821-4300 presented in [42] using the code found in [69, §4.4]. Spectral and light curve properties calculated using the pulsar's $R = 12$ km, $d = 2.2$ kpc and $N_H = 4.8 \times 10^{21}$ cm^{-2}.

two models, A and B, were produced using such scenarios inserted into the 2D cooling code presented in the previous chapter. Their differing magnetic fields are presented in Fig. 5.12. In order to recreate the dramatic temperature difference between the polar hotspots of PSR J0821-4300, a strong toroidal field ($B_o^{tor} = 10^{16}$ G) with it's maximum relatively near the surface at $0.7r_{crust}$ (see the Stoke's functions in the bottom left panel of Fig. 5.12) was constructed using two different angular dependencies. Both models have the same core-centered dipolar field ($B_o^{core} = 2 \times 10^{11}$ G) and the same, stronger, crust-confined poloidal field ($B_o^{pol} = 10^{13}G$, the components of which that stretch outside the star will hoever add to the overall magnetic field strength). Note that the bulk of the poloidal fields influence on heat flow is deeper within the crust than even the toroidal field.

The results are presented in Fig. 5.12. It can immediately be seen that both models can reproduce a single small hotter spot at one pole. Note that the geometry of Model B is flipped with repect to Model A and the model of PSR J0821-4300 in Fig. 5.11. However, an extended antipodal warmer region was more difficult to achieve, particularly with a cool equatorial belt, and thus higher pulsed fractions than desired were created (36.9% and 37.8% for Models A and B respectively).

One of the main difficulties in these first attempts at modelling PSR J0821-4300 is the balance between making a two-fold temperature difference between the relatively smaller hot spot and it cooler extended anipodal spot and creating an equatorial region that is cooler still. The strong asymmetric toroidal "wall" was deliberately placed in shallow depths in order to exagerrate the small hotspot and effectively block heat from the core in the rest of the star. The effect of a magnetized envelope was actually desirable in these models as it tends to allow a higher temperature along the poles for a given base temperature, T_b (see Fig. 3.10), thus further widening the temperature gap.

The models show the ability for the mysterious and arbitrary parameters of the interior magnetic field configuration to gain control of the surface temperature of the star and influence it in such a way as to cause the dramatic hot spot configurations found on stars such as PSR J0821-4300. It certainly supports that a submerged, but strong, magnetic field is likely. Further "fiddling" with the magnetic field will most likely improve results. Whether such asymmetric interior fields could come out of magnetic field evolution model remains to be seen.

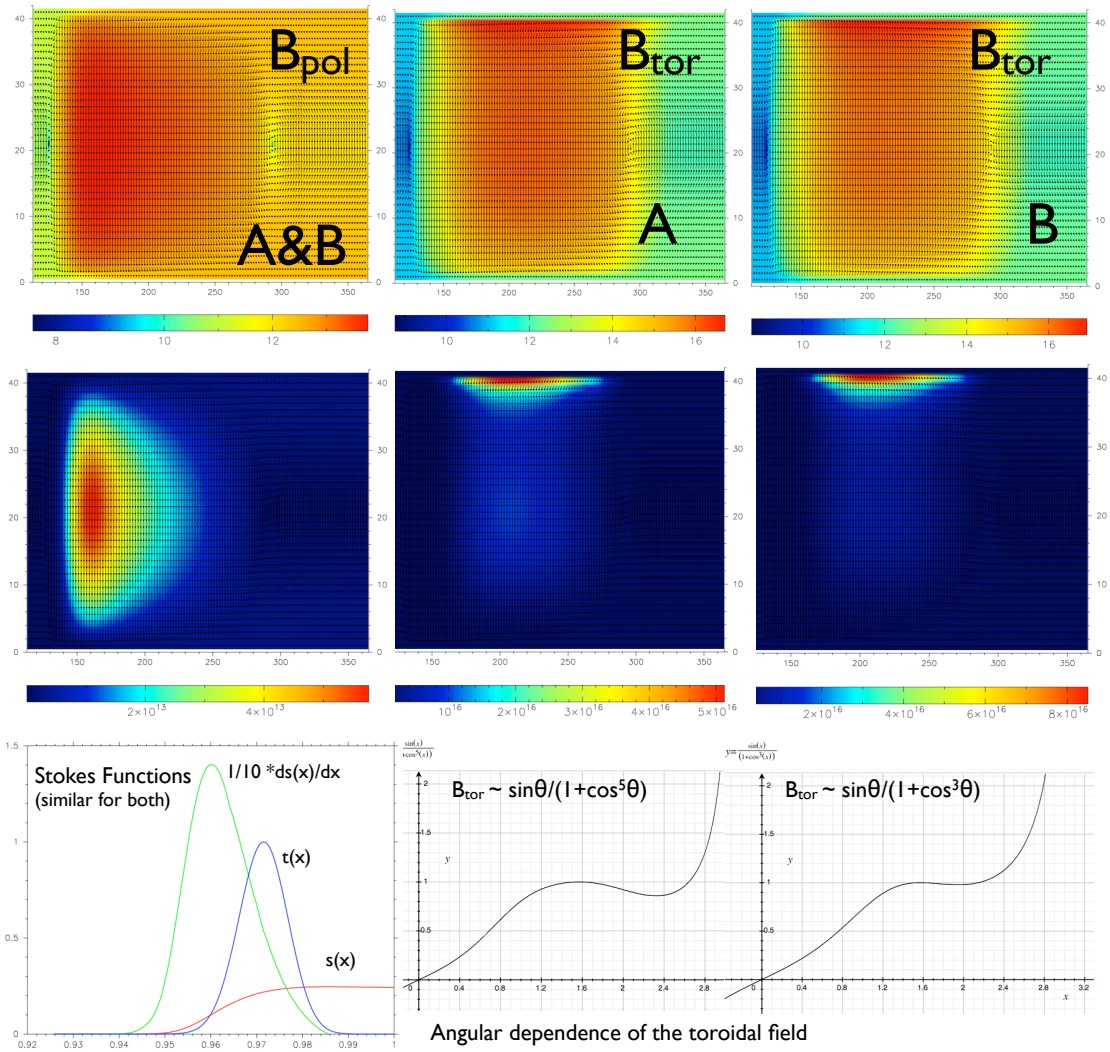

Figure 5.12 Assymetric toroidal field models and their varying angular dependencies.

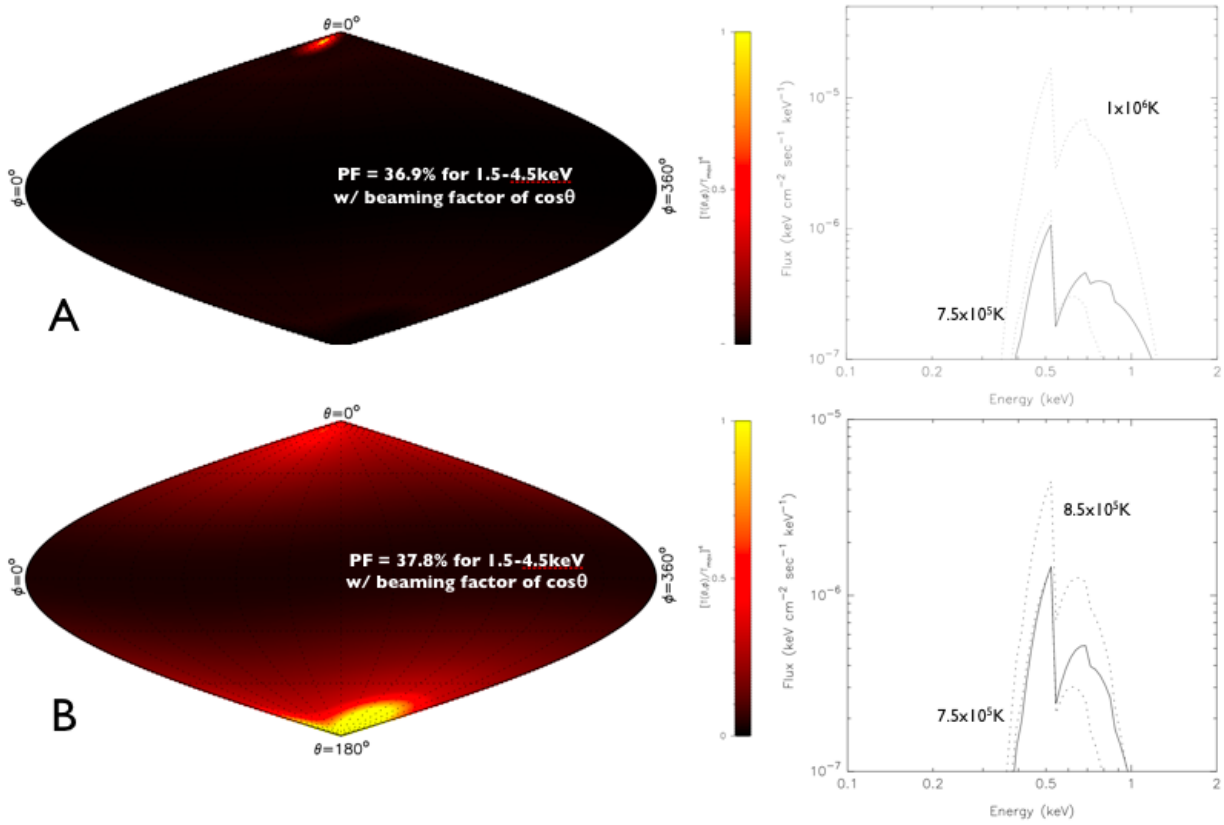

Figure 5.13 Surface temperature maps of models A and B presented in Fig. 5.12 using the code found in [69, §4.4]. Spectral and light curve properties calculated using PSR J0821-4300 properties $R = 12$ km, $d = 2.2$ kpc and $N_H = 4.8 \times 10^{21}$ cm^{-2} from [42].

5.4. Strange Stars

The possibility exists that some *neutron* stars could very well be *quark* stars and there is much research into the Equation of State of deconfined quark matter in the core of a compact star. This was first introduced by Itoh, 1970 [52] and continues to this day.

The following article is based on one of the propositions of this thesis: that the combination of a crust-confined magnetic field in a compact star and the thermal diffusion within said star will create a non-uniform surface temperature distribution. A surface with hot polar caps and a cooler equatorial belt could explain the observed spectra of some neutron stars. That is, the hot x-ray temperature predict a smaller radius for the star than its cooler optical counterpart. One possible inherent characteristic of these stars could be their relatively small radial size. The existence of a very thin crust covering the star then could be possible only when the electron density inside is less than that of the quark matter. Using the star RX J1856.5-3754 as a model candidate due to its small inferred radius, we calculate thermal diffusion inside stars based on the models of Geppert et al [33] supposing a quark core described by Farhi & Jaffe (1984)[26].

As in the case of neutron stars, it can be shown that the magnetic field configurations that result in non-uniform surface temperature distributions can exist in the baryonic crusts of quark stars, despite their meager depth. However, in order to reproduce the observations, the magnetic field strength, in particular that of the toroidal field, must be on the order of $10^{15}G$. When one considers that magnetif stresses can reach $B_r B_\theta/4\pi \sim 10^{26}\ dyne\ cm^{-2}$ for a $B_0^{corteza}$ de $10^{13}G$, it is doubtful that a crust of a depth only $200-300\ m$ [89] could support it.

Nevertheless, a detailed investigation into the non-linear evolution of a coupled poloidal and toroidal magnetic field is still lacking in order to see if a million year old star could maintain a magnetic field of $10^{15}G$ supposing that it was initially born with one that would have been several orders of magnitude even larger.

Astrophys Space Sci (2007) 308: 513–517
DOI 10.1007/s10509-007-9329-7

ORIGINAL ARTICLE

RX J1856.5-3754 as a possible strange star candidate

Jillian Anne Henderson · Dany Page

Received: 16 November 2006 / Accepted: 21 November 2006 / Published online: 24 March 2007

Abstract RX J1856.5-3754 has been proposed as a strange star candidate due to its very small apparent radius measured from its X-ray thermal spectrum. However, its optical emission requires a much larger radius and thus most of the stellar surface must be cold and undetectable in X-rays. In the case the star is a neutron star such a surface temperature distribution can be explained by the presence of a strong toroidal field in the crust (Pérez-Azorín et al.: Astron. Astrophys. 451, 1009 (2006); Geppert et al.: Astron. Astrophys. 457, 937 (2006)) We consider a similar scenario for a strange star with a thin baryonic crust to determine if such a magnetic field induced effect is still possible.

Keywords RX J1856.5-3754 · Strange star · Neutron star

PACS 26.60.+c · 97.60.Jd · 95.30.Tg

1 Introduction

Quark stars have long ago been proposed as an alternative to neutron stars (Itoh 1970). The "strange matter hypothesis" (Witten 1984) gave a more precise theoretical formulation for their existence: that at zero pressure three flavor quark matter, i.e. with u, d and s quarks, has a lower density per baryon than nuclear matter and would hence be the true ground state of baryonic matter. These stars are now called "strange stars" (Alcock et al. 1986; Haensel et al. 1986) and share many similarities with neutron stars: they can have similar masses, have similar radii in the observed range of masses, similar cooling histories and, to date, it has been practically impossible to conclusively prove or disprove their existence (for recent reviews, see Weber 2005; Page et al. 2006; Page and Reddy 2006).

One possible distinctive property of a strange star could be a small radius. Given the impossibility to treat quark-quark interactions from first principles, i.e. starting from Q.C.D., at densities relevant for compact stars, only simplified models are possible and results are, naturally, model dependent. However, several classes of such models do predict small radii, $5 < R < 10$ km at masses $\sim 1.4 M_\odot$ (see, e.g., Dey et al. 1998; Hanauske et al. 2001), and *all* models predict very small radii, $\leq$5 km, at masses $\ll 1 M_\odot$. Hence, measurement of a compact star radius giving a radius $\ll 10$ km directly allows a claim for a strange star candidate.

The "Magnificent Seven" (Haberl 2007) arouse great expectations to measure compact star radii with high enough accuracy to put strong constraints on the dense matter equation of state. In particular, fits of the observed soft X-ray thermal spectrum of RX J1856.5-3754 (Pons et al. 2002) pointed to a very small radius and lead to the claim that this object may be a strange star (Drake et al. 2002). However, observations in the optical band allowed the identification of the Rayleigh–Jeans tail of a second component of the surface thermal emission, corresponding to a lower temperature and much larger radius than the component detected in the X-ray band. An interpretation of these results is that the surface temperature of the star is highly non-uniform (Pons et al. 2002; Trümper et al. 2004), possibly

This work was partially supported by PAPIIT, UNAM, grant IN119306. J.A.H. studies at UNAM and travel to London are covered by fellowships from UNAM's Dirección General de Estudios de Posgrado.

J.A. Henderson (✉) · D. Page
Instituto de Astronomía, Universidad Nacional Autónoma de México, Ciudad Universitaria, Mexico, D.F., CP 04510, Mexico
e-mail: hendersj@astroscu.unam.mx

D. Page
e-mail: page@astroscu.unam.mx

due to the presence of a strong magnetic field. Models of surface temperature distribution with purely poloidal magnetic fields (Page 1995; Geppert et al. 2004) do predict non-uniform surface temperature distributions, but such inhomogeneities are not strong enough to produce such small X-ray emitting regions surrounded by large cold regions detectable in the optical band as observed. However, inclusion of a toroidal component of the magnetic field, confined to the neutron star crust, has a dramatic effect (Pérez-Azorín et al. 2006; Geppert et al. 2006; see also Pons 2007; Page 2007): this field component inhibits heat from the stellar core to flow to the surface through most of the crust, except for small domains surrounding the magnetic axis, and results in highly non-uniform surface temperature distributions producing good fits to the observed thermal spectra, from the optical up to the X-ray band.

These models of small hot regions, detected in the X-ray band, surrounded by large cold regions, detected in the optical band, which allow to reproduce the entire observed thermal spectrum and results in large radii for the star are in contradiction with the proposed strange star interpretation of RX J1856.5-3754, which was based on the small radius detected in the X-ray band. Here we want to push the discussion one step further: are these highly non-uniform surface temperature distributions, assuming they are real, incompatible with a strange star model? We consider strange stars having a thin crust, composed of normal baryonic matter, with a strong magnetic field. Since a strange star crust can, at most, reach the neutron drip density, it is much thiner than the crust of a normal neutron star and the specific question is: can such a thin layer produce the surface temperature distributions deduced from observation?

2 The strange star models

We will consider strange star models built on the MIT-bag inspired equation of state of (Farhi and Jaffe 1984) which has three parameters: the QCD coupling constant α_s, the bag constant B and the strange quark mass m_s (u and d quarks are treated as massless). Figure 1 illustrates four families of such strange matter models: by varying the parameters, these equations of state allow the production of a wide range of models, from very compact stars up to very large ones. It is important to notice from this figure that, depending on the assumed parameters of the model, strange stars can have large radii and thus, although a small radius measurement is a strong argument in favor of a strange star, a large radius is *not* an argument against a strange star.

On top of the quark matter, a thin crust can exist as long as the electron density within it is smaller than that in the quark matter (Alcock et al. 1986). Such a baryonic crust is, however, much thinner than a neutron star crust as illustrated in Fig. 2.

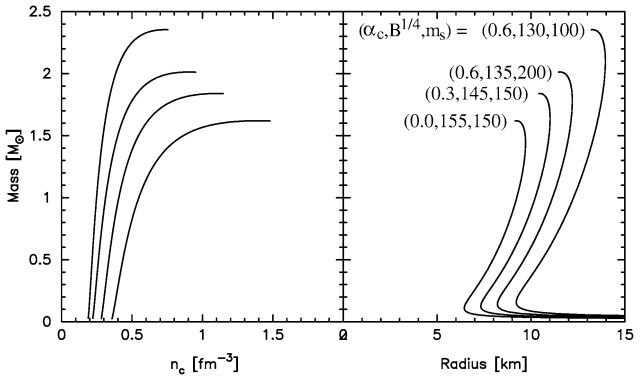

Fig. 1 Mass vs. central density (*left*) and radius (*right*) for strange stars built with four MIT-bag inspired models of strange matter (model parameters are indicated in the *right panel*) and covered by a thin baryonic crust (see Fig. 2)

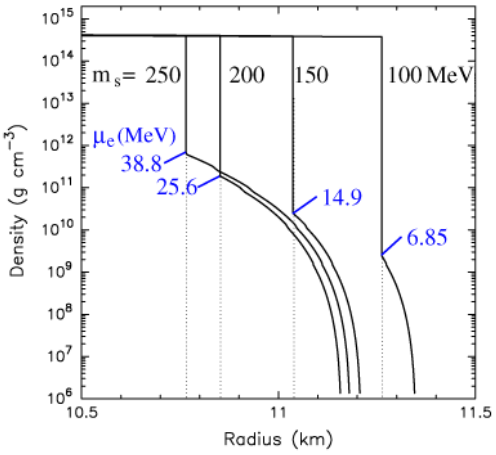

Fig. 2 Density profile of the upper layers of four strange stars built with four MIT-bag inspired models of strange matter, using $\alpha_s = 0.3$, $B^{1/4} = 140$ MeV and four different strange quark masses as indicated. Indicated are also the electron chemical potentials μ_e at the quark surface, which is the parameter determining the maximum baryonic crust density, i.e., the baryonic crust thickness. The crust equation of state is from (Haensel et al. 1989)

Following the neutron star models presented by Geppert et al. (2006) we consider dipolar magnetic fields with three components (Fig. 3): a poloidal one maintained by currents in the quark core, $\mathbf{B}^{\rm core}$, a poloidal one maintained by currents in the baryonic crust, $\mathbf{B}^{\rm crust}$, and a toroidal one maintained by currents in the baryonic crust, $\mathbf{B}^{\rm tor}$. The separation between currents in the crust and in the core is motivated by the likely fact that quark matter forms a Maxwell superconductor (Alford 2001; Page and Reddy 2006): at the moment of the phase transition, occurring very early in the life of the star, superconductivity will prevent any current in the crust from penetrating the core while currents in the core will become supercurrents and be frozen there. Moreover, flux expulsion due to the star's spin-down can also signif-

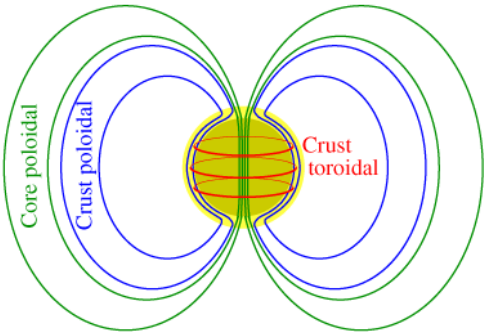

Fig. 3 The three components of the magnetic field considered in this work

icantly increase the crustal field at the expense of the core field.

The importance of the crustal field is that its field lines are forced to be closed within the crust and hence it has a very large meridional component B_θ, compared to the core component. Due to the classical Larmor rotation of electrons, a magnetic field causes anisotropy of the heat flux and the heat conductivity becomes a tensor whose components perpendicular, $\kappa_\perp$, and parallel, $\kappa_\parallel$, to the field lines become

$$\kappa_\perp = \frac{\kappa_0}{1+(\Omega_B \tau)^2} \quad \text{and} \quad \kappa_\parallel = \kappa_0 \tag{1}$$

where κ_0 is the conductivity in the absence of a magnetic field, Ω_B the electrons cyclotron frequency and τ their collisional relaxation time. The large values of B_θ in the crust have the effect of inhibiting radial heat flow except in regions close to the magnetic axis where B_r dominates over B_θ (Geppert et al. 2004).

3 Strange stars - results

We performed heat transport calculations using the 2D code described in Geppert et al. (2004) which incorporates the thermal conductivity anisotropy described by (1). Details of the crust microphysics are as described in Geppert et al. (2004, 2006). We consider a strange star model with a radius of ∼11 km and a baryonic crust of thickness ∼250 m for a $1.4 M_\odot$ mass. The two poloidal components of the magnetic field are parametrized by $B_0^{\rm core}$ and $B_0^{\rm crust}$ which are the strengths of the corresponding field components at the surface of the star along the magnetic axis so that, ideally, $B_0^{\rm core} + B_0^{\rm crust}$ would be the dipolar field estimated from the star's spin-down. Notice that the maximum value of $B^{\rm core}$ in the crust is only slightly larger than $B_0^{\rm core}$ while *maximum values of* $B^{\rm crust}$ *are up to almost 100 times larger than* $B_0^{\rm crust}$ due to its large tangential component, $B_\theta^{\rm crust}$, resulting from the compression of the field within the narrow crust. The strength of the toroidal field is parametrized by $B_0^{\rm tor}$, defined as the maximum value reached by $B^{\rm tor}$ within the crust. We keep $B_0^{\rm core}$ at 10^{13} G and vary $B_0^{\rm crust}$ and $B_0^{\rm tor}$.

We display in Fig. 4 the resulting crustal temperature profiles for several typical values of $B_0^{\rm crust}$ and $B_0^{\rm tor}$. One sees that, independently of the strength of the poloidal component, $B_0^{\rm tor}$ needs to reach 10^{15} G to have a significant effect, a result similar to what was obtained by Geppert et al. (2006) for the neutron star case. However, independently of the value of $B_0^{\rm tor}$, once $B_0^{\rm crust}$ reaches 10^{13} G highly non-uniform temperature profiles develop in the thin strange star crust: such profiles are sufficiently non-uniform to produce the wanted surface temperature distribution, i.e. small hot regions surrounded by extended cold ones.

4 Discussion and conclusions

The optical + X-ray spectrum of RX J1856.5-3754, when fitted with blackbodies, requires two components with very different temperatures and emitting areas. The implied highly non-uniform surface temperature distribution can be physically justified by the introduction of a very strong magnetic field, whose supporting currents are mostly located within the star's crust. We have shown here that, similarly to the neutron star case, such field configurations can be found in the case of a strange star, despite the shallowness of its baryonic crust. However, the strength of these fields, either the toroidal component $\mathbf{B}^{\rm tor}$ or the crust anchored poloidal one $\mathbf{B}^{\rm crust}$ must reach strengths close to, or above, 10^{15} G to produce the desired temperature anisotropy. Similarly to the neutron star case, such surface temperature distributions impose severe, but not unrealistic, restrictions on the orientation of either the observer or the magnetic field symmetry axis with respect to the rotation axis to explain the absence of pulsations (Braje and Romani 2002; Geppert et al. 2006).

That the thin strange star crust can support such huge field strengths is an open question, but a positive answer seems doubtful as some simple estimates illustrate. The magnetic shear stress, $B_r B_\theta / 4\pi$, reaches 10^{26} dyne cm^{-2} in the crust when $B_0^{\rm crust}$ reaches 10^{13} G, which is comparable or higher to the maximum value sustainable by a crust of thickness $\Delta \sim$ 200–300 m (Ruderman 2004): violent readjustments of the crust are expected but have yet to be observed in any of the "Magnificent Seven". Moreover, the ohmic decay time in the low density crust is relatively short, less than 10^5 yr (Page et al. 2000), and the presence of such a strong field in a $\sim 10^6$ yr old star would require an initial crustal field about two orders of magnitude higher when the star was young. (However, the highly non-linear evolution of coupled strong poloidal and toroidal magnetic fields remains to be studied under such conditions.)

We have also adopted the very ingenuous assumption that the surface emits as a perfect blackbody. A condensed

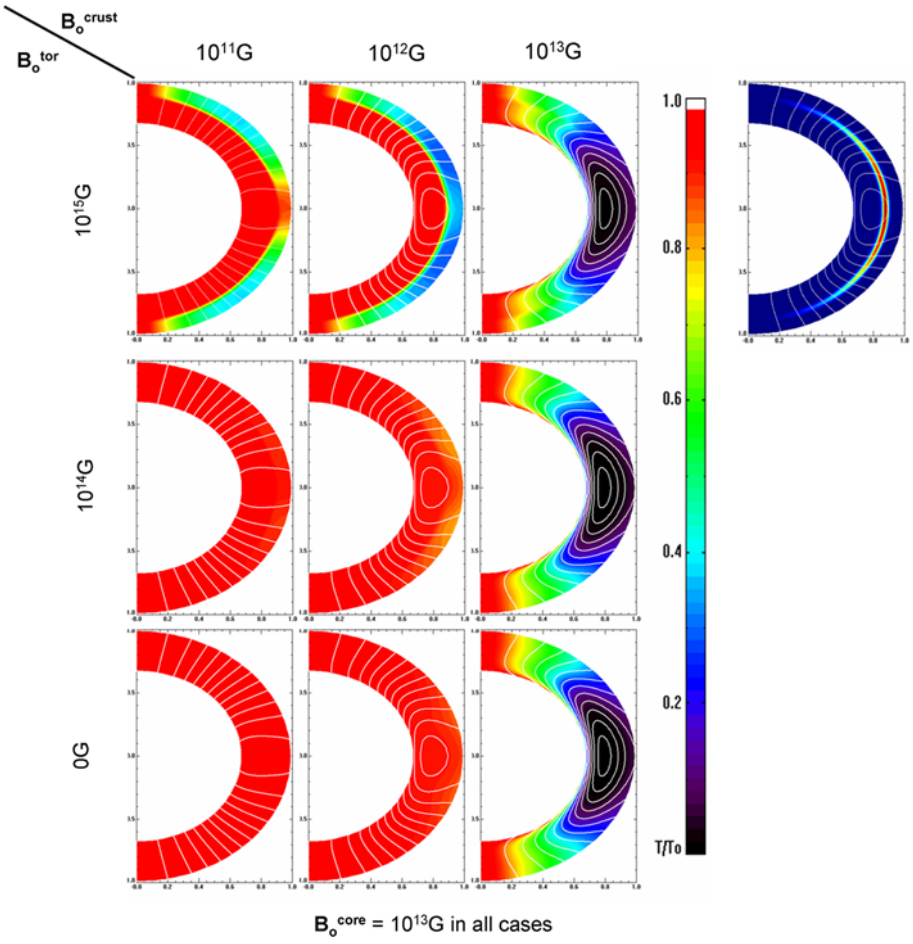

Fig. 4 Crustal temperature profiles for various strange star magnetic field structures according to the model parameters (see text for details). The radial aspect of the crust has been stretched by a factor of 15 in order to clearly show the thermal structure. The *upper right profile* shows the field lines of the poloidal component $\mathbf{B}^{\rm core} + \mathbf{B}^{\rm crust}$ (*white lines*) and the intensity distribution of the toroidal component $\mathbf{B}^{\rm tor}$ (*in colours*)

matter surface may simulate a blackbody spectrum (Turolla et al. 2004; Pérez-Azorín et al. 2005; van Adelsberg et al. 2005) but such models still require strong fields to produce a non-uniform temperature distribution (Pérez-Azorín et al. 2006). However, other interpretations are possible, such as a thin atmosphere atop a solid surface (Motch et al. 2003; Ho et al. 2007) which may be able to reproduce both the optical and X-ray spectra without invoking strongly non-uniform temperatures and can be applied as well to strange stars with a crust as to neutron stars since they only consider the very surface of the star.

In conclusion, the crustal field scenario, which is successful when applied to neutron star models in order to explain the observed thermal spectrum properties of RX J1856.5-3754, can be "successfully" applied to a strange star model but requires such a huge magnetic field confined within such a thin crust that its applicability is doubtful. It is hence difficult to conciliate the observed, from optical to X-ray, properties of RX J1856.5-3754 with a strange star interpretation unless these are due exclusively to the emitting properties of its surface.

Acknowledgements We thank M. Küker and U. Geppert for allowing us to use their 2D transport code.

References

Alcock, C., Farhi, E., Olinto, A.: Astrophys. J. **310**, 261 (1986)
Alford, M.: Annu. Rev. Nucl. Part. Sci. **51**, 131 (2001)
Braje, T.M., Romani, R.W.: Astrophys. J. **580**, 1043 (2002)
Dey, M., Bombaci, I., Dey, J., et al.: Phys. Lett. B **438**, 123 (1998)
Drake, J.J., Marshall, H.L., Dreizler, S., et al.: Astrophys. J. **572**, 996 (2002)
Farhi, E., Jaffe, R.L.: Phys. Rev. D **30**, 2379 (1984)
Geppert, U., Küker, M., Page, D.: Astron. Astrophys. **426**, 267 (2004)
Geppert, U., Küker, M., Page, D.: Astron. Astrophys. **457**, 937 (2006)
Haberl, F.: Astrophys. Space Sci. **308**. DOI 10.1007/s10509-007-9342-x (2007)
Haensel, P., Zdunik, J.L., Schaeffer, R.: Astron. Astrophys. **160**, 121 (1986)
Haensel, P., Zdunik, J.L., Dobaczewski, J.: Astron. Astrophys. **222**, 353 (1989)
Hanauske, M., Satarov, L.M., Mishustin, I.N., et al.: Phys. Rev. D **64**, 3005 (2001)
Ho, W.C.G., Kaplan, D.L., Chang, P., et al.: Astrophys. Space Sci. **308**. DOI 10.1007/s10509-007-9366-2 (2007)
Itoh, N.: Prog. Theor. Phys. **44**, 291 (1970)
Motch, C., Zavlin, V.E., Haberl, F.: Astron. Astrophys. **408**, 323 (2003)
Page, D.: Astrophys. J. **442**, 273 (1995)
Page, D.: Astrophys. Space Sci. **308**. DOI 10.1007/s10509-007-9316-z (2007)
Page, D., Geppert, U., Zannias, T.: Astron. Astrophys. **360**, 1053 (2000)

Page, D., Geppert, U., Weber, F.: Nucl. Phys. A **777**, 497 (2006)
Page, D., Reddy, S.: Annu. Rev. Nucl. Part. Sci. **56**, 327 (2006)
Pérez-Azorín, J.F., Miralles, J.A., Pons, J.A.: Astron. Astrophys. **433**, 275 (2005)
Pérez-Azorín, J.F., Miralles, J.A., Pons, J.A.: Astron. Astrophys. **451**, 1009 (2006)
Pons, J.A., Walter, F.M., Lattimer, J.M., et al.: Astrophys. J. **564**, 981 (2002)
Pons, J.: Astrophys. Space Sci. **308**. DOI 10.1007/s10509-007-9336-8 (2007)
Ruderman, M.: In: Baykal, A., Yerli, S.K., Gilfanov, M., Grebenev, M. (eds.) The Electromagnetic Spectrum of Neutron Stars (e-print: astro-ph/0410607)
Trümper, J.E., Burwitz, V., Haberl, F., et al.: Nucl. Phys. B Proc. Suppl. **132**, 560 (2004)
Turolla, R., Zane, Z., Drake, J.J.: Astrophys. J. **603**, 265 (2004)
van Adelsberg, M., Lai, D., Potekhin, A.Y., et al.: Astrophys. J. **628**, 902 (2005)
Weber, F.: Prog. Nucl. Part. Phys. **54**, 193 (2005)
Witten, E.: Phys. Rev. D **30**, 272 (1984)

Chapter 6

Summary and the Future

Neutron stars continue to be a fascinating laboratory for matter at extreme densities. Increasingly improved astronomical observations of compact objects such as pulsars and other neutron star phenomena has created the need for a comprehensive physical description of matter around nuclear density. In the cores of neutron stars densities are supra-nuclear, whose mysterious properties governing observable spectra is increasingly evident. One such aspect in determining the observable surface temperature, spectrum and timing properties is heat transport within the star. In the outer less dense layers the properties of matter is much better understood partly due to experimental nuclear physics results performed on Earth and more thoroughly tested mathematical treatments of particle interactions in the sub-nuclear regime. This insulating outer layer takes the heat generated in the core and determines the resulting surface temperature profile which in turn is observed and interpreted, thus providing a window into the depths of compact matter.

In this thesis project, I have aimed to improve upon existing one-dimensional temperature evolution calculations by extending to two- and three-dimensional models which are second-order accurate in both time and space. The purpose is to accurately reproduce the thermal history of a neutron star based on an input model of matter at high density, or equation of state, which can then be compared to existing observations of surface temperature and thus narrow down the rather vast field of theories of post-nuclear matter. Besides surface temperature, processes such as superfluidity turn-on times [75] or the effects of crustal heating mechanisms [50] such as accretion of material from a companion star can also be seen on so-called cooling curves, the results of thermal evolution calculations.

My work has also encompassed the effects of magnetic field configuration and strength on

heat transport and resulting surface temperature anisotropies. This in turn has been investigated as a probable explanation for variable thermal x-ray observations and additional source heating from magnetic field decay. An example was investigated in §5.1 where additional heating due to magnetic field decay shows how surface temperature could be maintained hot enough to account for the observed high temperatures of some magnetars (see Fig. 5.4).

Pulsations in thermal x-ray spectra from pulsars with unusually high pulse fractions were investigated in §5.2. A correlation between pulse fraction and stellar size (mass, radius) is made based on the idea that a strong magnetic field is present. Simple but elegant space-time geometry is applied to model stellar spectra [15]. The goal is to create a self-consistent picture of neutron star total mass, which is dependent on the particular equation of state of matter at high density, and its inherent magnetic field.

A natural expansion of this project could include, though is not limited to, expanding and improving two-dimensional neutron star cooling numerical modeling code to three dimensions in order to properly account for asymmetrical magnetic field effects on heat transport within the star. Currently, the complex mathematics involved in modeling an evolving magnetic field within a star force the most stable evolution codes to use mainly static magnetic fields or those with simplified evolution estimates [80].

Adding the third dimension in a problem as complicated as energy transport in a neutron star increases complexity by orders of magnitud. As mentioned previously, Finite Difference methods are relatively fast and sufficiently accurate for the problem of a spherically symmetric star in two-dimensions with well-defined boundaries, but the addition of the azimuthal direction introduces a *periodic* boundary condition which, although it can be represented by Finite Differences, may perhaps be better reproduced by a method specifically designed for boundary-value problems (e.g. Fourier and Cyclic-Reduction methods).

Another natural progression of the code described within would be a possible evolving magnetic field in both two and three dimensions. As mentioned previously, static magnetic field configurations were tested here. Recently, there has been advancement in solving the complexity of this problem by [104] who has developed an "upwind" finite-differencing scheme for magnetic field evolution that can be solved for in turn with solving heat diffusion. A scheme such as this could possibly be "glued" in to the code from the current project.

Part of the usefulness of having a multidimensional energy transport code for compact stars is the ability to model certain physical phenomena whose mechanisms remain mysterious. One such process would be high energy bursts observed in some strongly magnetized

neutron stars, or magnetars [88]. The origin of such a spike in energy output in these stars could be investigated by artificially inserting a strong energy source in an energy transport code such as that developed as part of my PhD thesis, and observing model output of its temperature evolution over time. Such model output can then be directly compared to astronomical observations of the temporal evolution of these bursts as well as their spectra and may well answer the reigning question: how are magnetar bursts powered? [5]. Successful modeling could, furthermore, constrain at what depth within the star burst energy originates and, therefore, what kinds of physical process are occurring at particular densities. Multidimensional models of these events produced from the numerical code developed in my thesis would be a desirable extension to existing one-dimensional results [5].

On the frontiers of nuclear physics is the question: how does matter behave in the ultra-dense regime? As mentioned above, the physical extremes experienced within compact stars are irreproducible on Earth, making these objects unique laboratories for studies of matter in extraordinary environments. One of the essential inputs to an energy transport evolution code is the Equation of State or the relationship between the pressure and the density of matter, whose lowest energy state dictates the local chemical composition. The composition within a star necessarily dictates how energy moves within and without, leaving its observational signature for astronomers on Earth. Numerical models, such as those proposed here, thus provide the testing ground for physical theories of matter, including superfluidity and exotic states such as Strange Stars with de-confined quark cores [107].

The Equation of State (EOS) describes the fundamental state of matter in thermodynamic equilibrium at $T = 0$. At a temperature of $T \sim 10^9 K$ nuclear reactions are so slow that we can assume the chemical composition of each density layer within the star remains uniform with the exception of processes such as electron capture. Since their birth from a supernova, it is supposed that a neutron star will have reached it's equilibrium state, however it is possible that this state is never actually achieved. It is perhaps desirable to use a temperature-dependent EOS, at least for the first hours of a neutron star's life in order to see the effect on it's overall temperature evolution.

In the particular case of magnetic braking in magnetars (§5.1) it was shown that the numerical model presented within this thesis could be effectively used to show the general effect of an unspecified heat source in the neutron star crust without elaborating on the details of the unknown energy producing mechanism. A simple decrease in the magnetic field showed that the effective temperature of the star could be maintanied sufficiently hot

for the timescale of the mechanism in order to arrive close to the region of a cooling curve diagram dominated by the magnetars. (see Figures 5.3 and 5.4).

The insulating effect of the azimuthal magnetic field components confined within the stellar crust producing superficial hot spots centered on the magnetic poles surrounded by a cooler equatorial belt was shown in the surface temperature profiles in Fig. 4.10. Supposing that this is a viable mechanism to produce non-uniform surface temperatures, a study of the geometry of the observation of light curves of these stars suggests a relation between the pulsed fraction (PF) and the gravitational radius of the star. In the particular case of the high-field pulsar PSR J1119-6127, a simple model of the *beaming* reproduces the large reported PF of $74 \pm 14\%$ [41] (see Figure 5.7).

It's altogether possible that there exist *quark* stars or, equally possible, *hybrid* stars - those that have an inner core of deconfined quark matter surrounded by an outer core of hadronic matter covered by a thin baryonic crust. Preliminary work done with Dr. Irina Sagert (Center for Exploration of Energy and Matter at Indiana University) using an energy diffusion model inside a compact star with a baryonic crust shows the dramatic effect possible with the addition of a quark nucleus Equation of State (Figure 6.1). The EOS was constructed by Dr. Sagert and presented in her doctoral thesis for Goethe Univeristy (Frankfurt, Germany, 2010 [91]). There are two cooling curves: the *dotted line* represents the result of a 1D neutron star model presented in Section §4.3; the secund lower curve is that of a hybrid star with a strange matter core. It is obvious that the neutrino cooling is very strong and that the T_e of the star decreases dramatically at a very young age. There is much activity in this area of compact star cooling research (see, for example, the work of Blaschke, Grigorian & Voskresensky [16] or the more recent Schramm et al 2012 [93]).

Theoretical modeling is fundamental to the continuing support of observational initiatives focusing on compact stars. One branch cannot exist without the other and it is this relationship that is the base objective of the research presented in this thesis: to contribute to the increasingly relevant discourse between observational, theoretical and experimental astrophysics.

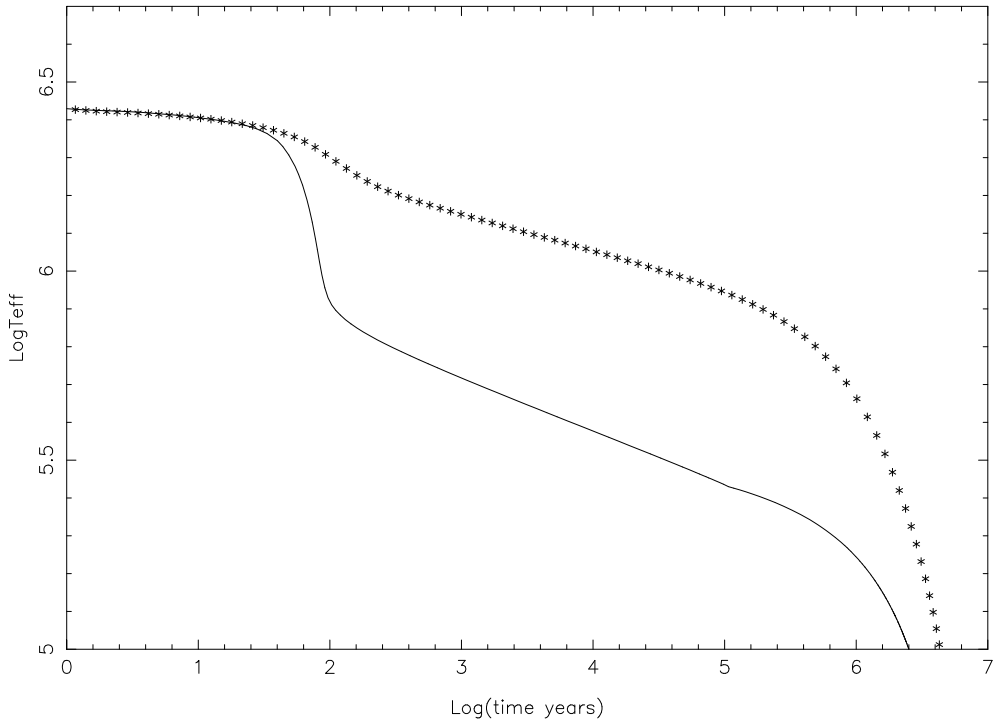

Figure 6.1 The thermal evolution of a hybrid star (*solid line*) - deconfined quark inner core with a hadronic outer core and baryonic crust - compared with a neutron star (*dotted line*).

Bibliography

[1] D. N. Aguilera, J. A. Pons, and J. A. Miralles. 2D Cooling of magnetized neutron stars. A&A, 486:255–271, July 2008.

[2] A. Akmal, V. R. Pandharipande, and D. G. Ravenhall. Equation of state of nucleon matter and neutron star structure. Phys. Rev. C, 58:1804–1828, September 1998.

[3] L. Amundsen and E. Ostgaard. Superfluidity of neutron matter (I). Singlet pairing. *Nuclear Physics A*, 437:487–508, April 1985.

[4] L. Amundsen and E. Ostgaard. Superfluidity of neutron matter (II). Triplet pairing. *Nuclear Physics A*, 442:163–188, August 1985.

[5] H. An, V. M. Kaspi, J. A. Tomsick, A. Cumming, A. Bodaghee, E. V. Gotthelf, and F. Rahoui. Chandra Observations of SGR 1627-41 near Quiescence. ApJ, 757:68, September 2012.

[6] W. B. Ashworth, Jr. A Probable Flamsteed Observations of the Cassiopeia-A Supernova. *Journal for the History of Astronomy*, 11:1, 1980.

[7] W. Baade and F. Zwicky. Remarks on Super-Novae and Cosmic Rays. *Physical Review*, 46:76–77, July 1934.

[8] D. A. Baiko, P. Haensel, and D. G. Yakovlev. Thermal conductivity of neutrons in neutron star cores. A&A, 374:151–163, July 2001.

[9] D. A. Baiko and D. G. Yakovlev. Thermal and electric conductivities of Coulomb crystals in the inner crust of a neutron star. *Astronomy Letters*, 22:708–714, September 1996.

[10] M. Baldo, J. Cugnon, A. Lejeune, and U. Lombardo. Proton and neutron superfluidity in neutron star matter. *Nuclear Physics A*, 536:349–365, January 1992.

[11] M. Baldo, Ø. Elgarøy, L. Engvik, M. Hjorth-Jensen, and H.-J. Schulze. $^3P_2$-$^3F_2$ pairing in neutron matter with modern nucleon-nucleon potentials. Phys. Rev. C, 58:1921–1928, October 1998.

[12] J. Bardeen, L. N. Cooper, and J. R. Schrieffer. Microscopic Theory of Superconductivity. *Physical Review*, 106:162–164, April 1957.

[13] G. Baym, H. A. Bethe, and C. J. Pethick. Neutron star matter. *Nuclear Physics A*, 175:225–271, November 1971.

[14] G. Baym, C. Pethick, and P. Sutherland. The Ground State of Matter at High Densities: Equation of State and Stellar Models. ApJ, 170:299, December 1971.

[15] A. M. Beloborodov. Gravitational Bending of Light Near Compact Objects. ApJ, 566:L85–L88, February 2002.

[16] D. Blaschke, H. Grigorian, and D. N. Voskresensky. Cooling of hybrid neutron stars and hypothetical self-bound objects with superconducting quark cores. A&A, 368:561–568, March 2001.

[17] J. Braithwaite and H. C. Spruit. A fossil origin for the magnetic field in A stars and white dwarfs. Nature, 431:819–821, October 2004.

[18] F. Camilo, V. M. Kaspi, A. G. Lyne, R. N. Manchester, J. F. Bell, N. D'Amico, N. P. F. McKay, and F. Crawford. Discovery of Two High Magnetic Field Radio Pulsars. ApJ, 541:367–373, September 2000.

[19] J. Chadwick. Possible Existence of a Neutron. Nature, 129:312, February 1932.

[20] S. Chandrasekhar. The Maximum Mass of Ideal White Dwarfs. ApJ, 74:81, July 1931.

[21] N.-C. Chao, J. W. Clark, and C.-H. Yang. Proton superfluidity in neutron-star matter. *Nuclear Physics A*, 179:320–332, January 1972.

[22] J. M. C. Chen, J. W. Clark, R. D. Davé, and V. V. Khodel. Pairing gaps in nucleonic superfluids. *Nuclear Physics A*, 555:59–89, April 1993.

[23] L. N. Cooper. Bound Electron Pairs in a Degenerate Fermi Gas. *Physical Review*, 104:1189–1190, November 1956.

[24] S. Dall'Osso, S. N. Shore, and L. Stella. Early evolution of newly born magnetars with a strong toroidal field. MNRAS, 398:1869–1885, October 2009.

[25] Ø. Elgarøy, L. Engvik, M. Hjorth-Jensen, and E. Osnes. Triplet pairing of neutrons in β-stable neutron star matter. *Nuclear Physics A*, 607:425–441, February 1996.

[26] E. Farhi and R. L. Jaffe. Strange matter. Phys. Rev. D, 30:2379–2390, December 1984.

[27] R. P. Feynman, N. Metropolis, and E. Teller. Equations of State of Elements Based on the Generalized Fermi-Thomas Theory. *Physical Review*, 75:1561–1573, May 1949.

[28] E. Flowers, M. Ruderman, and P. Sutherland. Neutrino pair emission from finite-temperature neutron superfluid and the cooling of young neutron stars. ApJ, 205:541–544, April 1976.

[29] B. Friedman and V. R. Pandharipande. Hot and cold, nuclear and neutron matter. *Nuclear Physics A*, 361:502–520, May 1981.

[30] S. Gandolfi, A. Y. Illarionov, S. Fantoni, F. Pederiva, and K. E. Schmidt. Equation of State of Superfluid Neutron Matter and the Calculation of the S01 Pairing Gap. *Physical Review Letters*, 101(13):132501, September 2008.

[31] F. P. Gavriil, M. E. Gonzalez, E. V. Gotthelf, V. M. Kaspi, M. A. Livingstone, and P. M. Woods. Magnetar-Like Emission from the Young Pulsar in Kes 75. *Science*, 319:1802–, March 2008.

[32] U. Geppert, M. Kuker, and D. Page. Temperature distribution in magnetized neutron star crusts. A&A, 426:267–277, October 2004.

[33] U. Geppert, M. Kuker, and D. Page. Temperature distribution in magnetized neutron star crusts. II. The effect of a strong toroidal component. A&A, 457:937–947, October 2006.

[34] U. Geppert, D. Page, and T. Zannias. Submergence and re-diffusion of the neutron star magnetic field after the supernova. A&A, 345:847–854, May 1999.

[35] A. Gezerlis and J. Carlson. Strongly paired fermions: Cold atoms and neutron matter. Phys. Rev. C, 77(3):032801, March 2008.

[36] R. Giacconi, H. Gursky, F. R. Paolini, and B. B. Rossi. Evidence for x Rays From Sources Outside the Solar System. *Physical Review Letters*, 9:439–443, December 1962.

[37] O. Y. Gnedin, D. G. Yakovlev, and A. Y. Potekhin. Thermal relaxation in young neutron stars. MNRAS, 324:725–736, June 2001.

[38] T. Gold. Rotating Neutron Stars as the Origin of the Pulsating Radio Sources. Nature, 218:731–732, May 1968.

[39] T. Gold. Rotating Neutron Stars and the Nature of Pulsars. Nature, 221:25–27, January 1969.

[40] P. Goldreich and A. Reisenegger. Magnetic field decay in isolated neutron stars. ApJ, 395:250–258, August 1992.

[41] M. E. Gonzalez, V. M. Kaspi, F. Camilo, B. M. Gaensler, and M. J. Pivovaroff. Unusual Pulsed X-Ray Emission from the Young, High Magnetic Field Pulsar PSR J1119-6127. ApJ, 630:489–494, September 2005.

[42] E. V. Gotthelf, R. Perna, and J. P. Halpern. Modeling the Surface X-ray Emission and Viewing Geometry of PSR J0821-4300 in Puppis A. ApJ, 724:1316–1324, December 2010.

[43] G. Greenstein and G. J. Hartke. Pulselike character of blackbody radiation from neutron stars. ApJ, 271:283–293, August 1983.

[44] E. H. Gudmundsson, C. J. Pethick, and R. I. Epstein. Neutron star envelopes. ApJ, 259:L19–L23, August 1982.

[45] F. Haberl. The Magnificent Seven: Nearby Isolated Neutron Stars with strong Magnetic Fields. In U. G. Briel, S. Sembay, and A. Read, editors, *5 years of Science with XMM-Newton*, pages 39–44, June 2005.

[46] P. Haensel, J. L. Zdunik, and J. Dobaczewski. Composition and equation of state of cold catalyzed matter below neutron drip. A&A, 222:353–357, September 1989.

[47] C. O. Heinke and W. C. G. Ho. Direct Observation of the Cooling of the Cassiopeia A Neutron Star. ApJ, 719:L167–L171, August 2010.

[48] D. J. Helfand, B. F. Collins, and E. V. Gotthelf. Chandra X-Ray Imaging Spectroscopy of the Young Supernova Remnant Kesteven 75. ApJ, 582:783–792, January 2003.

[49] A. Hewish, S. J. Bell, J. D. H. Pilkington, P. F. Scott, and R. A. Collins. Observation of a Rapidly Pulsating Radio Source. Nature, 217:709–713, February 1968.

[50] W. C. G. Ho, K. Glampedakis, and N. Andersson. Magnetars: super(ficially) hot and super(fluid) cool. MNRAS, 422:2632–2641, May 2012.

[51] M. Hoffberg, A. E. Glassgold, R. W. Richardson, and M. Ruderman. Anisotropic Superfluidity in Neutron Star Matter. *Physical Review Letters*, 24:775–777, April 1970.

[52] N. Itoh. Hydrostatic Equilibrium of Hypothetical Quark Stars. *Progress of Theoretical Physics*, 44:291–292, July 1970.

[53] N. Itoh, H. Hayashi, A. Nishikawa, and Y. Kohyama. Neutrino Energy Loss in Stellar Interiors. VII. Pair, Photo-, Plasma, Bremsstrahlung, and Recombination Neutrino Processes. ApJS, 102:411, February 1996.

[54] N. Itoh, Y. Kohyama, N. Matsumoto, and M. Seki. Electrical and thermal conductivities of dense matter in the crystalline lattice phase. ApJ, 285:758–765, October 1984.

[55] N. Itoh, S. Mitake, H. Iyetomi, and S. Ichimaru. Electrical and thermal conductivities of dense matter in the liquid metal phase. I - High-temperature results. ApJ, 273:774–782, October 1983.

[56] A. D. Kaminker, A. Y. Potekhin, D. G. Yakovlev, and G. Chabrier. Heating and cooling of magnetars with accreted envelopes. MNRAS, 395:2257–2267, June 2009.

[57] A. D. Kaminker, D. G. Yakovlev, A. Y. Potekhin, N. Shibazaki, P. S. Shternin, and O. Y. Gnedin. Magnetars as cooling neutron stars with internal heating. MNRAS, 371:477–483, September 2006.

[58] V. M. Kaspi. Soft Γ Repeaters and Anomalous X-ray Pulsars: Together Forever. In F. Camilo and B. M. Gaensler, editors, *Young Neutron Stars and Their Environments*, volume 218 of *IAU Symposium*, page 231, 2004.

[59] V. M. Kaspi and M. A. McLaughlin. Chandra X-Ray Detection of the High Magnetic Field Radio Pulsar PSR J1718-3718. ApJ, 618:L41–L44, January 2005.

[60] J. M. Lattimer. The Nuclear Equation of State and Neutron Star Masses. *Annual Review of Nuclear and Particle Science*, 62:485–515, November 2012.

[61] J. M. Lattimer, M. Prakash, C. J. Pethick, and P. Haensel. Direct URCA process in neutron stars. *Physical Review Letters*, 66:2701–2704, May 1991.

[62] K. P. Levenfish and D. G. Yakovlev. Specific heat of neutron star cores with superfluid nucleons. *Astronomy Reports*, 38:247–251, March 1994.

[63] P. Markey and R. J. Tayler. The adiabatic stability of stars containing magneticfields-II. Poloidal fields. MNRAS, 163:77, 1973.

[64] McGill Pulsar Group. McGill SGR/AXP Online Catalog. `http://www.physics.mcgill.ca/~pulsar/magnetar/main.html`, October 2012.

[65] M. A. McLaughlin, I. H. Stairs, V. M. Kaspi, D. R. Lorimer, M. Kramer, A. G. Lyne, R. N. Manchester, F. Camilo, G. Hobbs, A. Possenti, N. D'Amico, and A. J. Faulkner. PSR J1847-0130: A Radio Pulsar with Magnetar Spin Characteristics. ApJ, 591:L135–L138, July 2003.

[66] J. W. Negele and D. Vautherin. Neutron star matter at sub-nuclear densities. *Nuclear Physics A*, 207:298–320, June 1973.

[67] J.A. Niskanen and J.A. Sauls. unpublished manuscript. unpublished, 1981.

[68] J. R. Oppenheimer and G. M. Volkoff. On Massive Neutron Cores. *Physical Review*, 55:374–381, February 1939.

[69] D. Page. Surface temperature of a magnetized neutron star and interpretation of the ROSAT data. 1: Dipole fields. ApJ, 442:273–285, March 1995.

[70] D. Page. Thermal Evolution of Isolated Neutron Stars. In R. Buccheri, J. van Paradijs, and A. Alpar, editors, *NATO ASIC Proc. 515: The Many Faces of Neutron Stars.*, page 539, 1998.

[71] D. Page. Neutron Star Cooling: I. In W. Becker, editor, *Astrophysics and Space Science Library*, volume 357 of *Astrophysics and Space Science Library*, page 247, 2009.

[72] D. Page, U. Geppert, and T. Zannias. General relativistic treatment of the thermal, magnetic and rotational evolution of isolated neutron stars with crustal magnetic fields. A&A, 360:1052–1066, August 2000.

[73] D. Page, J. M. Lattimer, M. Prakash, and A. W. Steiner. Minimal Cooling of Neutron Stars: A New Paradigm. ApJS, 155:623–650, December 2004.

[74] D. Page, J. M. Lattimer, M. Prakash, and A. W. Steiner. Neutrino Emission from Cooper Pairs and Minimal Cooling of Neutron Stars. ApJ, 707:1131–1140, December 2009.

[75] D. Page, M. Prakash, J. M. Lattimer, and A. W. Steiner. Rapid Cooling of the Neutron Star in Cassiopeia A Triggered by Neutron Superfluidity in Dense Matter. *Physical Review Letters*, 106(8):081101, February 2011.

[76] D. Page and S. Reddy. Dense Matter in Compact Stars: Theoretical Developments and Observational Constraints. *Annual Review of Nuclear and Particle Science*, 56:327–374, November 2006.

[77] D. P. Page, M. Prakash, J. Lattimer, and A. Steiner. Superfluid Neutrons in the Core of the Cassiopeia-A Neutron Star. In *Brazilian Workshop on Nuclear Physics (XXXIV BWNP)*, 2011.

[78] J. F. Pérez-Azorín, J. A. Miralles, and J. A. Pons. Thermal radiation from magnetic neutron star surfaces. A&A, 433:275–283, April 2005.

[79] M. J. Pivovaroff, V. M. Kaspi, and F. Camilo. X-Ray Observations of the High Magnetic Field Radio Pulsar PSR J1814-1744. ApJ, 535:379–384, May 2000.

[80] J. A. Pons, J. A. Miralles, and U. Geppert. Magneto-thermal evolution of neutron stars. A&A, 496:207–216, March 2009.

[81] A. Y. Potekhin, G. Chabrier, and D. G. Yakovlev. Internal temperatures and cooling of neutron stars with accreted envelopes. A&A, 323:415–428, July 1997.

[82] A. Y. Potekhin, G. Chabrier, and D. G. Yakovlev. Heat blanketing envelopes and thermal radiation of strongly magnetized neutron stars. Ap&SS, 308:353–361, April 2007.

[83] A. Y. Potekhin, D. G. Yakovlev, G. Chabrier, and O. Y. Gnedin. Thermal Structure and Cooling of Superfluid Neutron Stars with Accreted Magnetized Envelopes. ApJ, 594:404–418, September 2003.

[84] William H. Press, Brian P. Flannery, Saul A. Teukolsky, and William T. Vetterling. *Numerical Recipes in FORTRAN 77: The Art of Scientific Computing*. Cambridge University Press, 2 edition, September 1992.

[85] William H. Press, Saul A. Teukolsky, William T. Vetterling, and Brian P. Flannery. *Numerical Recipes 3rd Edition: The Art of Scientific Computing*. Cambridge University Press, New York, NY, USA, 3 edition, 2007.

[86] B. S. Pudliner, V. R. Pandharipande, J. Carlson, and R. B. Wiringa. Quantum Monte Carlo Calculations of A $\leq$ 6 Nuclei. *Physical Review Letters*, 74:4396–4399, May 1995.

[87] D. G. Ravenhall, C. J. Pethick, and J. R. Wilson. Structure of Matter below Nuclear Saturation Density. *Physical Review Letters*, 50:2066–2069, June 1983.

[88] N. Rea and P. Esposito. Magnetar outbursts: an observational review. In D. F. Torres and N. Rea, editors, *High-Energy Emission from Pulsars and their Systems*, page 247, 2011.

[89] M. Ruderman. A Biography of the Magnetic Field of a Neutron Star. In A. Baykal, S. K. Yerli, S. C. Inam, and S. Grebenev, editors, *NATO ASIB Proc. 210: The Electromagnetic Spectrum of Neutron Stars*, page 47, January 2005.

[90] R. E. Rutledge, D. B. Fox, and A. H. Shevchuk. Discovery of an Isolated Compact Object at High Galactic Latitude. ApJ, 672:1137–1143, January 2008.

[91] I. Sagert. *Probing the QCD Phase Diagram with Compact Stars*. PhD thesis, Johann Wolfgang Goethe - Universität in Frankfurt am Main, 2010.

[92] C. Schaab, D. Voskresensky, A. D. Sedrakian, F. Weber, and M. K. Weigel. Impact of medium effects on the cooling of non-superfluid and superfluid neutron stars. A&A, 321:591–604, May 1997.

[93] S. Schramm, V. Dexheimer, R. Negreiros, T. Schurhoff, and J. Steinheimer. Structure and Cooling of Neutron and Hybrid Stars. *ArXiv e-prints*, February 2012.

[94] A. Schwenk, B. Friman, and G. E. Brown. Renormalization group approach to neutron matter: quasiparticle interactions, superfluid gaps and the equation of state. *Nuclear Physics A*, 713:191–216, January 2003.

[95] L. Shapiro and S.A. Teukolsky. *Black Foles, White Dwarfs and Neutron Stars: The Physics of Compact Objects*. Wiley-Interscience, New York, N.Y., 1983.

[96] P. S. Shternin and D. G. Yakovlev. Electron-muon heat conduction in neutron star cores via the exchange of transverse plasmons. Phys. Rev. D, 75(10):103004, May 2007.

[97] P. S. Shternin, D. G. Yakovlev, C. O. Heinke, W. C. G. Ho, and D. J. Patnaude. Cooling neutron star in the Cassiopeia A supernova remnant: evidence for superfluidity in the core. MNRAS, 412:L108–L112, March 2011.

[98] V. Smirnov. *Cours de Mathématiques Supérieurs*, volume II. Éditions Mir, Moscou, 1970.

[99] T. Takatsuka. Energy Gap in Neutron-Star Matter. *Progress of Theoretical Physics*, 48:1517–1533, November 1972.

[100] T. Takatsuka. Proton Superfluidity in Neutron-Star Matter. *Progress of Theoretical Physics*, 50:1754–1755, November 1973.

[101] R. Tamagaki. Superfluid state in neutron star matter. I. Generalized Bogoliubov transformation and existence of $^3P_2$ gap at high density. *Progress of Theoretical Physics*, 44:905–928, 1970.

[102] H. Tananbaum. Cassiopeia A. IAU Circ., 7246:1, September 1999.

[103] L.N. Trefethen. Finite Difference and Spectral Methods for Ordinary and Partial Differential Equations. `http://people.maths.ox.ac.uk/trefethen/pdetext.html`, 1996.

[104] D. Viganò. *Magnetic fields in neutron stars.* PhD thesis, University of Alicante, September 2013.

[105] D. N. Voskresensky and A. V. Senatorov. . *Sov. J. Nucl. Phys*, 45:411, 1987.

[106] J. Wambach, T. L. Ainsworth, and D. Pines. Quasiparticle interactions in neutron matter for applications in neutron stars. *Nuclear Physics A*, 555:128–150, April 1993.

[107] S. Weissenborn, I. Sagert, G. Pagliara, M. Hempel, and J. Schaffner-Bielich. Quark Matter in Massive Compact Stars. ApJ, 740:L14, October 2011.

[108] R. B. Wiringa, V. G. J. Stoks, and R. Schiavilla. Accurate nucleon-nucleon potential with charge-independence breaking. Phys. Rev. C, 51:38–51, January 1995.

[109] D. G. Yakovlev, A. D. Kaminker, and O. Y. Gnedin. $^1S_0$ neutron pairing vs. observations of cooling neutron stars. A&A, 379:L5–L8, November 2001.

[110] D. G. Yakovlev, A. D. Kaminker, P. Haensel, and O. Y. Gnedin. The cooling neutron star in 3C 58. A&A, 389:L24–L27, July 2002.

[111] D. G. Yakovlev and V. A. Urpin. Thermal and Electrical Conductivity in White Dwarfs and Neutron Stars. Soviet Ast., 24:303, June 1980.

[112] V. E. Zavlin. First X-Ray Observations of the Young Pulsar J1357-6429. ApJ, 665:L143–L146, August 2007.

[113] V. E. Zavlin, G. G. Pavlov, Y. A. Shibanov, and J. Ventura. Thermal radiation from rotating neutron star: effect of the magnetic field and surface temperature distribution. A&A, 297:441, May 1995.